

PhD

3rd CYCLE

FCUP
UA
UM
HW
2024

U.PORTO

Towards ultrafast and ultracompact lasers: uncovering ultrashort pulse generation in semiconductor lasers with novel characterization approaches

Tiago dos Santos Gomes

FC



Towards ultrafast and ultracompact lasers: uncovering ultrashort pulse generation in semiconductor lasers with novel characterization approaches

Tiago dos Santos Gomes

Ph.D. Thesis co-supervision between the University of Porto and the Heriot-Watt University

Faculty of Sciences of the University of Porto, University of Aveiro, University of Minho, Heriot-Watt University

2024

PhD

Towards ultrafast and ultracompact lasers: uncovering ultrashort pulse generation in semiconductor lasers with novel characterization approaches

Tiago dos Santos Gomes

Thesis carried out as part of the Ph.D. in Physics
Department of Physics and Astronomy
2024

Supervisor
Helder Crespo, Professor, Dep. of Physics and Astronomy, Faculty of Sciences, University of Porto, Portugal

Co-supervisor
Maria Ana Cataluna, Professor, Institute of Photonics and Quantum Sciences, Heriot-Watt University, Scotland

U.PORTO
FACULDADE DE CIÊNCIAS
UNIVERSIDADE DO PORTO

HERIOT WATT
UNIVERSITY

Todas as correções determinadas pelo júri, e só essas, foram efetuadas.

A/O Orientadora(o),

Maria Ana Catalina

Edimburgo, UK, 9/ 1/ 25

Porto, _____/_____/_____

13 de Janeiro de 2025

Nota: Esta página só deverá ser incluída, **no âmbito da versão final após defesa e apenas no caso de o júri aprovar a tese com recomendação de correção**, pelo estudante, dos erros, imprecisões ou incorreções formais identificados e expressamente referidos durante as provas. **Esta página deve ser eliminada da versão a ser submetida no âmbito do pedido de admissão a provas.**

“ Look again at that dot. That’s here. That’s home. That’s us. On it everyone you love, everyone you know, everyone you ever heard of, every human being who ever was, lived out their lives. The aggregate of our joy and suffering, thousands of confident religions, ideologies, and economic doctrines, every hunter and forager, every hero and coward, every creator and destroyer of civilization, every king and peasant, every young couple in love, every mother and father, hopeful child, inventor and explorer, every teacher of morals, every corrupt politician, every ”superstar,” every ”supreme leader,” every saint and sinner in the history of our species lived there-on a mote of dust suspended in a sunbeam.

That’s here. That’s home. That’s us. ”

Carl Sagan, 1994

Acknowledgements

I believe I speak for most Ph.D. students when I say that we always write the acknowledgments section at the end of the thesis writing. Not because it is hard, but because there are so many people to be thankful for.

My first words of gratitude are directed to my supervisors, Prof. Helder Crespo and Prof. Maria Ana Cataluna, for guiding me throughout this 4-year journey. This work would not be completed without their extreme patience, guidance, and, most of all, their love for physics. To Prof. Helder, I specifically want to thank once again for introducing me to the fantastic world of ultrafast lasers, and for the encouragement he gave me to pursue this path and study at one of the most beautiful places in the world: the great Scotland (”Freedom!!”). To Prof. Maria Ana, I want to thank for the endless help, for teaching me to never give up, for the extremely contagious laughter, and for teaching me to always ”pull the hot coal to our sardine” (paraphrasing, but not really, José Mourinho).

I had the privilege to share the lab in Portugal and the lab in Scotland with great friends. In Portugal, I would like to thank Ana (1), Ana (2), Mike, Tânia, and Tiago for their friendship, and for all the good times we had together (Munchies!). In Scotland, I have to thank Ana, Miguel, and Sven for all the good times we have spent in the lab, and for all the afternoons spent on Starbucks. I will cherish these moments. I would also like to thank Dr. Benjamín Alonso, for the fruitful collaboration in applying the self-calibrating d-scan retrieval algorithm to our measurements.

I would also like to express my gratitude to D. Isabel Alves and Eng. Francisco Carpinteiro, from IFIMUP, and Shannon Mitchell, Cameron Smith, and John Binnie, from IPaQS, for all the technical support.

To my friends from my hometown, thank you for all the game nights, thematic dinners, picnics, camps, trips to London, and Arnold noises inside jokes, but most of all, thank you for being my friends.

I would like to thank Innolume GmbH (Germany) for the growth and fabrication of the mode-locked lasers used in this thesis, and the European Research Council (ERC) under the European Union’s Horizon 2020 research and innovation program (grant agreement No. 640537), for the financial support. I would also like to thank Fundação para a Ciência e Tecnologia (Portugal) for financing my doctoral work through grant 2020.08110.BD.

To my parents, Alexandre and Gabriela, and my sister Mariana, I want to thank you from the bottom of my heart for all the love and support you gave me for as long as I can remember. People say that ”we choose our family”, and my family could not have been better chosen. I love you all.

And finally, I want to thank you, Rita. You are the love of my life and have supported me for the last 10 years. An entire decade spent with you. You were my hugs when I celebrated an achievement, and the shoulder to cry on when things did not go as expected. I cannot wait to spend the rest of my life building a home with you.

Resumo

Os díodos laser semicondutores mode-locked são fontes de impulsos ultracurtos compactos, de baixo custo e eletricamente eficientes. Materiais baseados em quantum-dots fornecem acesso a uma dinâmica de ganho e absorção ultrarrápidas, assim como uma curva de ganho ultralarga devido ao alargamento não homogéneo, fornecendo a capacidade de gerar impulsos laser de alta potência e subpicossegundos, com taxas de repetição muito altas (até centenas de GHz) e baixo jitter temporal. No entanto, ainda não é possível aproveitar todas as suas capacidades e alcançar regimes de mode-locking com maior potência, uma vez que usando uma corrente mais elevada cria instabilidades no trem de impulsos.

Dispersion-scan (ou d-scan, abreviadamente) é uma técnica que se baseia numa configuração simples e totalmente inline, onde um sinal não linear é medido em função da dispersão aplicada ao impulso laser, criando uma medida 2D que, através de algoritmos de retrieval apropriados, podem reconstruir tanto a potência espectral como a fase (e, portanto, o perfil temporal) de impulsos laser ultracurtos. Nesta tese, desenvolvemos uma técnica d-scan altamente sensível, capaz de medir impulsos com baixa energia e durações temporais elevadas. Juntamente com o algoritmo de self-calibrating retrieval, é possível quantificar pela primeira vez as instabilidades de trens de impulsos em díodos laser semicondutores, fornecendo informações privilegiadas sobre a dinâmica de geração de impulsos nestas fontes laser. O processo de amplificação de impulsos gerados em díodo laser baseados em quantum-dots usando amplificadores ópticos semicondutores também foi investigado, em particular o efeito do processo de amplificação no chirp, perfil temporal e instabilidades dos impulsos.

Palavras-chave: impulsos laser ultracurtos, díodos laser semicondutores, dispersion-scan, amplificadores óticos de semicondutor

Abstract

Semiconductor mode-locked laser diodes are compact, low-cost, and wall-plug efficient sources of ultrashort pulses. Quantum-dot materials provide access to ultrafast gain and absorption dynamics, as well as ultra-broadband gain due to inhomogeneous broadening, providing the capabilities for generating sub-picosecond and high-power laser pulses, with very high repetition rates (up to hundreds of GHz) and low timing jitter. However, it is still not possible to harness their full capabilities and achieve mode-locking regimes with higher optical output power, since driving them at higher gain currents creates pulse train instabilities.

Dispersion-scan (or d-scan, for short) is a technique that relies on a simple and fully in-line setup, where a nonlinear signal is measured as a function of the dispersion applied to the laser pulse, creating a 2D trace that, through appropriate retrieval algorithms, can reconstruct both the spectral power and phase (and therefore the temporal profile) of ultrashort laser pulses. In this thesis, we have developed a highly-sensitive d-scan technique, capable of measuring pulses with very low energy and ps time durations. Together with the self-calibrating retrieval algorithm, this allows quantifying for the first time pulse train instabilities in semiconductor laser diodes, providing privileged information about the pulse generation dynamics in these laser sources. The pulse amplification process of quantum-dot mode-locked laser diode pulses using semiconductor optical amplifiers was also investigated, namely the effect of the amplification process on the pulses' chirp, temporal profile, and instabilities.

Keywords: ultrashort laser pulses, semiconductor laser diodes, dispersion-scan, semiconductor optical amplifiers

Table of Contents

List of Tables xiii
List of Figures xv
List of Abbreviations xxi
List of Publications xxii

1. Introduction 1
   1.1. Motivation 1
   1.2. Mathematical description 3
   1.3. Mode-locking 4
   1.4. Dispersion 5
      1.4.1. Dispersion Compensation 6
   1.5. Nonlinear Optics 8
      1.5.1. Second Harmonic Generation 9
      1.5.2. Phase Matching 10
      1.5.3. Third Harmonic Generation 11
      1.5.4. Self-phase modulation 11
   1.6. Ultrashort Laser Pulse Characterization 12
      1.6.1. Intensity autocorrelation 12
      1.6.2. Frequency-Resolved Optical Gating 13
      1.6.3. Spectral Phase Interferometry for Direct Electric-field Reconstruction 13
      1.6.4. Multiphoton Intrapulse Interference Phase Scan 14
      1.6.5. Dispersion-scan 14
   1.7. Purpose of this thesis 17
2. Surface third-harmonic dispersion-scan with ptychographic retrieval 19
   2.1. Introduction 19
   2.2. Experimental setup 20
   2.3. Ptychographic retrieval 22
   2.4. Experimental results 27
   2.5. Conclusions and future work 30
3. Highly-sensitive dispersion-scan setup for the characterization of semiconductor mode-locked laser diodes 31
   3.1. Semiconductor laser diodes 31
   3.2. Mode-locking in semiconductor lasers 32
   3.3. The advantages of quantum-dots as gain media 33
   3.4. Mode-locked quantum-dot lasers 35

3.5. State of the art in low-power, long pulse duration pulse measurements 36
3.5.1. Frequency-Resolved Optical Gating 36
3.5.2. Frequency-Resolved Mach-Zender Gating 37
3.5.3. Stepped heterodyne detection 37
3.5.4. Sonogram 37
3.5.5. Shifted Wave Interference Fourier Transform Spectroscopy 38
3.6. The advantages of dispersion-scan 38
3.7. Used quantum-dot laser 38
3.8. Setup design 39
3.8.1. Pulse compression 41
3.8.2. Nonlinear signal generation 45
3.8.3. Nonlinear signal detection 46
3.8.4. Monochromator calibration 47
3.9. D-scan measurement and retrieval 48
3.9.1. Pulse measurement across the dispersion range 49
3.10. Setup performance 50
3.11. Conclusions and future work 53
4. Mode-locking dynamics in semiconductor laser diodes 55
4.1. Introduction 55
4.2. Dispersion-scan measurements 56
4.3. Spectral power and phase retrieval 57
4.4. Temporal profile visualization 59
4.5. Pulse measurement across the dispersion range 63
4.6. Conclusions and future work 64
5. Quantification of pulse train instabilities in semiconductor laser diodes 67
5.1. Pulse train instabilities 67
5.1.1. D-scan simulations 70
5.2. Measurement of pulse train instabilities 71
5.3. Self-calibrating d-scan 72
5.4. Self-calibrating retrieval of stable pulses 73
5.5. Measurement of pulse train instabilities 75
5.5.1. Mode-locking transition 77
5.6. Map of instabilites 78
5.6.1. Unstable ML and modulated ML 83
5.6.2. Harmonic mode-locking 84
5.7. Conclusions and future work 87
6. Characterization of pulses amplified by semiconductor optical amplifiers 89
6.1. The need for pulse amplification 89

6.2. Semiconductor Optical Amplifiers 90
6.3. Experimental setup 92
6.4. Amplification of stable pulse trains 94
6.4.1. Case 1 94
6.4.2. Case 2 99
6.4.3. Case 3 100
6.5. Amplification of unstable pulse trains 102
6.6. Conclusions and future work 105
7. Conclusions and future work 107

Bibliography 108

List of Tables

4.1. D-scan error G obtained for the retrieved d-scan traces. 57

5.1. Instability metric for a constant reverse bias voltage (V_{abs} = 4.6 V), and a drive current changing from 220 mA to 280 mA. The real GDD/L introduced by the compressor is equal to $-5.36\ \mathrm{ps}^2/m$. The values in bold indicate driving currents where the retrieved GDD/L differs significantly from the actual GDD/L from the compressor, indicating the presence of pulse train instabilities. 77

6.1. G error obtained for the retrieved d-scan traces for the amplified pulses. 95

List of Figures

1.1. Intensity of a laser with a single mode (top), 100 modes with random phases (middle), and 100 modes with locked phases (bottom). 5
1.2. Temporal effects of a linear (GD - Group Delay), quadratic (GDD - Group Delay Dispersion), and cubic (TOD - Third Order Dispersion) phase on a transform-limited (TL) pulse (blue curve). Further numerical details in text....7
1.3. Schematic of a standard prism compressor. Reproduced from [34]....7
1.4. (a) Structure of a DCM with alternating layers with different refractive index and thickness. (b) Penetration depth as a function of wavelength for the DCM, which provides negative dispersion in the 650 to 1050 nm region. Reproduced from [37]. 8
1.5. Second-order noncollinear autocorrelation setup. 12
1.6. SPIDER experimental setup. 13
1.7. (a) General schematics of a dispersion-scan setup and retrieval procedure. (b) Typical d-scan experimental setup [27]. 15

2.1. STHG d-scan experimental setup. DCM1,2: double-chirped mirrors. M1: mirror. VNDF: variable neutral-density filter. FS: fused silica. Reproduced from [52]. 21
2.2. Ptychographic retrieval of a pulse with a Gaussian profile (G = $0.03\,\%$). 24
2.3. Ptychographic retrieval of a pulse with a Gaussian profile, with $40\,\%$ Gaussian noise (G = $0.54\,\%$). 25
2.4. Ptychographic retrieval of a pulse with a complex spectral profile (G = $0.09\,\%$). 25
2.5. Flowchart diagram describing the ptychography algorithm with the filter correction variation. $E_i(\omega)$: guess for the spectral power and phase (i^{th} iteration); $T^{sim,i}(\omega,z)$: simulated d-scan using the guess for the spectral power and phase (i^{th} iteration); FPM: Forward Propagation Model; BPM: Backward Propagation Model; l: position of the compressor; $\mu(\omega)$: response function. Reproduced from [52]....26
2.6. Measured (left) and retrieved (right) STHG d-scan using a 0.5 mm-thick sapphire substrate. Reproduced from [52]. 27
2.7. Measured (left) and retrieved (right) SHG d-scan using a $20\,\mu$m-thick BBO crystal. Reproduced from [52]....28
2.8. Mean retrieved spectral phase and amplitude for SHG d-scan (orange and red, respectively) and STHG d-scan (blue and purple, respectively), along with the calculated standard deviation (shaded area). The black curve is an independent measurement of the spectral power of the laser, and the green curve is an independent spectral phase retrieval for SHG d-scan, using a standard retrieval algorithm. Reproduced from [52]. 28
2.9. Pulse temporal profile retrieved by SHG d-scan (orange) and STHG d-scan (dashed blue), using both the retrieved spectral amplitude and phase. Reproduced from [52].29

3.1. Schematic representation and respective density of states of bulk (a), quantum well (b), quantum wire (c), and quantum dot (d) semiconductors [80]....32
3.2. (a) Illustration of a two-section passively mode-locked quantum-dot laser. (b) Gain and loss dynamics in a quantum-dot laser with a saturable absorber. Reproduced from [86]. 33
3.3. Normalized modal gain vs carrier density for bulk, quantum well and quantum dot systems [87]. 34

3.4. Left: ideal QD system, with all the QDs having the same size, and respective density of states $D(E)$. Right: real QD system, with an inhomogeneous broadening depicted in the density of states, caused by the Gaussian size distribution of the quantum dots. Reproduced from [86]....34
3.5. Schematic representation of the QD laser used in these experiments, with a distributed saturable absorber. 39
3.6. QD laser used throughout the experiments. 39
3.7. Experimental setup. Blue section (S1): compressor system, based on a single-grating four-pass configuration. Green section (S2): nonlinear signal generation. Red section (S3): Nonlinear signal frequency-resolved detection. RR: repetition rate. λ/2: half-wave plate. M1: mirror. HRM: hollow-roof mirror. RRM: retroreflector mirror. PMT: photomultiplier tube. Since the incoming and outgoing beams of the compressor have different heights, the mirror M1 is only aligned for the outgoing beam. For the first and second pass on the grating, the hollow-roof mirror is at a different height, to allow light to enter the compressor. Adapted from [75, 76]. 40
3.8. Experimental d-scan setup, top perspective. 41
3.9. Experimental d-scan setup, side perspective. The black box is needed to reduce stray light captured by the photomultiplier tube. 41
3.10. Single-grating compressor implementation. 42
3.11. Autocorrelation traces (blue curve) and autocorrelation fit assuming a $sech^2$ pulse (orange curve) for pulses obtained at a driving current of 230 mA and a reverse bias voltage of 5.8 V, for distances between the grating and the retroreflector mirror of 29.2 cm, 38.6 cm, and 48 cm. 44
3.12. Evolution of the FWHM of the pulses obtained after the single-grating compressor for different distances between the grating and the retroreflector mirror. Measurements were made for different laser driving conditions. The lines shown are just guides for the eyes. 44
3.13. Monochromator calibration curve. The linear fit will be used as a post-processing calibration curve for the measured wavelengths in the monochromator. 48
3.14. Measured (top left) and retrieved (top right) d-scan traces for pulses obtained at $I_{gain} = 230$ mA and $V_{abs} = 5.4$ V. Retrieved pulse in the frequency (bottom left) and time (bottom right) domain. 49
3.15. Evolution of the temporal profile of the retrieved pulse with the dispersion applied to the pulse driven at $I_{gain} = 230$ mA and $V_{abs} = 5.4$ V. The grating with 600 lines/mm and a blaze wavelength of $1.25\,\mu m$ was used in the single-grating compressor. 50
3.16. Measured (left) and retrieved (right) d-scan traces obtained for the pulses driven at $I_{gain} = 230$ mA and $V_{abs} = 5.6$ V, with 20 (top), 35 (middle) and 50 (bottom) dispersion points. The grating with 600 lines/mm and a blaze wavelength of $1.25\,\mu m$ was used in the single-grating compressor. 52
3.17. Retrieved temporal profiles of the pulses driven at $I_{gain} = 230$ mA and $V_{abs} = 5.6$ V, from d-scan traces with 20 (blue), 35 (orange) and 50 (green) dispersion points. 52

4.1. Measured d-scan traces for different values of I_{gain} (rows) and V_{abs} (columns). 56
4.2. Measured and retrieved d-scan trace for $I_{gain} = 230$ mA and $V_{abs} = 5.2$ V. 57
4.3. Retrieved spectral power (blue) and phase (red), together with an independent spectral measurement (orange) of the pulses obtained at different values of I_{gain} and V_{abs}. The blue and red shaded regions correspond to the standard deviation for the spectral power and phase retrievals, respectively. 58
4.4. Temporal profile of the QD laser pulses obtained at different values of I_{gain} and V_{abs}, uncompressed (blue), compressed (red), and Fourier-limited (green). 59

4.5. Retrieved spectral phase (blue) and the correspondent polynomial fit (orange) of the pulses obtained at $I_{gain} = 230$ mA and $V_{abs} = 4.6$ V. 59
4.6. Effects of the self-phase modulation in a mode-locked semiconductor laser, regarding optical power, carrier density, index of refraction and instantaneous frequency in gain (a) and absorption (b) saturation regimes [127, 128]. 61
4.7. Temporal profile evolution of the QD laser pulses obtained at different values of I_{gain} and V_{abs}, as a function of the dispersion applied to the laser pulses. 63
4.8. Temporal profile of the QD laser pulses at $I_{gain} = 240$ mA and $V_{abs} = 5.2$ V, before (blue), and after the compressor with a grating distance of 0.1 (orange) and 0.53 (green) meters. 64
4.9. Left: retrieved spectral profile (black) and phase (orange) for pulses driven at $I_{gain} = 220$ mA and $V_{abs} = 5.6$ V, together with the filtered spectrum (red), filtered by a logistic filter with central frequency ω_0 (blue). Right: respective temporal profile, uncompressed (blue) and transform-limited (orange) for the retrieved fundamental spectrum, as well as the uncompressed (green) and transform-limited (red) temporal profiles for the filtered pulses. 65

5.1. Autocorrelation traces for a pulse train with random chirp instability (left), random phase distribution (middle), and double-pulsing with mutual timing jitter (right). The blue curves are the autocorrelation traces of the stable pulse train for each situation. On the left graphic, the blue curve is almost indistinguishable from the orange curve. 69
5.2. (a) Base pulse d-scan trace for comparison. (b) to (d): Simulated d-scan trace using a pulse train with linear chirp instability, with $\Gamma = 0.1$ ps^2 (b), $\Gamma = 0.3$ ps^2 (c) and $\Gamma = 0.7$ ps^2 (d). 71
5.3. D-scan simulation of a random phase fluctuation regime, with a base pulse with $GDD = 1.4ps^2$ and $\alpha = 0.1$ (b), $\alpha = 0.3$ (c) and $\alpha = 0.5$ (d). Base pulse d-scan trace for comparison (a). 71
5.4. Measured (upper left) and retrieved (upper right) d-scan traces obtained at I_{gain} = 230 mA and V_{abs} = 4.6 V, using the self-calibrating retrieval algorithm. Retrieved uncompressed (bottom left) and compressed (bottom right) pulses in the temporal domain, using the ptychographic (blue curves) and the self-calibrating (orange curves) retrieval algorithm. 74
5.5. Experimental measurements for a constant reverse bias voltage (V_{abs} = 4.6 V). First column: measured d-scan traces for a drive current increasing from 220 mA to 280 mA. Second column: retrieved d-scan traces using the self-calibrating algorithm. Third column: d-scan trace simulation using the retrieved spectral phase, the measured spectral power, and the dispersion imparted by the compressor, for comparison. Fourth column: measured spectral power (black) and retrieved spectral phase (red) for the compressed pulse. For I_{gain} = 253.5 mA, the green curve was obtained by using the max hold function on the OSA. Fifth column: retrieved average pulse in the time domain, both compressed (blue) and uncompressed (red). 76
5.6. Full map of the measured d-scan traces for different values of drive current (220 mA $\leq I_{gain} \leq$ 280 mA) and reverse bias voltage (3.6 V $\leq V_{abs} \leq$ 5.6 V). Since two different gratings were used for different drive conditions, the y-axis was renormalized to the GDD applied by the compressor, for a more direct comparison between d-scan traces. 79
5.7. Full map of the measured fundamental optical spectrum for different values of drive current (220 mA $\leq I_{gain} \leq$ 280 mA) and reverse bias voltage (3.6 V $\leq V_{abs} \leq$ 5.6 V). 80

5.8. Full map of the average temporal profile of the uncompressed (red) and compressed (blue) pulses for different values of drive current (220 mA $\leq I_{gain} \leq$ 280 mA) and reverse bias voltage (3.6 V $\leq V_{abs} \leq$ 5.6 V). 81
5.9. Full map of the measured RF spectrum for different values of drive current (220 mA $\leq I_{gain} \leq$ 280 mA) and reverse bias voltage (3.6 V $\leq V_{abs} \leq$ 5.6 V).....82
5.10. Instability metric map, together with the representation of the regions of different mode-locking regimes, obtained for the pulses from the QD laser for different values of drive current and reverse bias. 83
5.11. RF spectra obtained for the pulses driven at $V_{abs} = 3.6$ V and drive current of 240 mA (left) and 270 mA (right). 84
5.12. RF spectra (top row) and autocorrelation traces (bottom row) obtained for pulses driven at $V_{abs} = 5.6$ V and different drive currents.....85
5.13. HML regime d-scan simulation, with a base pulse with $GDD = 1.4ps^2$ and another pulse with $GDD = 2.1ps^2$ (a), $GDD = 1.8ps^2$ (b) and $GDD = 1.55ps^2$ (c). Base pulse with $GDD = 1.4ps^2$ d-scan trace for comparison (d). 86
5.14. Experimental setup for the passive suppression of Q-switching. U_{abs}: voltage source. I_{gain}: DC current source. L: lowpass filter. R: resistance. C: DC-block. a, g: absorber and gain section, respectively. Reproduced from [149]. 88
5.15. Experimental setup for the active suppresion of Q-switching. BT: Bias Tee. D: photodetector. BS: beam splitter. $Ampl.$: amplifier. Reproduced from [150]. 88

6.1. Measured average power from the QD mode-locked laser, as a function of drive current and reverse bias.....89
6.2. Setup for studying the amplification process using a semiconductor optical amplifier. The polarization paddles are used to match the polarization of the laser to the one that provides the higher amplification efficiency. 92
6.3. Amplified spontaneous emission (ASE) spectrum of the QD SOA, for fixed operating temperature and variable drive current (left), and fixed drive current and variable operating temperature (right). 93
6.4. Input (blue), output (green) and ASE (orange) spectra for pulses with $I_{gain} = 240$ mA and $V_{abs} = 5.2$ V, amplified in the SOA with an amplification current of 800 mA.....94
6.5. From left to right: measured d-scan trace for pulses from the QD laser driven at $I_{gain} = 240$ mA and $V_{abs} = 5.2$ V without amplification; and with amplification with the SOA driving current equal to 200; 500; and 800 mA.....95
6.6. Measured and retrieved d-scan trace for $I_{gain} = 240$ mA and $V_{abs} = 5.2$ V, amplified with the SOA driven at 800 mA. 96
6.7. Retrieved spectral power (top left) and phase (top right), as well as the uncompressed (bottom left) and compressed (bottom right) temporal profiles for the pulses at $I_{gain} = 240$ mA and $V_{abs} = 5.2$ V, amplified with the SOA driven at different amplification currents.....97
6.8. Temporal chirp of the pulses driven at $I_{gain} = 240$ mA and $V_{abs} = 5.2$ V, with and without amplification using the SOA at different amplification currents.....98
6.9. Average power (red), pulse duration (blue), and peak power (green) of the pulses obtained directly after the SOA (top row) and after the SOA + single-grating compressor (bottom row) for the pulses driven at $I_{gain} = 240$ mA and $V_{abs} = 5.2$ V. 98
6.10. Retrieved spectral power (top left) and phase (top right), as well as the uncompressed (bottom left) and compressed (bottom right) temporal profiles for the pulses at $I_{gain} = 220$ mA and $V_{abs} = 4.6$ V, amplified with the SOA driven at different amplification currents.....99

6.11. Temporal chirp of the pulses driven at $I_{gain} = 220\,\text{mA}$ and $V_{abs} = 4.6\,\text{V}$, with and without amplification using the SOA at different amplification currents.....100
6.12. Average power (red), pulse duration (blue), and peak power (green) of the pulses obtained directly after the SOA (top row) and after the SOA + single-grating compressor (bottom row) for the pulses driven at $I_{gain} = 220\,\text{mA}$ and $V_{abs} = 4.6\,\text{V}$. 100
6.13. Retrieved spectral power (top left) and phase (top right), as well as the uncompressed (bottom left) and compressed (bottom right) temporal profiles for the pulses at $I_{gain} = 230\,\text{mA}$ and $V_{abs} = 5.6\,\text{V}$, amplified with the SOA driven at different amplification currents.....101
6.14. Temporal chirp of the pulses driven at $I_{gain} = 230\,\text{mA}$ and $V_{abs} = 5.6\,\text{V}$, with and without amplification using the SOA at different amplification currents.....102
6.15. Average power (red), pulse duration (blue), and peak power (green) of the pulses obtained directly after the SOA (top row) and after the SOA + single-grating compressor (bottom row) for the pulses driven at $I_{gain} = 230\,\text{mA}$ and $V_{abs} = 5.6\,\text{V}$. 102
6.16. Left: Evolution of the amplified optical spectrum from the pulses driven at $I_{gain} = 230\,\text{mA}$ and $V_{abs} = 3.6\,\text{V}$, amplified in the SOA with varying amplification currents. Right: evolution of the optical power of the amplified pulses as a function of the SOA drive current. The blue line serves as a guide for the eyes.....103
6.17. Experimental measurements for the amplification of an unstable pulse train, driven at $I_{gain} = 230\,\text{mA}$ and $V_{abs} = 3.6\,\text{V}$. First column: measured d-scans for an amplification drive current increasing from 0 mA to 800 mA. Second column: retrieved d-scan traces using the self-calibrating algorithm. Third column: d-scan trace simulation using the retrieved spectral phase, the measured spectral power, and the dispersion imparted by the compressor, for comparison. Fourth column: measured spectral power (black) and retrieved spectral phase (red) for the compressed pulse. Fifth column: retrieved average pulse in the time domain, both compressed (blue) and uncompressed (red). 104
6.18. Evolution of the instability metric of the amplified pulses with the amplification current.105

List of Abbreviations

A-PPLN Aperiodically-Poled Lithium Niobate

ASE Amplified Spontaneous Emission

BBO Beta Barium Borate

CEP Carrier-Envelope Phase

CW Continuous Wave

d-scan Dispersion-scan

DCM Dispersion Compensation Mirror

DWELL Dots in a WELL

ES Excited State

FWHM Full-Width at Half-Maximum

FROG Frequency-Resolved Optical Gating

GDD Group Delay Dispersion

GS Ground State

GVD Group Velocity Dispersion

HML Harmonic Mode-Locking

MLL Mode-Locked Laser

PM Phase-Matching

PPLN Periodically-Poled Lithium Niobate

QD Quantum Dot

RF Radio-Frequency

RR Repetition Rate

SA Saturable Absorber

SHG Second-Harmonic Generation

SOA Semiconductor Optical Amplifier

SPIDER Spectral Phase Interferometry for Direct Electric-field Reconstruction

SPM Self-Phase Modulation

STHG Surface Third-Harmonic Generation

TEP Trailing Edge Plateau

TL Transform-Limit

TOD Third-Order Dispersion

List of Publications

T. Gomes*, M. Canhota*, and H. Crespo, ”Temporal characterization of broadband femtosecond laser pulses by a surface third-harmonic dispersion scan with ptychographic retrieval,” *Optics Letters*, vol. 47, no. 15, pp. 3660–3663, 2022

In preparation

● T. Gomes, H. Crespo and M. Cataluna, ”Design and development of a highly-sensitive dispersion-scan setup for the characterization of low-power, picosecond pulses.”

● T. Gomes, H. Crespo and M. Cataluna, ”Pulse characterization and compression of mode-locked laser diodes using dispersion-scan.”

● T. Gomes, B. Alonso, H. Crespo and M. Cataluna, ”Detection and quantification of pulse train instabilities in semiconductor monolithic mode-locked laser diodes using self-calibrating dispersion-scan.”

● T. Gomes, B. Alonso, H. Crespo and M. Cataluna, ”Amplification of semiconductor mode-locked laser diodes using semiconductor optical amplifiers.”

Talks

● T. Gomes, H. Crespo, and M. A. Cataluna, “Characterization and compression of ultrashort pulses from mode-locked laser diodes using dispersion-scan,” in CLEO 2023, Optica Publishing Group, 2023, STh3Q.3.

● T. Gomes, H. Crespo, and M. A. Cataluna, “Detection and investigation of pulse asymmetries in passively mode-locked quantum-dot laser diodes using dispersion-scan,” in Conference on Lasers and Electro-Optics/Europe (CLEO/Europe 2023) and European Quantum Electronics Conference (EQEC 2023), Optica Publishing Group, 2023, cb76.

Posters

● T. Gomes, B. Alonso, H. Crespo, and M. A. Cataluna, “Quantification of pulse train instabilities in mode-locked quantum-dot laser diodes,” in CLEO 2024, Optica Publishing Group, 2024, JTu2A.29.

*These authors contributed equally to this work.

● T. Gomes, H. Crespo and M. A. Cataluna, ”Bringing ultrafast laser diodes to the masses by developing new pulse diagnostic tools,” in STEM for Britain, London, 2023.

Other Conference Proceedings

● A. F. Ribeiro, T. Gomes, and M. A. Cataluna, “High-speed optical sampling by dynamic repetition rate tuning of an optically injected mode-locked laser diode,” in Conference on Lasers and Electro-Optics/Europe (CLEO/Europe 2023) and European Quantum Electronics Conference (EQEC 2023), Optica Publishing Group, 2023, cf72.

● A. F. Ribeiro, T. Gomes, and M. A. Cataluna, “High-speed optical sampling with an optically injected mode-locked laser diode,” in 2023 Conference on Lasers and Electro-Optics (CLEO), 2023, pp. 1–2.

● A. F. Ribeiro, T. Gomes, and M. A. Cataluna, “Subharmonic optical injection locking of a mode-locked laser diode,” in 2023 Conference on Lasers and Electro-Optics Europe European Quantum Electronics Conference (CLEO/Europe-EQEC), 2023, pp. 1–1.

● A. F. Ribeiro, T. Gomes, and M. A. Cataluna, “High-speed and wide repetition rate tuning of dual-tone optically injected mode-locked quantum-dot lasers,” in 2022 28th International Semiconductor Laser Conference (ISLC), 2022, pp. 1–2.

Awards

● Professor Julian Jones prize, at School of Engineering and Physical Sciences, Heriot-Watt University, Scotland, UK.

1. Introduction

Light itself is extraordinary on its own. However, when the laser effect was discovered and the first laser was invented in 1960 [1], using a synthetic ruby cylinder with silver-coated ends as the Fabry-Perot resonator and photographic flash lamps as the pump source, creating laser flashes with ms of time duration, an optical revolution started, and the concept of laser pulses, as in flashes of coherent light, started to appear. This concept was expanded to the nanosecond (10^{-9} s) regime, with the creation of the Q-switching technique [2], which rapidly extended to the pico- (10^{-12} s) and the femtosecond (10^{-15} s) regime with the mode-locking technique [3], creating the concept of an ultrashort pulse.

1.1. Motivation

The possibility of having ultrashort laser pulses with high peak power and low average power allows their usage in applications such as micro-machining [4–6], and photo-ablation of biological tissue without thermal effects [7], useful for precise and contactless eye surgery [8]. Their broadband spectrum allows for tissue imaging, using techniques such as nonlinear optical microscopy [9] or Optical Coherence Tomography (OCT) [10, 11]. Lasers with a high repetition rate serve their purpose in telecommunications, where applications include ultra-high bit rate optical communication [12] and femtosecond signal processing [13, 14]. Pump-probe configurations with these lasers allow the study of a vast array of fields, from magnetization dynamics [15, 16] to the real-time monitoring of chemical reactions [17]. The creation of frequency combs has made a great impact in the field of optical metrology [18]. Generating attosecond (10^{-18} s) laser pulses enables unprecedented resolution in pump-probe measurements [19]. There is no limit to what ultrafast laser systems can achieve [20, 21].

In the vast range of ultrafast lasers, semiconductor laser diodes are a compact, electrically pumped, and wall-plug efficient source for generating ultrashort laser pulses. With semiconductor material in the gain section, these lasers generate light through stimulated emission where, by applying a forward bias to a doped p-n junction, a photon can induce the recombination of an electron-hole pair, creating another photon with the same wavelength and direction of propagation. For high enough drive currents, coherent light is created [22].

The existence of a compact, wall-plug efficient, and low-cost laser source that can generate ultrashort pulses seems like the ultrafast Holy Grail. However, the widespread adoption of these laser sources is not a reality yet. So, what is the problem?

It is still not possible to harness the full capabilities of ultrafast laser diodes and achieve mode-locking regimes with higher optical output power, since driving them at higher gain currents creates pulse train instabilities [23–26]. To better understand the instabilities that occur in semiconductor laser diodes, it is crucial to identify and quantify them, to gain privileged information into the stability of the mode-locking regime, inform theoretical work, and develop strategies to minimize or even eliminate such instabilities. In this work, we use the dispersion-scan [27, 28], a pulse characterization technique that strongly relies on nonlinear optics and dispersion to measure ultrashort laser pulses, to gain further insights into the pulse generation mechanisms and stability regimes of semiconductor laser diodes. This thesis is divided as follows:

Chapter 1 provides a brief introduction to the description of ultrashort laser pulses, namely pulse generation, mathematical formulation, and characterization, as well as a brief introduction to nonlinear optics.

Chapter 2 presents a d-scan setup, developed at University of Porto, based on surface third-harmonic generation, used to characterize and compress sub-10 fs pulses from a Ti:Sapphire oscillator. This work is a culmination of previous work initiated prior to the beginning of this PhD.

In Chapter 3 we present a highly-sensitive d-scan setup, developed at Heriot-Watt University, able to characterize pulses with low energy and long (ps) durations. We use it to characterize and compress pulses from a semiconductor laser diode to the sub-ps regime.

This setup was used in Chapter 4 to characterize and compress (to a sub-ps regime) pulses from a quantum-dot mode-locked laser, as well as to investigate the pulse generation dynamics with the laser driving conditions. We have correlated our findings with theoretical models and previous experimental measurements with similar laser sources.

In Chapter 5, we show, for the first time, the quantification of pulse train instabilities in semiconductor laser diodes using the self-calibrating retrieval algorithm. We have detected different mode-locking regimes depending on the laser driving conditions.

The study of the amplification process using semiconductor optical amplifiers is presented in Chapter 6, where we analyze the influence of the amplification process on the pulses'

spectra and temporal profile. We also investigate the amplification of unstable pulse trains.

Chapter 7 presents the main conclusions and the outlook for the near future.

1.2. Mathematical description

Ultrashort laser pulses consist of electromagnetic wave packets with a few picoseconds or less of time duration. They can be described in the time domain as a complex vector [29, 30]:

$$\vec{E}(\vec{r},t) = |\vec{E}(\vec{r},t)|e^{i\varphi(\vec{r},t)}\hat{e}(\vec{r},t) \tag{1.1}$$

where $\varphi(\vec{r},t)$ is the temporal time- and space-dependent phase of the ultrashort laser pulse, and $\hat{e}(\vec{r},t)$ is the polarization direction vector. To get to the frequency domain, we can apply the Fourier transform to the above equation and, assuming we are only dealing with linearly polarized laser pulses $\vec{E}(\vec{r},t) = E(\vec{r},t)\hat{e}$, where $\hat{e}$ is fixed and dictates the polarization direction:

$$E(\vec{r},\omega) = \mathcal{F}\left[E(\vec{r},t)\right] = |\vec{E}(\vec{r},\omega)|e^{i\varphi(\vec{r},\omega)} \tag{1.2}$$

where $\varphi(\vec{r},\omega)$ is the spectral phase of the pulse, and $|\vec{E}(\vec{r},\omega)| = \sqrt{I(\vec{r},\omega)}$, $I(\vec{r},\omega)$ being the spectral power, which is typically measured with a spectrometer. For the purpose of this work, we are only interested in the time-varying component of the pulses, therefore we assume $E(\vec{r},\omega) \equiv E(\omega)$ and $\varphi(\vec{r},\omega) \equiv \varphi(\omega)$. This assumption is made accordingly to the laser sources used in this work.

Two of the most used temporal envelopes in the field of ultrashort laser science are those of Gaussian and $sech^2$ pulses. For the Gaussian pulses, the expression for the envelope is as follows:

$$|E(t)|^2 = e^{-\varrho t^2}; \varrho = \frac{2ln(2)}{\Delta t^2} \tag{1.3}$$

where Δt is the full-width at half-maximum (FWHM) of the pulse. The expression for the envelope of a $sech^2$ pulse is written as:

$$|E(t)|^2 = sech^2\left(\frac{t}{\kappa}\right); \kappa = \frac{\Delta t}{ln\left(3+2\sqrt{2}\right)} \tag{1.4}$$

Let us take into account a Gaussian pulse. If we go to the frequency domain, employing a Fourier transform, we get another Gaussian profile, with spectral bandwidth $\Delta\omega$. It follows then, by the properties of the Fourier transform, that:

$$\Delta t \Delta\omega \geq K \tag{1.5}$$

where K is a constant that depends on the pulse shape ($K = 0.441$ for a Gaussian pulse and $K = 0.315$ for a $sech^2$ pulse) [31]. If the equality is observed, we say that the pulse is transform-limited (TL) and is the shortest pulse possible for a given spectrum. There is a strong resemblance between Equation 1.5 and Heisenberg's principle: to get a short pulse in the temporal domain (concentrated in time), we need a broad spectrum to support it (dispersed in frequency), and vice-versa.

1.3. Mode-locking

Due to the wave properties of light, a laser cavity with length l can support several longitudinal modes, which frequencies are separated by:

$$\Delta\nu = \frac{c}{2l} \tag{1.6}$$

where c is the speed of light in the cavity medium. If the relative phase of these modes is not controlled, then these modes do not interfere constructively. However, if the phase between these modes remains fixed, the modes interfere constructively, creating pulses in a process referred to as mode-locking. Figure 1.1 shows an example of constructive or destructive interference between modes in a cavity where the phases are either random or fixed.

Mode-locking allows for the generation of ultrashort pulses from laser sources [32], with a repetition rate equal to the mode spacing and a peak intensity that scales with N_m^2, N_m being the number of modes locked and emitted by the laser. We should note that the cavity can support an almost infinite number of modes, but only those that are within the gain bandwidth and above threshold are emitting.

The energy of the modes is now concentrated in time, which leads to a high peak power:

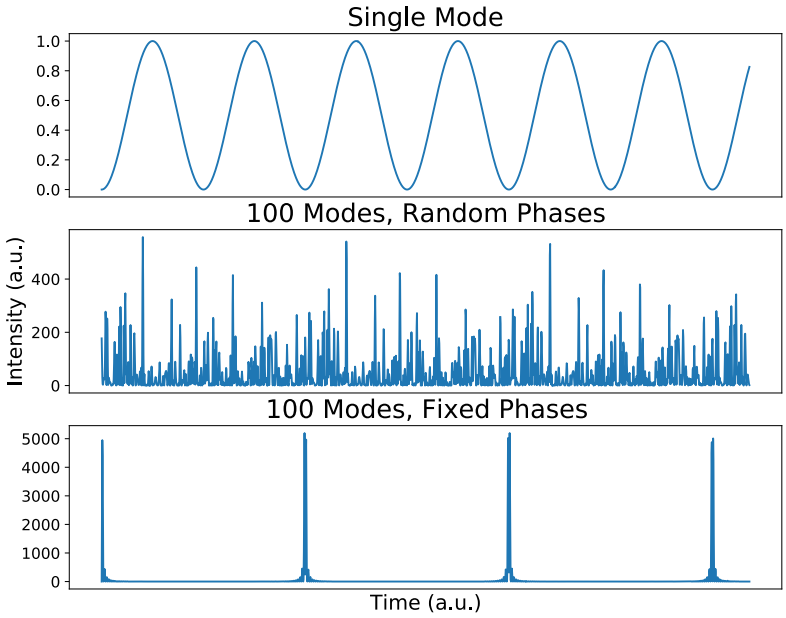


Figure 1.1: Intensity of a laser with a single mode (top), 100 modes with random phases (middle), and 100 modes with locked phases (bottom).

$$P_{peak} = B\frac{E_p}{\Delta t} \tag{1.7}$$

where Δt is the pulse duration, B is a parameter that depends on the pulse shape (approximately 0.88 for $sech^2$ pulses and 0.94 for Gaussian pulses) and E_p is the pulse energy, equal to P_{av}/f_{rep}, P_{av} being the average power and f_{rep} being the repetition rate. This means that even with a low average power, the peak power can be extremely high, depending on the pulse duration.

1.4. Dispersion

If we expand the spectral phase into a Taylor series around the central frequency ω_0 of the pulse's spectrum, we get:

$$\varphi(\omega) = \varphi(\omega_0) + \frac{d\varphi}{d\omega}(\omega-\omega_0) + \frac{1}{2!}\frac{d^2\varphi}{d\omega^2}(\omega-\omega_0)^2 + \frac{1}{3!}\frac{d^3\varphi}{d\omega^3}(\omega-\omega_0)^3 + ... \tag{1.8}$$

The above expansion is extremely useful since we can now determine the effect of each term on the temporal profile of an ultrashort pulse. $\varphi(\omega_0)$ is defined as the Carrier Envelope Phase (CEP) and is a constant phase offset. For few-cycle laser pulses (where the carrier oscillates only a small number of times within the envelope) this phase is of extreme importance. However, it does not affect the temporal profile in the case of the

pulses investigated in this work (which contain many cycles), and therefore is not considered further in this thesis. The second term on the equation is directly dependent on the group delay $t_g = d\varphi/d\omega$. If $t_g(\omega)$ is constant for all frequencies, it translates to a pulse delay in the time domain. However, if we consider higher-order dispersions, the group delay becomes dependent on the frequency, and the pulse will suffer time distortions.

The first term that starts changing the pulse temporal shape is the Group Delay Dispersion $GDD = d^2\varphi/d\omega^2 = dt_g/d\omega$, consisting of a linear chirp, which results from a quadratic spectral phase. In the temporal domain, GDD creates a pulse broadening by lagging higher frequencies compared to shorter ones (if the GDD is positive). If the value of GDD is known, it can be used to crudely estimate the pulse elongation by measuring the pulse duration Δt after dispersion:

$$\Delta t = \Delta t_0 \sqrt{1 + \left(4ln2\frac{GDD}{\Delta t_0^2}\right)^2} \tag{1.9}$$

where Δt_0 is the initial pulse width (assuming a Gaussian profile).

The Third Order Dispersion $TOD = d^3\varphi/d\omega^3 = d^2t_g/d\omega^2$ is a quadratic chirp, stemming from a cubic spectral phase. The contribution of TOD affects the pulse less than the GDD, but its effects can still be visible, consisting of the creation of pre- or post-pulses, depending on its sign.

To better visualize the effects of these terms in the pulse's temporal profile, we have simulated an ultrashort pulse with a center wavelength of 1264 nm, yielding a transform-limited (TL) pulse of around 510 fs. We have applied independently to each simulated pulse a Group Delay of $2.7\ ps$, a GDD of $0.36\ ps^2$, and a TOD of $0.09\ ps^3$, whose respective temporal profiles can be seen in Figure 1.2.

1.4.1 Dispersion Compensation

In the previous section, we have only applied dispersion with a positive sign, where components in the pulse with higher frequency are delayed with respect to the ones with lower frequency (in more colloquial terms, we can say that the "blues" are delayed with respect to the "reds"). Dispersion with a positive sign occurs normally in pulse propagation in a material and is typically not desired since it creates a pulse broadening in the time domain. Therefore, one must find a way to reverse this effect, either by reversing this delay or making the components with a higher frequency travel a smaller distance compared to

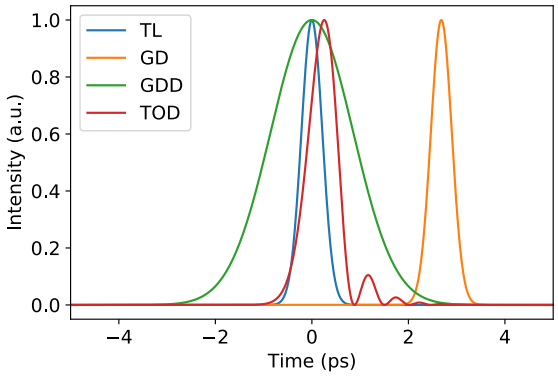


Figure 1.2: Temporal effects of a linear (GD - Group Delay), quadratic (GDD - Group Delay Dispersion), and cubic (TOD - Third Order Dispersion) phase on a transform-limited (TL) pulse (blue curve). Further numerical details in text.

the ones with a lower frequency, which is equivalent to a negative dispersion. The three better known techniques to apply negative dispersion are prism compression, chirped mirrors, and grating compression.

Prism compression [33] relies on changing the optical path of components with different frequencies using refraction on prisms. If done correctly, this creates a negative dispersion, as seen in Figure 1.3.

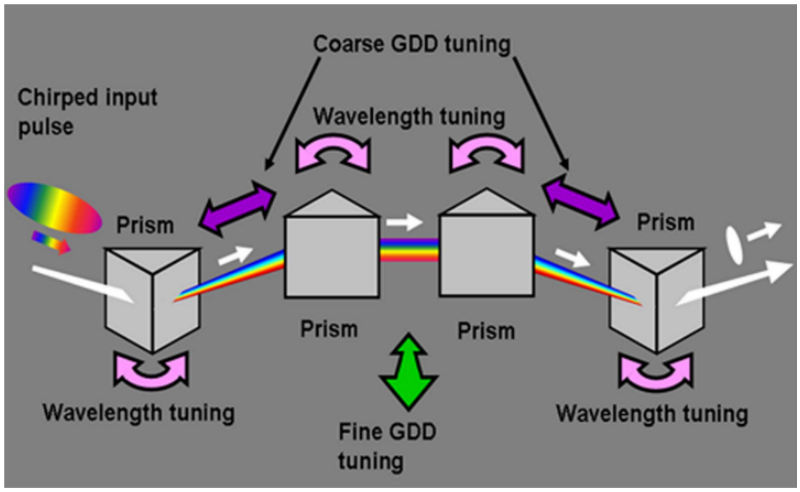


Figure 1.3: Schematic of a standard prism compressor. Reproduced from [34].

A similar setup is used for the grating compressor [35], but with gratings instead of prisms and using the properties of grating diffraction to create negative dispersion. A variation of this grating compressor will be used in the work developed throughout this thesis. More details will be presented in chapter 3.

Another well-known approach is the use of dispersion compensation mirrors (DCMs) [36] which are composed of several layers of unevenly spaced dielectric layers, each with

alternating refractive index. This introduces a net negative dispersion since components with higher frequencies are reflected at layers closer to the surface, while components with lower frequencies are reflected far away from the surface. (see Figure 1.4 for more details).

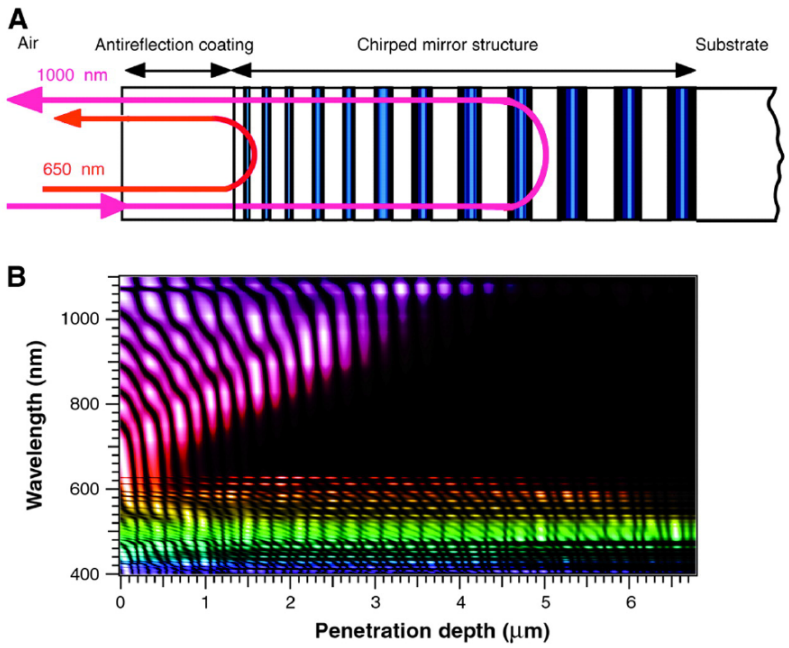


Figure 1.4: (a) Structure of a DCM with alternating layers with different refractive index and thickness. (b) Penetration depth as a function of wavelength for the DCM, which provides negative dispersion in the 650 to 1050 nm region. Reproduced from [37].

1.5. Nonlinear Optics

For relatively low peak intensities, the interaction between light and matter can typically be described with a linear model, where the polarization of a material is only linearly affected by the light interacting with it. However, since ultrashort laser pulses have very short temporal durations, it is feasible to assume that they have a strong peak intensity. In these cases, the linear model fails, and there is a need for a nonlinear model of light-matter interaction. This effect gives rise to the nonlinear optics field, which studies the nonlinear interaction between light and matter (and between light and itself). In this section, we will give a brief theoretical description of the most common nonlinear optical effects, such as second harmonic generation (SHG) and third harmonic generation (THG).

The model begins with the wave equation for nonmagnetic materials without free carriers:

$$\nabla \times \nabla \times \vec{E}(\vec{r},t) - \frac{1}{c^2}\frac{\partial^2 \vec{E}(\vec{r},t)}{\partial t^2} = \frac{1}{\epsilon_0 c^2}\frac{\partial^2 \vec{P}(\vec{r},t)}{\partial t^2} \tag{1.10}$$

which can be rewritten in the frequency domain as:

$$\nabla \times \nabla \times \vec{E}(\vec{r},\omega) + \frac{\omega^2}{c^2}\vec{E}(\vec{r},\omega) = -\frac{1}{\epsilon_0 c^2}\omega^2 \vec{P}(\vec{r},\omega) \tag{1.11}$$

If the light intensity is weak, then only a linear polarization $\vec{P}(t) = \epsilon_0 \chi^{(1)} \vec{E}(t)$ is created, where ϵ_0 is the vacuum permittivity and $\chi^{(1)}$ is the electric susceptibility of the medium. If, however, the light intensity is high, and the light electric field becomes comparable to the atomic electric field that binds an electron to an atom, we must expand the polarization as a multilinear function of the electric field:

$$P_i = \epsilon_0 \left(\sum_j \chi^{(1)}_{ij} E_j(t) + \sum_{j,k} \chi^{(2)}_{ijk} E_j(t) E_k(t) + \sum_{j,k,l} \chi^{(3)}_{ijkl} E_j(t) E_k(t) E_l(t) + ... \right) \tag{1.12}$$

where P_i is the i-th Cartesian coordinate of the polarization, and $\chi^{(2)}_{ijk}$ and $\chi^{(3)}_{ijkl}$ are the second and third-order nonlinear optical susceptibility tensors, respectively. The expansion extends indefinitely, however, for the purpose of this thesis, we are only interested in the second and third-order terms.

1.5.1 Second Harmonic Generation

If we consider a linear polarization, for the second-order term we get a scalar polarization:

$$P^{(2)}(t) = \epsilon_0 \chi^{(2)} E^2(t) \tag{1.13}$$

Let's assume that the electric field can be described as a superposition of two monochromatic sinusoidal waves with frequencies ω_1 and ω_2 and amplitudes E_1 and E_2, respectively:

$$E(t) = E_1 e^{-i\omega_1 t} + E_2 e^{-i\omega_2 t} + c.c. \tag{1.14}$$

where $c.c.$ stands for the complex conjugate. In this case, the nonlinear polarization is written as:

$$\begin{aligned} P^{(2)}(t) = \epsilon_0 \chi^{(2)} [&E_1^2 e^{-2i\omega_1 t} + E_2^2 e^{-2i\omega_2 t} + 2E_1 E_2 e^{-i(\omega_1+\omega_2)t} \\ &+2E_1 E_2^* e^{-i(\omega_1-\omega_2)t} + 2E_1 E_1^* + 2E_2 E_2^* + c.c] \end{aligned} \tag{1.15}$$

The first two terms inside the brackets are called second harmonic generation (SHG), which consists on the generation of light with a frequency that is double of the original - $2\omega_1$ and $2\omega_2$, in this case. The third and fourth terms are sum-frequency generation (SFG) and difference-frequency generation (DFG), respectively, which generate light with a frequency that is the sum or the difference of the original frequencies, respectively.

1.5.2 Phase Matching

It is rather intuitive to think that by increasing the power of the fundamental field the generated nonlinear power would increase as well. Although this is true, it is not that simple, and other relevant considerations must be made. Let us take into account the second harmonic generation effect, described by the following wave equation:

$$\nabla^2\vec{E} - \frac{n^2}{c^2}\frac{\partial^2\vec{E}}{\partial t^2} = \frac{\partial^2\vec{P}_{NL}}{\partial t^2} \tag{1.16}$$

where $\vec{P}_{NL}$ is the nonlinear polarization vector. By assuming a monochromatic wave, it can be easily demonstrated that the output power of the SHG P^{SHG}_{power} is proportional to:

$$P^{SHG}_{power} \propto sinc^2\left(\frac{\Delta k}{2}L\right)L^2 \tag{1.17}$$

where L is the thickness of the nonlinear medium and $\Delta k = k_2 - 2k_1$ is the phase-mismatch, where k_2 is the wavenumber of the second harmonic signal and k_1 the wavenumber of the fundamental field. Since the refractive index is normally a monotonic function of the wavelength, it is impossible to nullify the phase mismatch for a material with a single refractive index. However, for materials with two or more refractive indexes (such as uniaxial crystals, e.g., Beta-Barium Borate (BBO) and Potassium Dideuterium Phosphate (KDP), which have an ordinary refractive index n_o and an extraordinary refractive index n_e, depending on the crystal direction), the refractive index n changes with the angle of incidence of the light beam on the optical axis of the material, θ:

$$\frac{1}{n^2(\theta)} = \frac{cos^2(\theta)}{n_o^2} + \frac{sin^2(\theta)}{n_e^2} \tag{1.18}$$

and we can now minimize or even nullify the phase mismatch $\Delta k(\theta,\omega) = k(\theta,2\omega) - 2k(\omega)$ simply by tuning the angle θ.

1.5.3 Third Harmonic Generation

Using the same expression for the electric field from Equation 1.14, and analyzing the third-order term of the polarization:

$$P^{(3)}(t) = \epsilon_0 \chi^{(3)} E^3(t) \tag{1.19}$$

there are going to be terms of the form $\epsilon_0 \chi^{(3)} E_1^3 e^{-3i\omega_1 t}$ and $\epsilon_0 \chi^{(3)} E_2^3 e^{-3i\omega_2 t}$, which are referred to as third harmonic generation (THG), consisting on the generation of light with triple of the original frequency of each monochromatic wave. This effect is also affected by the phase-matching conditions.

1.5.4 Self-phase modulation

If the intensity of the laser pulse is strong enough, the refractive index of the material where it is propagating changes with the instantaneous intensity:

$$n(I) = n_0 + n_2 I \tag{1.20}$$

where n_0 is the linear refractive index and n_2 is the nonlinear refractive index (which depends on the third order nonlinear optical susceptibility $\chi^{(3)}$). Since the pulse intensity is strongly time-dependent, the refractive index seen by the pulse will be time-dependent as well, which in turn dictates the phase acquired by the pulse during propagation:

$$\phi_{SPM}(t) = \frac{2\pi z}{\lambda_0} n(I) \tag{1.21}$$

where λ_0 is the carrier wavelength and z is the propagation length. The time derivative of the phase gives the instantaneous frequency:

$$\omega(t) = \omega_0 - \frac{d\phi_{SPM}(t)}{dt} \tag{1.22}$$

This effect is called self-phase modulation (SPM) and generates new frequencies in the laser spectrum during the pulse propagation in the nonlinear medium.

1.6. Ultrashort Laser Pulse Characterization

As the pulse duration gets shorter, measuring ultrashort pulses becomes more difficult, since there are no detectors with such fast response times. In this regard, techniques that strongly rely on nonlinear effects have been developed, that allow either to provide estimates of the pulse duration, such as autocorrelation [38], or to provide the full spectrum and spectral phase of the pulse, allowing for a full characterization of an ultrashort pulse. Some of these techniques are Frequency Resolved Optical Gating (FROG) [39], Spectral Phase Interferometry for Direct Electric-field Reconstruction (SPIDER) [40], Multiphoton Intrapulse Interference Phase Scan (MIIPS) [41] and dispersion-scan [27, 28].

1.6.1 Intensity autocorrelation

In this technique, two replicas of the fundamental pulse are produced via a beam splitter, where one of the replicas can be delayed with respect to the other. If the two replicas interfere nonlinearly, for example in a SHG crystal, the resulting signal can be measured in a photodetector, giving rise to an intensity autocorrelation trace $A(\tau)$:

$$A(\tau) = \int_{-\infty}^{+\infty} I(t)I(t-\tau)dt \tag{1.23}$$

where τ is the delay between both replicas and $I(t)$ is the intensity of the pulse (see Figure 1.5 for further details about the experimental setup). If the replicas are non-collinear, then the SHG is spatially separated from the fundamental beam, and the measurement can be made background-free. With knowledge of the intensity autocorrelation, and assuming a certain pulse shape, it is possible to estimate the duration of the pulse from that of the autocorrelation measurement. However, it cannot provide information about the pulse shape, since two different pulses can have the same autocorrelation.

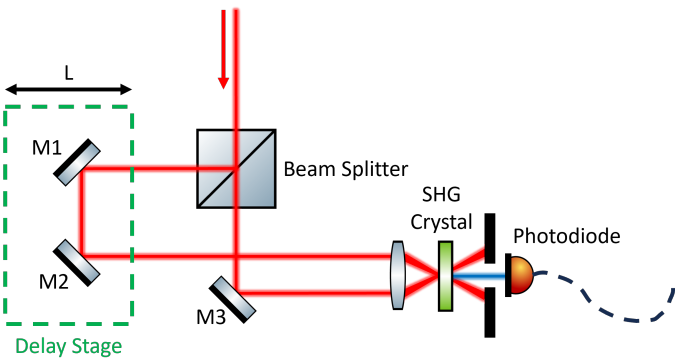


Figure 1.5: Second-order noncollinear autocorrelation setup.

1.6.2 Frequency-Resolved Optical Gating

By frequency-resolving the nonlinear signal obtained with an autocorrelation measurement (by using, for example, a spectrometer instead of a photodetector), and measuring it as a function of the delay between replicas, we obtain the FROG trace:

$$I_{FROG}(\omega,\tau) = \left| \int_{-\infty}^{+\infty} E_{sig}(t,\tau) e^{-i\omega t} dt \right|^2 \tag{1.24}$$

where $E_{sig}(t,\tau) = E(t)E(t-\tau)$ for the second harmonic FROG trace. Using appropriate retrieval algorithms, a spectral power and phase can be calculated, by optimizing these variables in a way that minimizes the difference between the measured FROG trace and the simulated FROG trace using these variables. Some retrieval algorithms will be described later.

1.6.3 Spectral Phase Interferometry for Direct Electric-field Reconstruction

The SPIDER technique is a self-referenced technique [42], and consists on interfering two replicas of the pulse, created using a Michelson interferometer, with a highly chirped version of itself, that are recombined in a nonlinear crystal to perform sum-frequency generation (see Figure 1.6 for further experimental details).

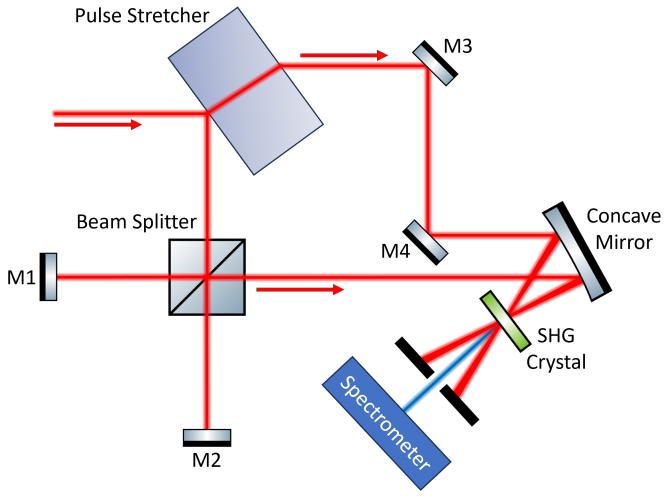


Figure 1.6: SPIDER experimental setup.

This interferogram is then measured with a spectrometer. The obtained interferogram can be written as [43]:

$$T(\omega) = D^{(DC)}(\omega) + e^{-i\omega\tau} D^{(-AC)}(\omega) + e^{i\omega\tau} D^{(+AC)}(\omega) \tag{1.25}$$

where $D^{(DC)}(\omega)$ is a DC component that does not contain any information, τ is the temporal delay between the replicas, and:

$$D^{(\pm AC)}(\omega) = |\tilde{E}(\omega-\Omega)\tilde{E}(\omega)|exp\{\mp i[\varphi(\omega)-\varphi(\omega-\Omega)]\} \tag{1.26}$$

is the AC component, where Ω is the spectral shear. This shear can be understood by the chirped pulse having a linearly time-dependent instantaneous frequency, which means that each replica created in the Michelson interferometer interferes with a different frequency of the chirped pulse. With an inverse Fourier transform, to go to the time domain, and another secondary measurement without shear, the spectral power and phase can be directly computed from this measurement, making this a very powerful technique, although extremely complicated to implement.

1.6.4 Multiphoton Intrapulse Interference Phase Scan

The MIIPS technique relies on the use of a pulse shaper, based on a liquid-crystal spatial light modulator (SLM), to measure and compress a pulse. The pulse to be measured traverses the pulse shaper, that imprints a spectral phase $\phi(\omega)$. The beam then goes through a SHG crystal and generates a nonlinear signal, which is then detected as a function of the phase applied by the compressor. In the frequency domain, the pulse can be described as written in Equation 1.2. The total SHG signal is given by [44]:

$$I(\omega) = \left| \int_{-\infty}^{+\infty} |E(\omega+\Omega)||E(\omega-\Omega)|e^{i\{\phi(\omega+\Omega)+\phi(\omega-\Omega)\}}d\Omega \right|^2 \tag{1.27}$$

In this case, for each frequency ω, there is a value of $\phi(\omega)$ that maximizes the nonlinear signal. With this information, the spectral phase is completely retrievable, allowing to fully characterize the measured pulse.

1.6.5 Dispersion-scan

Dispersion-scan (d-scan) is a technique that relies on the effect of the spectral phase of the pulse being measured on the nonlinear effect that it can produce. By measuring a frequency-resolved nonlinear signal, as for example the second-harmonic generation (SHG), as a function of the dispersion applied to the laser pulse, by use of a standard

compressor, we can measure a 2D d-scan trace which, through appropriate retrieval algorithms, can be used to fully retrieve both the spectral power and the spectral phase of the pulse being studied (see the diagram from Figure 1.7 for a better comprehension).

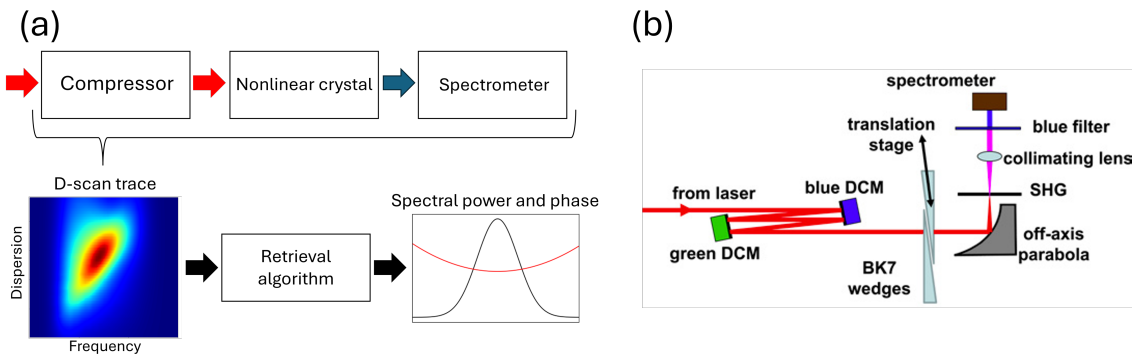


Figure 1.7: (a) General schematics of a dispersion-scan setup and retrieval procedure. (b) Typical d-scan experimental setup [27].

To better understand the process of a d-scan measurement, let us begin with its mathematical description. In the frequency domain, the pulse can be described as written in Equation 1.2. Assuming that there is no spatial variation, we can focus only on the frequency-varying component of the pulse $E(\vec{r},\omega) = E(\omega)$. If we apply a spectral phase $\phi(\omega,z)$ to the pulse, we get:

$$E(\omega) \rightarrow |E(\omega)|e^{i\varphi(\omega)}e^{i\phi(\omega,z)} \tag{1.28}$$

The spectral phase that is applied must depend on some variable z, which can be the thickness of a dispersive material, the distance between two gratings, or other variables depending on the type of compressor used.

The next step in the d-scan setup consists of the nonlinear signal generation. If we consider SHG, in the time domain it simply consists of squaring the pulse itself:

$$E(\omega,z) \rightarrow E(t,z) = \mathcal{F}^{-1}\left[|E(\omega)|e^{i\varphi(\omega)}e^{i\phi(\omega,z)}\right]^2 \tag{1.29}$$

To measure the nonlinear signal, we must go back to the frequency domain (which is the physical equivalence of measuring a signal in a typical spectrometer) and measure the intensity of the nonlinear signal:

$$E(t,z) \rightarrow T(\omega,z) = \left| \mathcal{F}\left[\mathcal{F}^{-1}\left[|E(\omega)| e^{i\varphi(\omega)} e^{i\phi(\omega,z)} \right]^2 \right] \right|^2 \tag{1.30}$$

where $T(\omega,z)$ is the measured d-scan trace (henceforth called $T_{meas}(\omega,z)$).

It is straightforward to simulate a d-scan trace, normally discretized into a matrix with N_ω frequency points and N_z dispersion points, if we have a known spectral power and phase. The contrary, however, is not that simple. We have to resort to different methods to retrieve the spectral power and phase. The retrieval process, therefore, now consists of, after having a measured d-scan trace, finding the spectral power and phase that produce a d-scan trace $T_{sim}(\omega,z)$ that resembles the measured one the most. The measurement of the quality of a retrieval is made through the error function G:

$$G = \sqrt{\frac{1}{N_\omega N_z} \sum_{i,j} \left(T_{meas}(\omega_i,z_j) - \mu_i T_{sim}(\omega_i,z_j) \right)^2} \tag{1.31}$$

The function $\mu(\omega)$ is a parameter called the response function, which indirectly takes into account aspects such as phase-matching, pulse propagation inside the nonlinear medium, spectrometer response function, among others. It can be found by differentiating G with respect to μ, leading to:

$$\mu_i(\omega) = \frac{\sum_j T_{meas}(\omega_i,z_j) T_{sim}(\omega_i,z_j)}{T^2_{sim}(\omega_i,z_j)} \tag{1.32}$$

It is more intuitive to measure the G error as a percentage, normalizing it by the energy of the d-scan trace:

$$G = \sqrt{\frac{\sum_{i,j} \left(T_{meas}(\omega_i,z_j) - \mu_i T_{sim}(\omega_i,z_j) \right)^2}{\sum_{i,j} (T_{meas}(\omega_i,z_j))^2}} \tag{1.33}$$

The retrieval of the spectral power and phase is made typically through optimization algorithms, where the aim is to minimize the error function G. Several retrieval algorithms have been applied to the dispersion-scan technique, such as multi-variable optimization algorithms like the Nelder-Mead algorithm [28]. Other optimization algorithms have been used more recently [45–48], as well as deep neural networks [49]. However, we will use two different retrieval algorithms for the purpose of this work: the ptychographic retrieval and the self-calibrating d-scan retrieval. More details will be presented later in the thesis.

1.7. Purpose of this thesis

Currently established techniques do not provide significant information on the pulse train instabilities themselves. Autocorrelation traces of unstable pulses present a coherent artifact peak at zero time delay. Still, no quantitative information can be extracted from these measurements - except for an average time duration of the unstable pulse train. Frequency-resolved optical gating (FROG) can be used to qualitatively separate the contributions of the average pulse and the coherent artifact [50], but the quantification of these instabilities remains a problem to be solved since the retrieval algorithms fail as soon as the pulses become unstable which, with the added difficulty of some instabilities being invisible to these pulse characterization techniques [51], making the pulse train instabilities quantification a problem yet to be solved in pulse trains from ultrafast laser diodes. In this thesis, we have developed a highly-sensitive dispersion-scan setup, capable of compressing and characterizing pulses with energies as low as a few hundred fJ and ps time duration. With this setup, we have achieved sub-ps ultrashort, stable pulses from QD passively mode-locked laser diodes. By using the self-calibrating d-scan retrieval, we have, for the first time, quantified pulse train instabilities in semiconductor laser diodes and have studied the influence of driving conditions on these instabilities, as well as observed different mode-locking regimes. We have also used a QD semiconductor optical amplifier (SOA) to further increase the output power of these laser sources and investigated the influence of the amplification process on the chirp, instability, and overall behavior of the laser pulses. With this new knowledge, we hope that these results pave the way to shorter and more energetic pulses directly from semiconductor laser diodes based on quantum dot materials.

2. Surface third-harmonic dispersion-scan with ptychographic retrieval

This chapter contains the first results obtained in University of Porto, where we have developed a new variant of the dispersion-scan technique, using surface third-harmonic generation as the nonlinear signal, which allows retrieving pulses with arbitrary frequency and bandwidth, only limited by the detection method. We have used this technique to retrieve sub-10 fs ultrashort pulses from a Ti:Sapphire oscillator using a ptychographic retrieval with a filter correction, being the first implementation of the ptychographic retrieval for ultrabroadband laser sources and, therefore, adequate for few-cycle pulses. The results shown in this chapter were published in ref. [52].

2.1. Introduction

Although the first implementation of the d-scan technique used second harmonic generation as the nonlinear signal generation, several other variations have been implemented. Implementations based on third-order nonlinearities, such as third-harmonic generation [53, 54], cross-polarized wave (XPW) [55–57], self-diffraction (SD) [58, 59] and third-harmonic *in situ* (THIS) [60], have been done, each implementation with its advantages. The most commonly used nonlinear signal for a d-scan is SHG. However, this nonlinear effect can be problematic when dealing with octave-spanning sources, due to the spectral overlap between the fundamental and SHG beams (although certain implementations of the d-scan take advantage of this overlap between these two beams to retrieve information about the carrier-envelope phase (CEP) [61], or to access the absolute CEP of the pulses *in situ* [62]. Third-harmonic generation has been demonstrated in d-scan using different nonlinear mediums, such as graphene [53] or thin films of $TiO_2 - SiO_2$ with bandgaps tailored for a particular spectral region [54]. However, these materials are not commonly available and must be manufactured, with the added difficulty that their phase-matching conditions change drastically for different spectral regions, which requires designing and manufacturing samples for each particular region.

Surface third-harmonic generation (STHG) in standard optical interfaces, such as glass or sapphire, could overcome these problems [63, 64]. Although having a lower efficiency than third-harmonic generation in specific nonlinear crystals, it occurs at all interfaces and

can be used to fully characterize the temporal profile of ultrashort pulses with arbitrary bandwidth and center frequency, limited only by the detection process.

STHG has been demonstrated at the air/dielectric interface of crystalline sapphire wafers at fundamental wavelengths of $1.595\,\mu$m [65], using a standard Si-based spectrometer to detect the nonlinear signal. By coupling a variable pulse compressor to this system, a simple d-scan setup can be realized that should enable the full characterization of the temporal profile of the used ultrashort pulses. Even for longer fundamental wavelengths, the generation and detection of the STHG signal should be straightforward. For example, a standard spectrometer with a silicon-based detector should enable d-scan measurements of pulses with center frequencies up to $3\,\mu$m. STHG-based FROG has been demonstrated with approximately 100 fs pulses [66] and more recently with sub-10-fs pulses in the visible [67] and near-infrared [68] regions. However, to the best of our knowledge, no STHG d-scan measurement using standard optical substrates has been reported so far.

In this work, we have developed a surface third-harmonic dispersion scan setup to compress and characterize 7 fs pulses from a Ti:Sapphire oscillator. The obtained results are in very good agreement with standard SHG d-scans using a BBO crystal, showing that STHG d-scan is a powerful tool to characterize ultrashort pulses, covering a wide spectral range.

2.2. Experimental setup

The experimental setup for STHG d-scan is given in Fig. 2.1. In our experiments, we used an ultra-broadband Ti:Sapphire laser oscillator (Femtolasers Rainbow CEP) delivering pulses with a central wavelength of 800 nm, sub-10-fs duration, 2.5 nJ of energy and a repetition rate of 80 MHz. Like in most d-scan implementations, the setup comprises three sections: a variable compressor (usually already in place and responsible for adjusting the total dispersion applied to the laser pulse), a nonlinear signal generator (where the STHG is performed) and a spectral measurement of the generated signal. In the variable compressor, the beam undergoes 8 bounces off ultra-broadband double-chirped mirrors (Laser Quantum Ltd) that introduce negative dispersion before crossing a pair of BK7-glass wedges for variable dispersion compensation. One of the wedges is connected to a motorized stage for scanning and fine-tuning the applied dispersion. The pulse energy is adjusted with a variable neutral-density filter prior to the nonlinear section, where the beam crosses a 0.5 mm thick sapphire substrate and is focused back on the same substrate with a concave silver-coated spherical mirror (f $= 5$ cm) at an incidence angle of 19° (a

smaller angle would have been preferable to minimize astigmatism, but this was the best compromise in our setup given our beam size and the useful aperture of the components). The peak intensity at the focus is of the order of $900\,\mathrm{GW\,cm^{-2}}$. The resulting STHG signal is then collimated with an aluminum-coated concave spherical mirror with the same focal length as the focusing mirror. Spherical mirrors were used instead of lenses to reduce chromatic aberration. Note that high-quality, low scatter off-axis parabolic mirrors could have been used instead. We opted for spherical mirrors at a relatively low incidence angle due to their better quality focused spot and higher focused intensity compared to standard off-axis parabolas.

The collinear fundamental and STHG beams are sent through a wavelength separator composed of a set of two fused silica prisms, to spatially separate the two beams before the spectral measurement. A double-pass scheme was used to remove spatial chirp (for clarity, only one pass is shown in Fig. 2.1). The spectrum of the STHG signal was then recorded as a function of dispersion with a fiber-coupled spectrometer (Ocean Optics HR4000) to obtain the measured STHG d-scan trace.

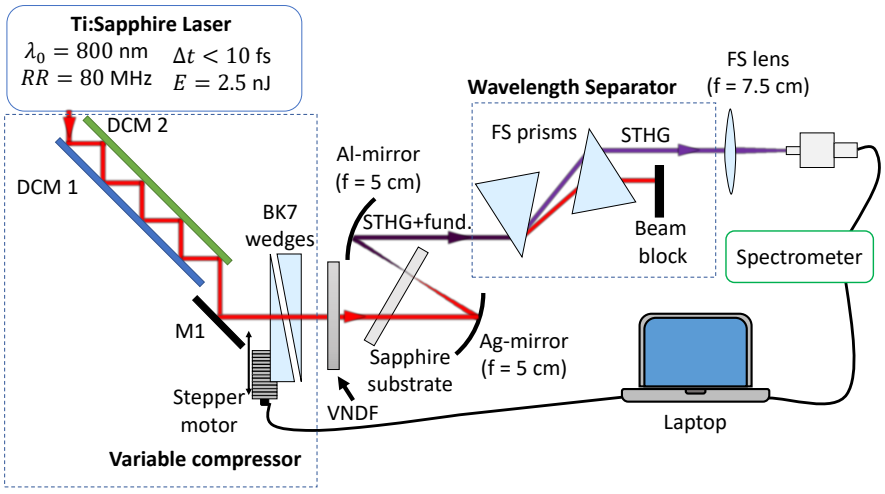


Figure 2.1: STHG d-scan experimental setup. DCM1,2: double-chirped mirrors. M1: mirror. VNDF: variable neutral-density filter. FS: fused silica. Reproduced from [52].

We scanned the dispersion in 150 steps over a 4-mm wedge insertion range for both techniques, using an integration time of 1.5 s for the STHG d-scan and 50 ms for the SHG d-scan.

2.3. Ptychographic retrieval

Since the obtained d-scan traces using STHG have relatively low signal-to-noise ratio (SNR), the retrieval of the electric field of the pulses follows the recently developed ptychographic approach to pulse retrieval from 2D-traces [69–71], which shows promise for retrieving complex pulses from incomplete traces and/or traces with low SNR [69] and which we have adapted in order to extend its applicability to the important case of broadband few-cycle pulses. Ptychographic algorithms have been previously used for image reconstruction in ultrafast electron [72] and X-ray [73] diffraction. It has been extended to phase-only transfer functions [71] and used to retrieve FROG [69], and more recently, d-scan traces [70], even for multi-mode retrievals [74]. This algorithm does not rely on the minimization of an error function (such as the error function G defined previously), but instead iteratively approximates the field by combining the field from a previous iteration with the measured and the calculated d-scan traces via an adequate transfer function.

The ptychographic algorithm starts by applying the phase of the compressor $\phi(\omega)$ to a first guess of the pulse $E_k(\omega)$, where k is the $k-th$ position of the compressor being used:

$$X_k(\omega) = E_k(\omega)e^{i\phi_k(\omega)} \tag{2.1}$$

The algorithm then simulates the nonlinear effect being used, which in the case of SHG is as follows:

$$\psi_k(t) = \left(\mathcal{F}^{-1}\left\{X_k(\omega)\right\}\right)^2 \tag{2.2}$$

and in the case of STHG is:

$$\psi_k(t) = \left(\mathcal{F}^{-1}\left\{X_k(\omega)\right\}\right)^3 \tag{2.3}$$

The corresponding complex spectral amplitude is given by:

$$\Psi_k(\omega) = \mathcal{F}\left\{\psi_k(t)\right\} \tag{2.4}$$

and the simulated d-scan trace, $T_k^{sim}(\omega)$, can be modeled as:

$$T_k^{sim}(\omega) = |\Psi_k(\omega)|^2 \tag{2.5}$$

Following the ptychographic approach, a modulus constraint is applied:

$$\Psi'_k(\omega) = \sqrt{T_k(\omega)}\frac{\Psi_k(\omega)}{|\Psi_k(\omega)|} \tag{2.6}$$

where $T_k(\omega)$ is the normalized measured d-scan trace. A new signal, $\psi'_k(t)$, is then determined by:

$$\psi'_k(t) = \mathcal{F}^{-1}\left\{\Psi'_k(\omega)\right\} \tag{2.7}$$

To obtain the new (iterated) field, a transfer function is computed, which for the second-harmonic reads:

$$X'_k(t) = \frac{1}{2}\left[2X_k(t) + \frac{X_k^*(t)}{|X_k(t)|^2_{max}}\left(\psi'_k(t) - \psi_k(t)\right)\right] \tag{2.8}$$

and for the STHG variant reads:

$$X'_k(t) = \frac{1}{3}\left[3X_k(t) + \frac{(X_k^*(t))^2}{|X_k(t)|^4_{max}}\left(\psi'_k(t) - \psi_k(t)\right)\right] \tag{2.9}$$

where $X_k(t) = \mathcal{F}^{-1}\left\{X_k(\omega)\right\}$. This function is inspired by Newton's method to compute the square root. Going back to the frequency domain, $X'_k(\omega) = \mathcal{F}\left(X'_k(t)\right)$, the phase of the compressor is removed:

$$E'_k(\omega) = X'_k(\omega)e^{-i\phi_k(\omega)} \tag{2.10}$$

Finally, the field is calculated as the arithmetic average of the previous fields over all N dispersion points, i.e.:

$$E(\omega) = \frac{\sum_{k=1}^{N} E'_k(\omega)}{N} \tag{2.11}$$

It is important to note that Equation 2.8 is used to compute the fundamental field from the

SHG field, which is equivalent to taking the square root in the time domain. However, the main problem arises in the ambiguity that it generates, since there are two solutions (two branches in the complex plane) to this computation and, depending on the solution chosen, the retrieval algorithm can stagnate at a local minimum. To solve this problem, the root choice is imposed by the modulus constraint together with the field averaging, and Equation 2.8 preserves the choice [74]. A similar approach is made for the STHG variant.

To test the efficiency of the ptychographic algorithm, we have simulated a d-scan trace from a Gaussian spectrum with a center wavelength of $800\,\text{nm}$, capable of supporting pulses with TL duration of $7\,\text{fs}$, and have applied a spectral phase with TOD equal to $137.6\,\text{fs}^3$. The simulated and retrieved d-scan trace, together with the simulated and retrieved spectral power and phase, can be seen in Figure 2.2. The retrieved d-scan trace, spectral power, and spectral phase are in excellent agreement with their counterparts, with a G error equal to $0.03\,\%$.

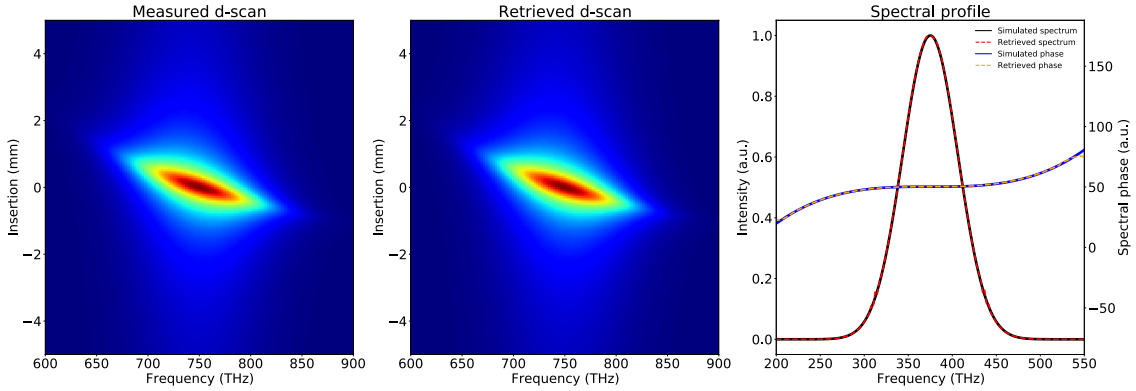


Figure 2.2: Ptychographic retrieval of a pulse with a Gaussian profile (G = $0.03\,\%$).

We have also tested the ptychographic algorithm with d-scan traces with a low signal-to-noise ratio (SNR), by adding an intensity noise matrix that follows a Gaussian distribution to the trace, with an intensity of $40\,\%$ of the trace intensity). The results can be seen in Figure 2.3.

To prove the efficiency of the ptychographic algorithm, we have also retrieved more complex spectral shapes, as can be seen in Figure 2.4. Once again, the retrieved d-scan trace, spectral power, and spectral phase are in excellent agreement with their counterparts, with a G error equal to $0.09\,\%$.

The ptychographic algorithm has only been adapted for d-scan traces very recently [70],

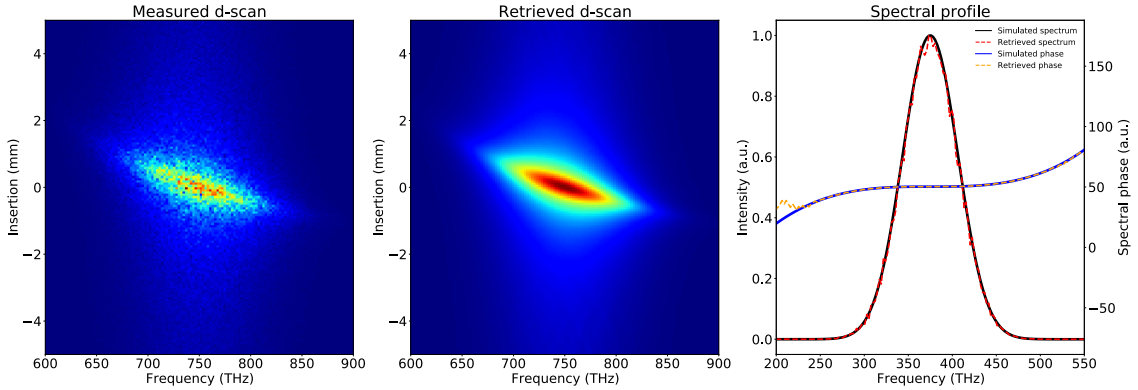


Figure 2.3: Ptychographic retrieval of a pulse with a Gaussian profile, with 40 % Gaussian noise (G = 0.54 %).

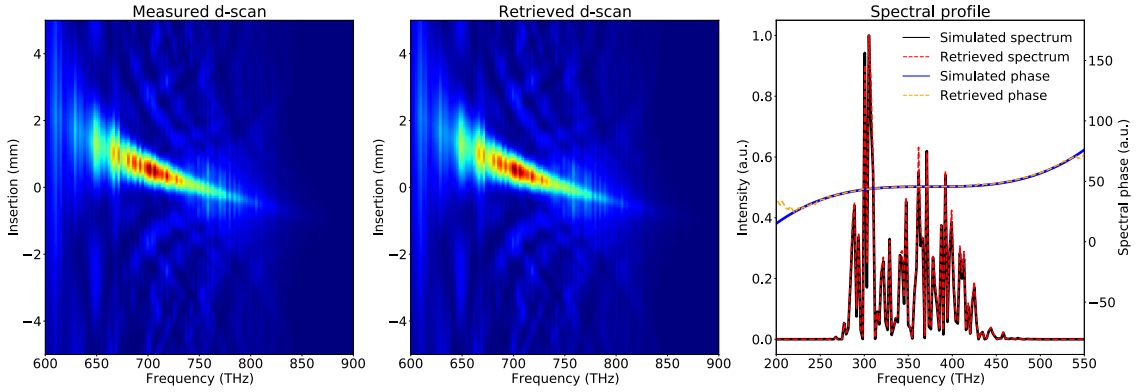


Figure 2.4: Ptychographic retrieval of a pulse with a complex spectral profile (G = 0.09 %).

but was never used with ultrabroadband laser sources. This algorithm successfully retrieved both the spectrum and the phase of relatively long (40 fs) pulses derived from a grating compressor. However, in our case of shorter, few-cycle pulses, with a broadband spectrum, the ptychographic algorithm did not retrieve a spectral power that is in good agreement with the experimental, measured spectrum.

We therefore introduced a new extension to the algorithm (see Fig. 2.5 for a flowchart diagram describing the general aspects of the algorithm) to improve the accuracy of the retrieved spectrum. We observed numerically that a first run of the algorithm (first stage) yields a retrieved spectrum that can be significantly different from the directly measured spectrum, which can be attributed to the fact that the generation of the nonlinear effect is assumed to be ideal. With the retrieved trace and the acquired trace, it is possible to calculate a spectral filter (Equation 1.32), and a new trace can be constructed by factoring out the filter from the measured trace. With this new modified trace, the algorithm is run again (second stage), where the retrieved spectrum is now close to the measured one.

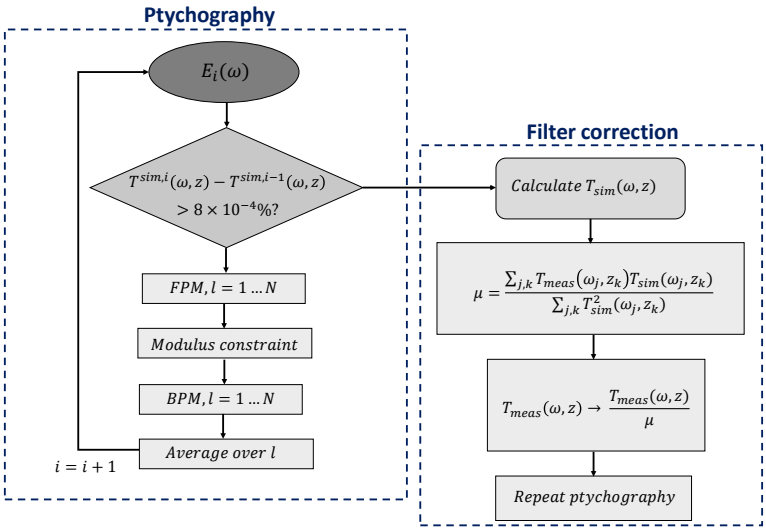


Figure 2.5: Flowchart diagram describing the ptychography algorithm with the filter correction variation. $E_i(\omega)$: guess for the spectral power and phase (i^{th} iteration); $T^{sim,i}(\omega,z)$: simulated d-scan using the guess for the spectral power and phase (i^{th} iteration); FPM: Forward Propagation Model; BPM: Backward Propagation Model; l: position of the compressor; $\mu(\omega)$: response function. Reproduced from [52].

In this work, the algorithm was implemented by Dr. Miguel Canhota, which also developed and implemented the filter correction approach.

2.4. Experimental results

The measured and the retrieved STHG d-scan using a sapphire plate can be seen in Figure 2.6. One should note that all intensity values below 2% of the maximum are set to zero in the plot (shown in white). All traces are 150 $\times$ 384 pixels in size (insertion $\times$ frequency). One individual retrieval process comprises the two stages, including the filter correction treatment, and takes around 4 seconds in the SHG variant and 5 seconds in the STHG variant, using a 2019 AMD Ryzen 7 processor. The stopping criteria for each stage is that the difference between consecutive simulated traces be less than 8×10^{-4} percent. For differences smaller than the one referred, some oscillations appeared in the spectrum, and therefore the stopping criteria was adjusted to overcome this problem. The retrieved d-scan trace shown corresponds to one out of 10 retrievals, performed for different initial guesses (Gaussian spectra with random second- and third-order spectral phases). The retrieved spectral phase and intensity used to reconstruct the pulse's temporal profile are the mean retrieved spectral phase and intensity of all retrievals.

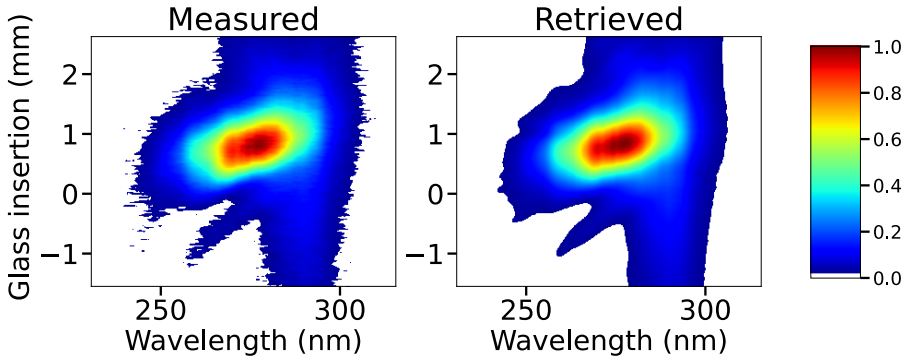


Figure 2.6: Measured (left) and retrieved (right) STHG d-scan using a 0.5 mm-thick sapphire substrate. Reproduced from [52].

The mean d-scan error G is 8.1%, which is relatively high since the retrieval algorithm does not retrieve the noise that appears on the d-scan trace. However, we were able to reconstruct the main features of the STHG d-scan, namely the trace's small tilt, caused by residual third-order dispersion, and the small features that appear around the trace's center of mass.

The same retrieval process was applied to the measured SHG d-scan, whose measured and retrieved traces can be seen in Figure 2.7.

In this case, the mean d-scan error G is $6.5\,\%$, and all the features were correctly reproduced by the retrieval. Visually, both retrieved d-scan traces are very similar to the

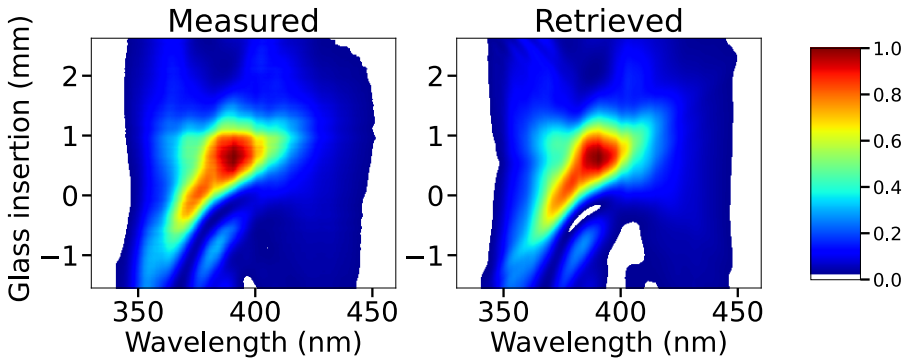


Figure 2.7: Measured (left) and retrieved (right) SHG d-scan using a $20\,\mu$m-thick BBO crystal. Reproduced from [52].

measured ones. The retrieved spectral phases and amplitudes obtained from both techniques are shown in Figure 2.8.

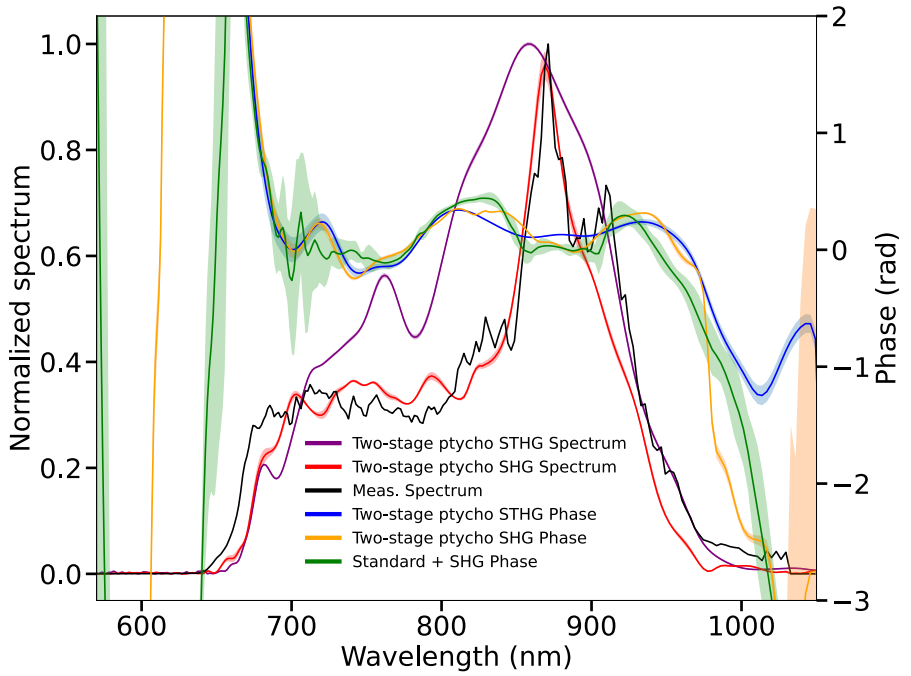


Figure 2.8: Mean retrieved spectral phase and amplitude for SHG d-scan (orange and red, respectively) and STHG d-scan (blue and purple, respectively), along with the calculated standard deviation (shaded area). The black curve is an independent measurement of the spectral power of the laser, and the green curve is an independent spectral phase retrieval for SHG d-scan, using a standard retrieval algorithm. Reproduced from [52].

We see that in the region with higher spectral power the retrieved spectral phases using both techniques are in very good agreement. Both spectral phases diverge rapidly for wavelengths lower than ≈ 680 nm and are also relatively flat over the most significant spectral region ($\approx$ 680-960 nm).

The spectral intensity retrieved using SHG d-scan is in excellent agreement with the measured one. However, the retrieved spectral intensity with the STHG d-scan has significant differences compared to the measured one, which we attribute to the presence of astigmatism induced by the silver-coated concave mirror. This effect was visible as small shifts in the nonlinear signal frequencies that depend on the angle and distance between the laser beam and the sapphire plate. The spectrum retrieved by the STHG d-scan has smoother features than the measured spectrum, which could be attributed to the fact that it is based on a third-order process and is thus less sensitive to the electric field when compared to a second-order process.

For comparison, the retrieved spectral phase for SHG d-scan using a standard retrieval algorithm is shown as well. It is clear that the spectral phase retrieved using the ptychographic algorithm is in excellent agreement with that retrieved by a standard algorithm. The retrieved spectral phase for the STHG d-scan using a standard retrieval algorithm is not shown here, due to the incapability of said algorithm to correctly retrieve the ultrashort pulse, caused by the low signal-to-noise ratio of the measured STHG signal.

The retrieved temporal profile of the ultrashort pulse when using the two measuring techniques is given in Figure 2.9.

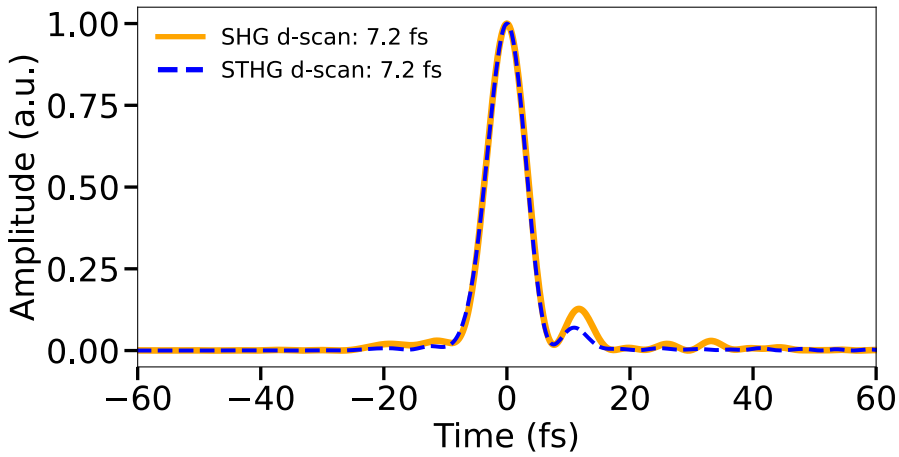


Figure 2.9: Pulse temporal profile retrieved by SHG d-scan (orange) and STHG d-scan (dashed blue), using both the retrieved spectral amplitude and phase. Reproduced from [52].

The agreement between both retrievals is very good, with a full-width-at-half maximum (FWHM) pulse duration of (7.2 ± 0.1) fs (STHG d-scan) and (7.2 ± 0.2) fs (SHG d-scan). If the pulses are plotted using the measured spectrum instead of the retrieved spectra, they are virtually indistinguishable by eye, which again confirms the robustness of the phase retrieval. In both cases, we observe a small post-pulse, a synonym of residual

third-order dispersion, whose position is identical in both cases. These results are also in good agreement with previously published measurements [27] of the same laser source.

2.5. Conclusions and future work

We have demonstrated surface THG d-scan measurements of few-cycle laser pulses using a 0.5 mm-thick sapphire substrate as the nonlinear medium and a ptychographic retrieval algorithm adapted to broadband pulses by introducing a second retrieval step to account for the non-ideal nature of the nonlinearity and fully retrieve the pulses (spectrum and phase) without the need to calibrate the measured nonlinear signal in intensity. These results are in very good agreement with the established technique of SHG d-scan based on BBO crystals, showing that surface THG d-scan is a powerful technique for the simultaneous characterization and compression of ultrashort pulses. Although this filter correction approach was applied to the ptychographic algorithm, it is not exclusive to it, and could be used in other full-field d-scan retrieval algorithms.

The intrinsic broadband nature of STHG should allow the full characterization of ultrashort pulses with arbitrary frequencies and bandwidth via d-scan, only limited by the detection method. For example, using a standard, Si-based spectrometer, STHG signals with wavelength up to $1\,\mu$m can be easily measured, which means that pulses with central wavelengths up to $3\,\mu$m can be characterized using this technique and a standard spectrometer, and therefore characterizing pulses in the mid-infrared (MIR) region is the next step for the STHG d-scan.

3. Highly-sensitive dispersion-scan setup for the characterization of semiconductor mode-locked laser diodes

In this chapter, we will describe the design and development of a highly-sensitive dispersion-scan setup, capable of measuring low-power ultrashort pulses with ps time durations. This setup was implemented to fully compress and characterize pulses from a semiconductor mode-locked laser diode with quantum-dots as the gain medium. Part of this work was published in refs. [75, 76].

3.1. Semiconductor laser diodes

The first semiconductor laser was created in 1962, using GaAs and GaAsP homostructure p-n junctions [77], having continuously improved over the years [78]. However, a new revolution was starting, when the word ”quantum” started to make its way in the ultrashort laser pulse world.

Let us start by defining the de Broglie wavelength λ_B:

$$\lambda_B = \frac{h}{\sqrt{2m^* E}} \tag{3.1}$$

where h is Planck’s constant, m^* is the electron effective mass, and E is the energy. The de Broglie wavelength is in the order of tens of nanometers for III-V compound semiconductors. If one of the dimensions of the active region can be confined to the de Broglie wavelength, the electrons will be confined in one dimension as well [79]. Depending on the number of confined dimensions, we can create quantum wells (1D confinement), quantum wires or quantum dashes (2D confinement), or quantum dots (3D confinement). This will drastically change the density of states, which becomes quantized, as seen in Figure 3.1.

Lasers based on these structures allow higher optical gain per injected carrier, lower temperature dependence, and overall higher power output and efficiency [81]. In the case of quantum dots (QDs), the charge carriers can only occupy a restricted set of levels, being sometimes called ”artificial atoms” due to their resemblance with electrons in an atom.

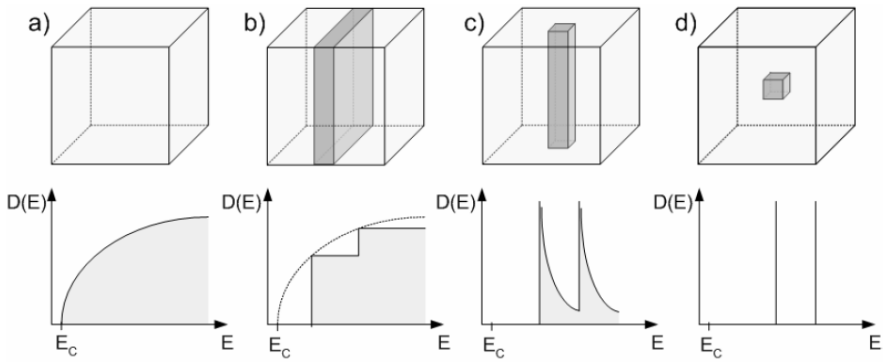


Figure 3.1: Schematic representation and respective density of states of bulk (a), quantum well (b), quantum wire (c), and quantum dot (d) semiconductors [80].

3.2. Mode-locking in semiconductor lasers

Mode-locked semiconductor lasers have proven to be useful tools in ultrafast science, generating short pulses with high repetition rates, depending on the laser structure and mode-locking technique [82]. Mode-locking in semiconductor lasers occurs mainly in three ways: active mode-locking, passive mode-locking, and hybrid mode-locking. For the purpose of this thesis, we will focus our attention on passive mode-locking.

Passive mode-locking can be implemented by introducing a saturable absorber (SA) within the laser, electrically isolated from the gain section, for an independent control of both sections. In a saturable absorber, the loss decreases as the optical intensity increases, which can be a self-starting mechanism for mode-locking. A DC negative voltage (reverse bias) is applied to control the absorption recovery time in the saturable absorber. It can be implemented at the edge of the device, usually called a two-section laser, or in the center of the device - in that case, to enable colliding pulse mode-locking (CPM) [83]. Passive mode-locking also allows for high repetition rates, dictated by the cavity length [84, 85].

When the laser is started, the modes oscillate with random, non-correlated phases, creating noise bursts. However, if one of these bursts is energetic enough, it will bleach the saturable absorber and, at the peak of the burst, the losses will be smaller. At the same time, the low-intensity wings will be attenuated, thus starting the pulse generation process.

The gain and absorption dynamics play a key role in pulse shaping. In a steady state, the unsaturated losses prevail over the gain. However, when the leading edge of the pulse enters the saturable absorber, the losses are saturated at a higher pace than the gain, thus

creating a net gain window that allows for pulse formation (see Figure 3.2). Applying a reverse bias to the saturable absorber leads to a faster sweep-out of the photogenerated carriers, allowing for a faster absorption recovery. Increasing the reverse bias further decreases the absorption recovery time, thus allowing for pulse shortening [86].

It is important to mention that this temporal description of mode-locking is completely related to its description in the frequency domain. The noise bursts described result from an instantaneous phase-locking of several modes, which are favored by the saturable absorber instead of the low-power CW noise.

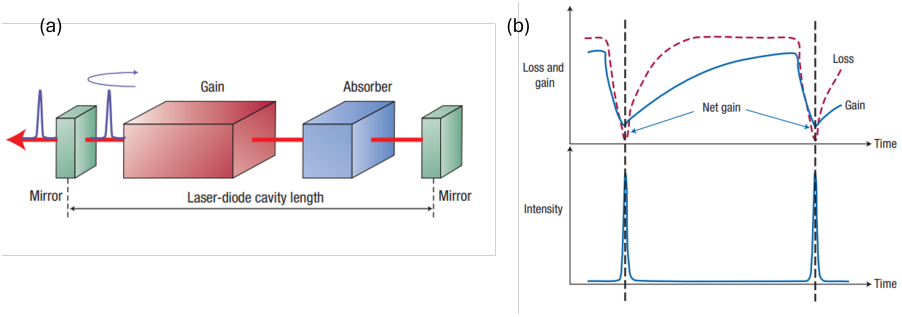


Figure 3.2: (a) Illustration of a two-section passively mode-locked quantum-dot laser. (b) Gain and loss dynamics in a quantum-dot laser with a saturable absorber. Reproduced from [86].

3.3. The advantages of quantum-dots as gain media

There must be a net gain window to generate pulses in semiconductor lasers, which can only be created if the absorption saturates quicker than the gain and the absorption recovers faster than the gain, so that the losses saturate more greatly than the gain. In this case, the saturation energy of the gain section must be higher than the one of the absorption section, or in other words, the stability parameter [82]:

$$S = \frac{E_{sat,g}}{E_{sat,a}}; E_{sat,g} = \frac{h\nu A}{\partial g/\partial N}; E_{sat,a} = \frac{h\nu A}{\partial a/\partial N} \tag{3.2}$$

must be greater than one (where $E_{sat,g}$ is the saturation energy of the gain section and $E_{sat,a}$ is the saturation energy of the absorber, h is the Planck's constant, ν is the optical frequency, and $\partial g/\partial N$ and $\partial a/\partial N$ are the differential gain and loss, respectively).

Let's compare the normalized modal gain in bulk materials, quantum wells, and quantum dots (see Figure 3.3 for more details). Quantum dots are the clear winner since, due to their discrete density of states, the modal gain saturates more strongly with the carrier

density, leading to a lower differential gain and, therefore, a higher stability parameter, making them the ideal candidates for stable mode-locking.

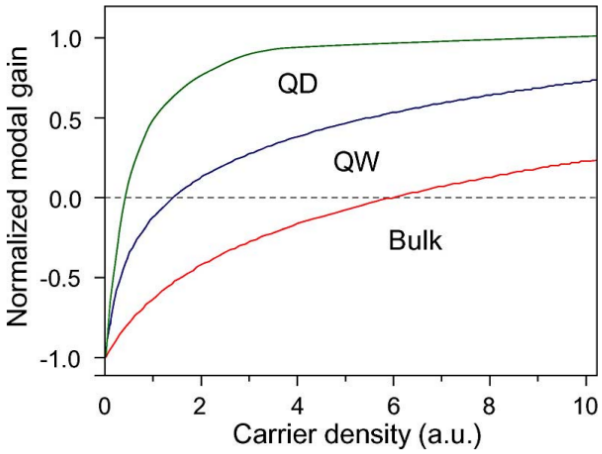


Figure 3.3: Normalized modal gain vs carrier density for bulk, quantum well and quantum dot systems [87].

Quantum dots also offer a broad gain bandwidth, due to the inhomogeneous broadening caused by their size distribution (see Figure 3.4). This broad gain curve should allow the generation of sub-100 fs pulses if the dispersion effects are effectively minimized, and the amplification of broad laser sources, as demonstrated with the amplification of both CW sources [88] and sub-200 fs pulses [89].

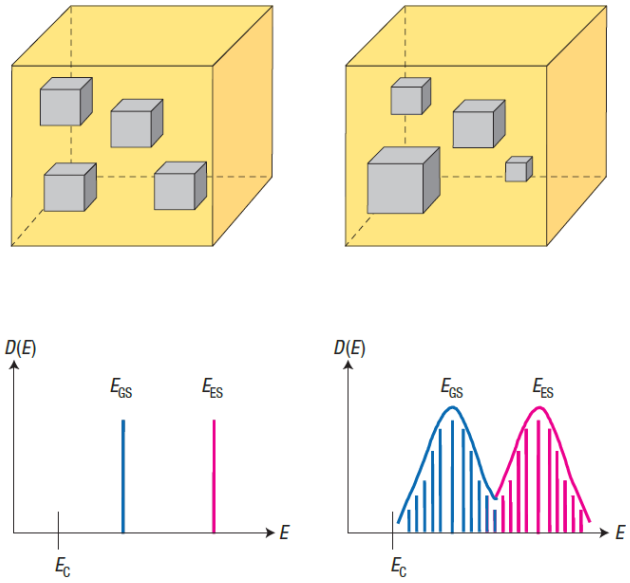


Figure 3.4: Left: ideal QD system, with all the QDs having the same size, and respective density of states $D(E)$. Right: real QD system, with an inhomogeneous broadening depicted in the density of states, caused by the Gaussian size distribution of the quantum dots. Reproduced from [86].

Quantum dot materials also provide ultrafast carrier dynamics, exhibiting ultrafast gain and absorption recovery [90] with sub-ps carrier recovery observed in a quantum dot absorption modulator when a reverse bias is applied [91]. Other properties, such as a low threshold current [92] and low temperature sensitivity [93], make quantum dots as the ideal semiconductor medium for the generation of ultrashort, high-power laser pulses.

3.4. Mode-locked quantum-dot lasers

The first demonstration of a mode-locked quantum dot laser happened in 2001 [84], with a repetition rate of 7.4 GHz and pulse duration of ≈ 17 ps at $1.3\,\mu$m. In 2004, transform-limited 10 ps pulses were obtained at 18 GHz at the same wavelength [94].

The first sub-ps pulses obtained directly from monolithic quantum-dot mode-locked lasers were achieved in 2004 [95], where pulse durations of 390 fs were observed at high values of drive current and reverse bias, with a broad spectrum of 14 nm and output power of 45 mW for mode-locked operation. After this major achievement, other reports of sub-ps pulses were published [96]. The usage of a tapered waveguide to increase the modal area in the gain section and, consequently, increase its saturation energy has also been studied [87, 97]. This technique allowed for reducing pulse broadening due to gain saturation and generating higher power pulses that can saturate the absorber section waveguide (narrower than the gain section waveguide) more effectively, granting access to sub-ps pulses directly from the laser source. It is important to note that, in general, quantum-dot lasers can also be operated in a broad range of temperatures [98, 99]. Especially, Finch *et al.* [100] have operated an InAs quantum dot laser at extremely low temperatures (20 K), which slows the emission of carriers to the wetting layer, allowing for a wider gain spectrum available and for pulses with temporal widths as low as 290 fs. The generation of ultrashort pulses from mode-locked quantum-dot lasers has also been achieved in different wavelength bands, namely at $1.5\,\mu$m [101].

Regarding the achievable repetition rate of the laser, several efforts have been made to increase this value to its maximum. By simply increasing the number of QD layers, shorter cavity lengths were possible and a high repetition rate of 80 GHz was achieved [96]. Other efforts include harmonic mode-locking, where more than two pulses circulate in the cavity (the harmonic dictates the number of pulses). This technique has demonstrated repetition rates up to 240 GHz [102].

3.5. State of the art in low-power, long pulse duration pulse measurements

Semiconductor laser diodes typically generate high repetition rate, low power pulses with a long pulse duration (in the ps domain), leading to very chirped pulses with pJ energies and less than a Watt of peak power. The difficulty of characterizing these laser sources has led to many advances in the field of ultrashort laser pulse characterization. We will present a brief state-of-the-art regarding the characterization of such low-power, long-duration pulses, specifically from semiconductor lasers.

3.5.1 Frequency-Resolved Optical Gating

In 2008, Xin *et al.* [25] developed a highly sensitive FROG device, allowing the first FROG measurements of quantum-dot mode-locked lasers. The authors successfully characterized $5.0 - 6.3$ ps pulses obtained from a 5 GHz repetition rate, 4.3 nm bandwidth optimized six-stack dots-in-a-well (DWELL) laser structure, grown in a GaAs substrate. Regarding the FROG setup, the SHG signal was generated using a 1 mm-thick lithium iodate ($LiIO_3$) crystal, which was then coupled into a monochromator with a photomultiplier tube (PMT). In 2009, the characterization of 40 GHz, 1526 nm quantum dash lasers was achieved [103], using a standard FROG setup. However, an Erbium-doped fiber amplifier (EDFA) was used to increase the optical power of the laser. In the next year, Schmeckebier *et al.* [104] used SHG-FROG to characterize pulses from an AlGaAs/GaAs-based quantum-dot monolithic mode-locked laser, with a central wavelength of $1.31\ \mu$m and a repetition rate of 40 GHz. Their setup comprised a highly-sensitive SHG detection method, consisting of a monochromator, together with an extremely sensitive charge-coupled device (CCD), achieving low noise detection for pulses with energy down to 9 fJ and a peak power of 3.5 mW.

Li *et al.* [23] have also characterized, in 2013, pulses from a InAs/InGaAs quantum-dot monolithic mode-locked laser, with central wavelength of 1241 nm and bandwidths of $2 - 3$ nm, resulting in pulses with FWHM of a few picoseconds, using SHG-FROG. An aperiodically-poled $LiNO_3$ (a-PPLN) waveguided crystal with a 45.4 mm long poling region was used as the SHG medium. Apodization was used to flatten the bandwidth of the poled grating waveguide over 20 nm. Two $40\times$ objectives were used to couple the light into and out of the waveguide. The second-harmonic signal was then coupled to a highly-sensitive Ocean Optics QE65000 spectrometer, allowing near real-time acquisition.

3.5.2 Frequency-Resolved Mach-Zender Gating

An interesting variation of the FROG technique is the Frequency-Resolved Mach-Zender Gating (FRMZG), which uses the same principle as frequency-resolved electro-absorption gating [105], but with a Mach-Zender modulator as a gate, with the advantage of being a linear technique capable of measuring extremely low power pulses. This technique has been implemented by Habruseva *et al.* [106], to successfully characterize an optically injected, 10 GHz, 1295 nm QD laser.

3.5.3 Stepped heterodyne detection

With the advantage of being a linear, self-referenced method, the stepped heterodyne detection [107] is another option for the characterization of low-power ultrashort laser pulses. In this technique, the to-be-characterized pulse is mixed with an optical local oscillator positioned between two optical modes. The interference between the oscillator and the adjacent modes (which is measured in a real-time oscilloscope), allows measuring both the amplitude of the modes and the phase between them.

In 2011, Murdoch *et al.* [108] presented a variation of this method, where they introduced an electronic oscillator to the setup, which improves the setup's capability of measuring pulses with extremely high repetition rates (up to 100 GHz), and used this setup to measure 40 GHz pulses from a quantum-dash mode-locked laser.

3.5.4 Sonogram

The sonogram technique was used by Stolarz *et al.* [109] to characterize pulses from a 35 GHz, $1.5\,\mu$m semiconductor mode-locked laser. This technique relies on cross-correlating a spectrally filtered pulse with a replica of the pulse on a quasi-instantaneous detector (for example, a two-photon absorption detector), creating a sonogram trace that is a time-frequency representation of the pulse and measures the group delay of each frequency component [110] *, allowing the complete characterization of ultrashort pulses while being free from the time-direction ambiguity from which FROG suffers. It has clear advantages over standard pulse diagnostic methods, such as a broad detection bandwidth with low polarization sensitivity [111] and the lack of need for phase-matching [112], providing a simple measurement procedure due to the direct conversion of an optical signal into a photocurrent. Using a photomultiplier tube (PMT) as the two-photon absorption

*It can be seen as a FROG measurement in the time domain, where the spectral filtering precedes the temporal gating

detector allows measuring pulses with energies as low as $10\,\mathrm{fJ}$ and peak powers of $5\,\mathrm{mW}$ [109].

3.5.5 Shifted Wave Interference Fourier Transform Spectroscopy

Shifted Wave Interference Fourier Transform Spectroscopy, or SWIFTS, for short, is a linear technique that allows measuring the phase coherence of a comb spectrum, by using intermode beat spectroscopy to measure the degree of coherence [113, 114]. Also, the complex part of the SWIFTS spectrum equals the phase difference between two adjacent modes, allowing the extraction of the time-dependent intensity and time-dependent frequency. This technique has been used to study injection-locked quantum-cascade laser frequency combs [115], regarding phase coherence and temporal profile.

3.6. The advantages of dispersion-scan

The previously introduced techniques have been successfully implemented to characterize pulses with low power and long durations, such as those from semiconductor laser diodes. However, d-scan has some clear advantages compared to the referred techniques. First, it is a fully inline and easy to implement setup, without the need for beam splitting. Second, a single d-scan trace provides information about the spectral power and phase of the pulses (such as the other techniques), but also allows for the simultaneous compression of the measured pulses, due to the existence of a compressor built into the d-scan setup. Third, the d-scan technique has the possibility to retrieve the compressed pulses in all the N_z points of compression with a single d-scan trace, which has a N_z-fold advantage in terms of the number of measurements needed compared to the referred techniques. And fourth, it allows us to gain further information regarding pulse train instabilities, which will prove useful in the next chapters. With this information, we have decided to build a d-scan setup that is modified to accommodate for the low power and long duration nature of the studied laser sources.

3.7. Used quantum-dot laser

The QD laser used in these experiments is a two-section QD laser, with an active region composed of multiple layers of InAs/GaAs QDs, grown and fabricated by Innolume (GmbH). The total laser length is 8 mm, with a saturable absorber to total length ratio of 11%, similar to the laser used in [116]. The distributed saturable absorber consists of 3 sections with 0.3 mm each, located near the back-facet of the laser and interspersed

between 0.7 mm gain sections. The gain and absorption sections are electrically isolated from each other. A schematic of the QD laser can be seen in Figure 3.5.

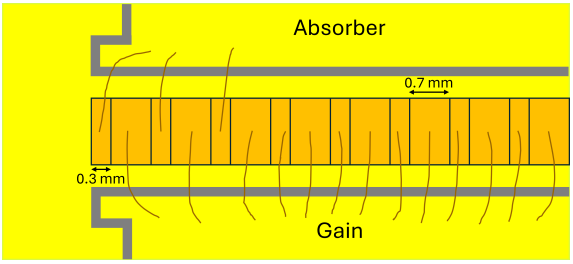


Figure 3.5: Schematic representation of the QD laser used in these experiments, with a distributed saturable absorber.

The back/front facets of the laser were coated with high-reflectivity/low-reflectivity coatings, respectively. The device was kept at a constant temperature of 20 ºC via a feedback-controlled Peltier cooler. The laser is passively mode-locked by applying a forward drive current to the gain section (I_{gain}), while applying a reverse bias voltage (V_{abs}) to the saturable absorber. As a result, a train of pulses with a typical pulse repetition rate of around 5 GHz is obtained. The used QD laser can be seen in Figure 3.6.

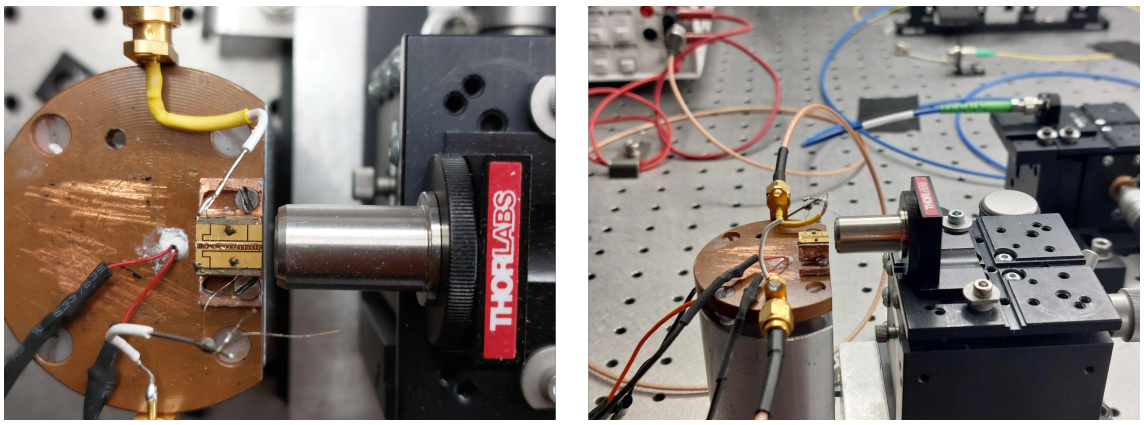


Figure 3.6: QD laser used throughout the experiments.

3.8. Setup design

The first implementations of the d-scan technique used chirped mirrors [27], to introduce negative dispersion and glass wedges, to introduce fine-tuned amounts of positive dispersion. The nonlinear signal generation and measurement consisted of a BBO crystal, for SHG, and a standard spectrometer, to frequency-resolve the nonlinear signal. However, due to the long-duration and low-power nature of mode-locked laser diodes, the setup needs to be changed, to accommodate for these conditions, as will be explained in the following sections.

A schematic of the full setup* can be seen in Figure 3.7. The laser output is launched into a highly-sensitive d-scan setup through an optical isolator with $\sim$ 60 dB isolation, to mitigate accidental retroreflections, which could de-stabilize the laser, thereby ensuring that any instabilities observed are intrinsic to the laser. The main d-scan setup is divided into three main sections: pulse compression (section S1), nonlinear signal generation (section S2), and nonlinear signal detection (section S3). Each of these sections will be described in the next sections. To search for mode-locking regimes, we have also fiber-coupled the laser beam to a 29 GHz photodetector (Picometrix D-15), connected to a 26.5 GHz electrical spectrum analyzer (Agilent E4407B), to measure the RF spectrum. For each d-scan measurement, an independent measurement of the fundamental spectrum is made, using an optical spectrum analyzer (OSA, Anritsu MS9710C).

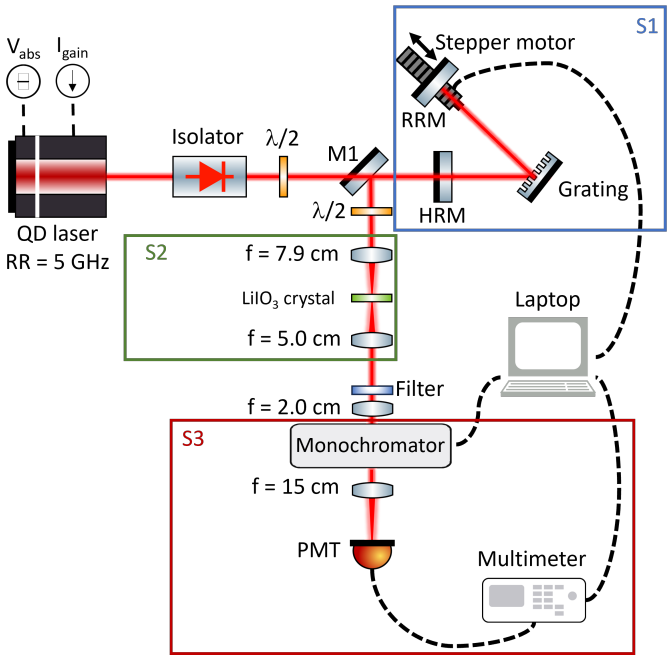


Figure 3.7: Experimental setup. Blue section (S1): compressor system, based on a single-grating four-pass configuration. Green section (S2): nonlinear signal generation. Red section (S3): Nonlinear signal frequency-resolved detection. RR: repetition rate. $\lambda/2$: half-wave plate. M1: mirror. HRM: hollow-roof mirror. RRM: retroreflector mirror. PMT: photomultiplier tube. Since the incoming and outgoing beams of the compressor have different heights, the mirror M1 is only aligned for the outgoing beam. For the first and second pass on the grating, the hollow-roof mirror is at a different height, to allow light to enter the compressor. Adapted from [75, 76].

The setup is remotely controlled by a USB connection, using a LabView ™program designed and implemented specifically for this project. The experimental setup can be seen in Figure 3.8 and Figure 3.9.

*Optical components drawn using: ComponentLibrary by Alexander Franzen, licensed under a Creative Commons Attribution-NonCommercial 3.0 Unported License.

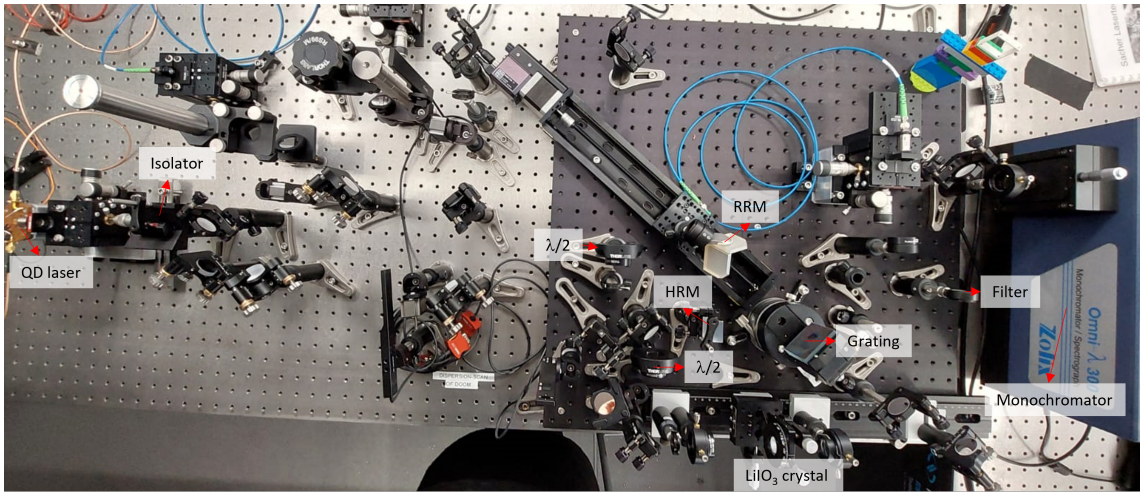


Figure 3.8: Experimental d-scan setup, top perspective.

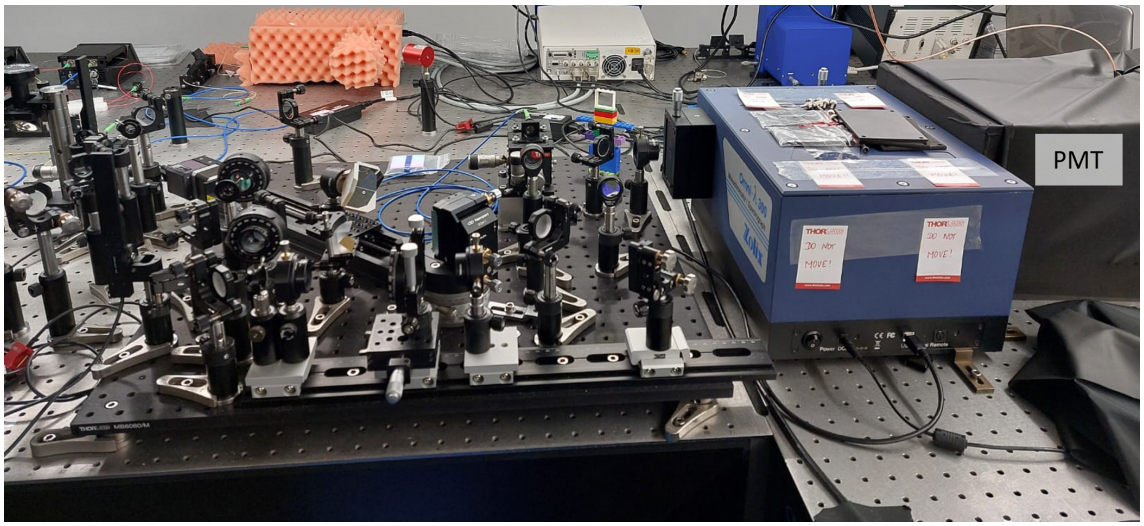


Figure 3.9: Experimental d-scan setup, side perspective. The black box is needed to reduce stray light captured by the photomultiplier tube.

3.8.1 Pulse compression

Due to the highly chirped nature and low spectral bandwidth of the pulses generated in these laser sources, a compressor that can introduce a Group Delay Dispersion in the order of a few ps^2 is needed. This problem is solved by using a grating compressor, which allows introducing dispersion in this order of magnitude. The compressor used in this setup is a single-grating compressor [34, 117], which is a variation of the standard grating compressor. In this variation, one of the gratings is replaced with a retroreflector mirror, as shown in Figure 3.10.

In this compressor, the distance between the retroreflector mirror and the grating dictates the amount of dispersion applied to the pulse train, whereas the angle of incidence of the grating tunes the wavelength for compression. The single-grating variant allows for pulse

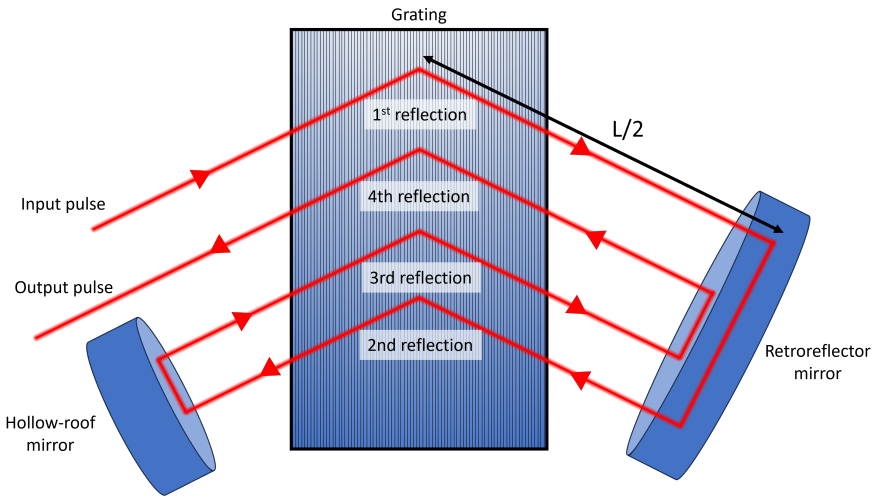


Figure 3.10: Single-grating compressor implementation.

compression without the need for complex alignments, and with minimization of angular dispersion, pulse-front tilt, and spatial chirp [34]. The GVD introduced by the compressor is given by [118]:

$$GVD(\lambda) = -\frac{\lambda^3}{\pi c^2 d^2}\left[1-\left(\frac{\lambda}{d}-sin\vartheta_0\right)^2\right]^{-\frac{3}{2}} \tag{3.3}$$

where λ is the wavelength, c is the speed of light, d^{-1} is the groove density and ϑ_0 is the angle of incidence. The total GDD introduced by the compressor at a specific wavelength is given by multiplying the GVD by L, which is double the distance between the grating and the retroreflector mirror. The TOD introduced by the compressor is given by [118]:

$$TOD(\lambda) = -\frac{3\lambda}{2\pi c}\frac{1+\frac{\lambda}{d}sin\vartheta_0 - sin^2\vartheta_0}{1-\left(\frac{\lambda}{d}-sin\vartheta_0\right)^2}GDD(\lambda) \tag{3.4}$$

The phase introduced by the compressor can be approximated by the Taylor series:

$$\varphi(\omega) = \frac{1}{2}GDD(\omega_0)(\omega-\omega_0)^2 + \frac{1}{6}TOD(\omega_0)(\omega-\omega_0)^3 \tag{3.5}$$

where ω is the angular frequency and $\omega_0 = 2\pi c/\lambda_0$ is the central angular frequency, which is defined for the Taylor expansion.

Since the chirp of the pulses changes significantly with driving conditions, two different gratings had to be used to accommodate the range of dispersion needed: one with 600 lines/mm and a blaze wavelength of 1.25 μm (Thorlabs GR50-0613), with an angle of

incidence of $45°$ yielding a GVD value of -2.59 ps^2/m@1265 nm and a TOD/L value of $0.00543\,\text{ps}^3/\text{m}$, and one with 830 lines/mm and a blaze wavelength of 1.2 μm (Laser-Components HR-R-R-830/1200-F-50X50X9.5), with an angle of incidence of $55°$ yielding a GVD value of -5.36 ps^2/m@1265 nm and a TOD/L value of $0.0136\,\text{ps}^3/\text{m}$. Due to the different angles of incidence, for the first grating, the total distance range L is approximately $0.478\,\text{m}$, yielding a GDD range of $-1.243\,\text{ps}^2$ (from -0.267 to $-1.51\,\text{ps}^2$) and a TOD range of $0.00244\,\text{ps}^3$ (from 0.00559 to $0.00315\,\text{ps}^3$), and for the second grating, the total distance range is approximately $0.466\,\text{m}$, yielding a GDD range of $-2.494\,\text{ps}^2$ (from -0.536 to $-3.03\,\text{ps}^2$) and a TOD range of $0.00632\,\text{ps}^3$ (from 0.00136 to $0.00768\,\text{ps}^3$). The maximum and minimum distances are limited by the linear motorized stage used and the setup geometry since the motorized stage crosses the path of the beam going from the QD laser to the compressor, which reduces the total length that can be used in the stage without blocking the incoming beam.

To test the efficiency of the single-grating compressor, we have applied it to the QD laser studied in this thesis. We have used the grating with 600 lines/mm and a blaze wavelength of $1.25\,\mu m$. The used corner cube consisted of a hollow retroreflector mirror (Thorlabs HRR203-P01), which is coupled to a 100-mm high-precision motorized linear motor (Zaber X-LSM100A-KX13AG), to change the distance to the grating. We should note that, for the second part of the experiment, due to the high chirp of the studied pulses, a high range of applied dispersion is needed to measure a full d-scan trace without cropping the signal, so we changed the motor to a Zaber X-LSQ300B-KX13CG, which allows for a 300-mm displacement. The roof mirror was a gold-coated, hollow-roof mirror (Thorlabs HRS1015-M03). The beam undergoes 4 reflections in the grating, due to the reflections on the retroreflector mirror and the hollow-roof mirror. To maximize the output power of the compressor, a half-wave plate is introduced beforehand, enabling to match the polarization direction to that of maximum efficiency in the diffraction grating.

After the single-grating compressor, we fiber-coupled the laser beam to a commercial autocorrelator (A.P.E. PulseCheck NX) and measured the autocorrelation traces of the pulses. We have assumed a $sech^2$ pulse shape, whose autocorrelation trace is well known, and automatically fitted by the autocorrelator software, providing a value for the FWHM.

We have calculated the FWHM of the obtained pulses for different distances between the grating and the retroreflector mirror (which dictates the amount of dispersion introduced to the pulses). An example of three autocorrelations obtained for a driving current of 230

mA and reverse bias voltage of 5.8 V, for three different grating distances, can be seen in Figure 3.11.

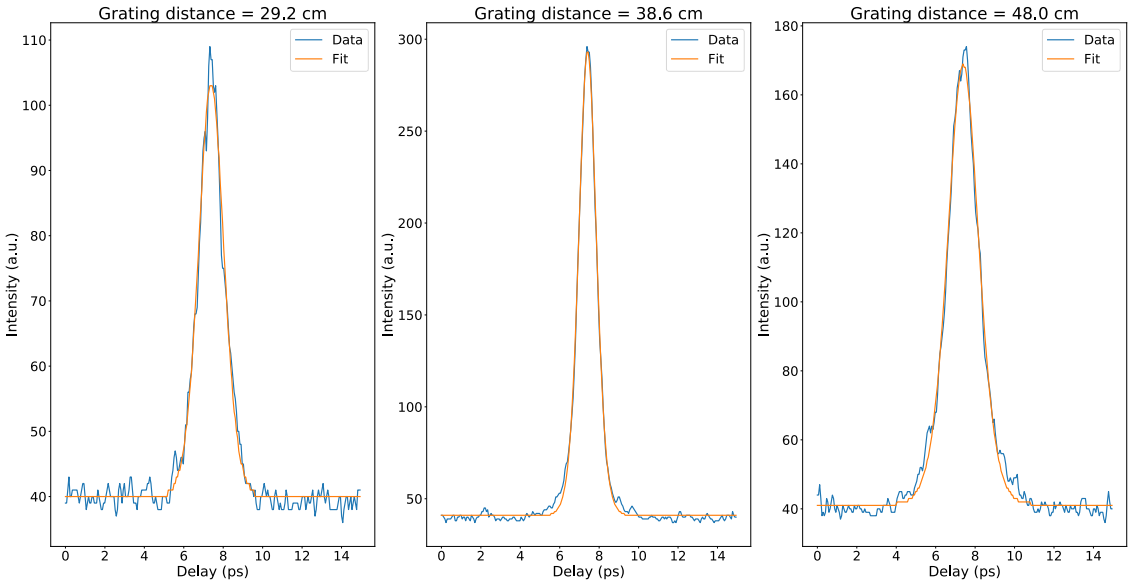


Figure 3.11: Autocorrelation traces (blue curve) and autocorrelation fit assuming a $sech^2$ pulse (orange curve) for pulses obtained at a driving current of 230 mA and a reverse bias voltage of 5.8 V, for distances between the grating and the retroreflector mirror of 29.2 cm, 38.6 cm, and 48 cm.

It is clear that the pulse duration changes if we change the distance between the grating and the retroreflector mirror. If we measure the evolution of the FWHM with the grating distance for different driving conditions, we get the results presented in Figure 3.12.

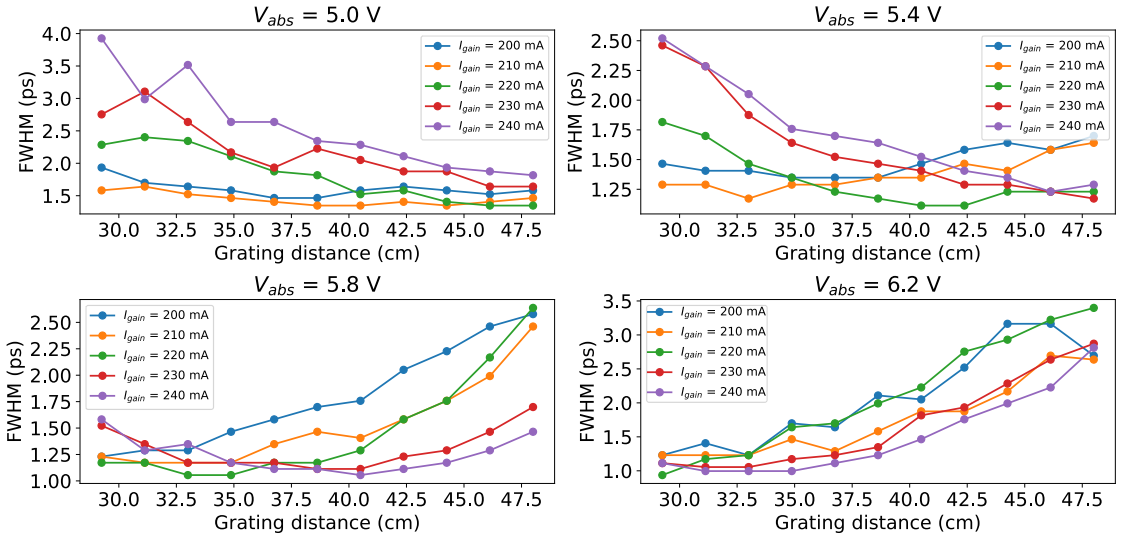


Figure 3.12: Evolution of the FWHM of the pulses obtained after the single-grating compressor for different distances between the grating and the retroreflector mirror. Measurements were made for different laser driving conditions. The lines shown are just guides for the eyes.

We can see that the FWHM of the pulses changes with the distance between the grating and the retroreflector mirror, which is a clear sign that the single-grating compressor is working as intended. If we consider, for example, the data obtained for a driving current of 230 mA and a reverse bias voltage of 5.8 V (red curve of the bottom left graphic of Figure 3.12), we can see that there is a point where the pulse duration is as low as possible for these conditions, meaning that we were able to obtain the shortest pulse duration obtainable with the used compressor. We can also conclude that the grating distance for which the pulses are optimally compressed, which is fully related to the chirp of the pulses, depends on the driving conditions of the QD laser. The chirp increases with the driving current but decreases with the reverse bias voltage applied to the laser. These preliminary results show that the single-grating compressor works as intended, and we can now proceed to the nonlinear signal generation and detection section.

An important feature that needs to be analyzed is the grating compressor efficiency regarding output power. Since the grating has reflection losses, and the beam undergoes 4 passes on the grating, the power losses will be relatively high. For the 600 lines/mm grating, the output power efficiency was calculated to be approximately 27% from the whole compressor setup, while for the 830 lines/mm grating, this value is increased to around 40%. Although these values are relatively low, they can easily be optimized using bespoke gratings with even higher efficiency at the wavelengths of interest.

3.8.2 Nonlinear signal generation

A solid choice for the nonlinear crystal that can provide a high conversion efficiency would be a fiber-coupled waveguided a-PPLN, but the extremely high price of this component is a disadvantage. Also, waveguided a-PPLN is not flexible, since changing the fundamental wavelength would mean that it would be necessary to change the grating period as well, which would drastically increase the cost of the setup. We have chosen to use a lithium iodate ($LiIO_3$) crystal, having good SHG efficiency for the wavelengths of interest. The laser beam is focused on a $LiIO_3$ crystal, generating a second-harmonic signal. The initial measurements were made with a 5-mm thick crystal, with an acceptance bandwidth of $5-6$ nm@1262 nm which was later changed to a 1-mm thick crystal with an acceptance bandwidth of $25-30$ nm@1262 nm to ensure that the acceptance bandwidth was not a limiting factor, with the trade-off of having a lower second harmonic signal. It is important to note that the d-scan measurements did not change when exchanging the crystals, which means that this change did not affect our results.

Both crystals were cut with a cut angle of $25.3°$, to maximize the phase-matching conditions for type I SHG, and have anti-reflective (AR) coating at $1262 + 631$ nm. Another half-wave plate is used before the nonlinear crystal to match the polarization of the laser beam to that of the crystal, to maximize the nonlinear signal intensity. By using a highly-sensitive power meter (Thorlabs S130C), we were able to detect the second harmonic signal and maximize it by adjusting the tilt/tip of the crystal positioning mount, maximizing the phase-matching conditions for SHG. The total integrated SHG power obtainable was a few nW.

3.8.3 Nonlinear signal detection

Due to the low SHG power obtained, frequency-resolving and detecting this signal proved to be a demanding task. The obtainable SHG power is not sufficient to be frequency-resolved and measured in a typical spectrometer, and the process of fiber-coupling the signal to an optical spectrum analyser introduces losses that compound the problem. Therefore, in the nonlinear signal detection, a monochromator was used in conjunction with a PMT. The fundamental signal is blocked by a high-quality, high-pass frequency filter (Thorlabs FESH0800), and the second-harmonic signal is then steered and focused, using a 2 cm focal length lens, into a monochromator (Zolix Omni λ-300), which frequency-resolves the nonlinear signal with a wavelength resolution up to 0.1 nm. It is important to note that light should be focused into the monochromator at a specific focal length, dictated by the monochromator itself. A lower focal length would create losses because a portion of the collimated light misses the grating inside the monochromator, and a higher focal length creates losses as well, because the image of the radiating element on the slit is larger than required, creating system efficiency losses. Therefore, the focal length used was chosen to minimize coupling losses.

This signal is then focused, using a 15-cm focal length lens (Thorlabs LA1433-ML) onto a highly-sensitive GaAsP photomultiplier tube (Thorlabs PMT2101/M), with an estimated radiant sensitivity of approximately 160 mA/W@630 nm. This PMT features an integrated transimpendance amplifier, which converts the output current from the PMT to a voltage with further amplification, yielding a signal that is equal to:

$$V = TG \times S \times G \times P \tag{3.6}$$

where V is the output voltage from the transimpendance amplifier, TG is the transimpendance gain, S is the radiant sensitivity, G is the gain of the PMT and P is the input optical power. The PMT is coupled to a highly-sensitive multimeter (Keithley DMM6500), which allows frequency-resolving the nonlinear signal and measuring the resultant ultralow power signal with a high resolution.

As an example, let us assume an input optical power of $1\,\text{nW}$, which is in the order of magnitude of the average integrated SHG power obtained in our measurements prior to the monochromator. If we assume a nonlinear SHG signal with approximately $2\,\text{nm}$ of spectral bandwidth and using a monochromator resolution of $0.1\,\text{nm}$, the integrated SHG power would be frequency-resolved in 200 slices with optical powers in the order of magnitude of $5\,\text{pW}$. Assuming a radiant sensitivity as defined before, a transimpendance amplifier gain of $11000\,\text{V/A}$ and an estimated PMT gain of 10^6, we would get a voltage signal in the order of $10\,\text{mV}$, which is completely measurable using a highly-sensitive multimeter. We should note that the saturation voltage of the PMT is $1.5\,\text{V}$. With this in mind, we can assume that the signal is strong enough to be frequency-resolved using the monochromator.

For each position of the Zaber motor, we scan the wavelength of the monochromator, to get a frequency-resolved measurement of the nonlinear signal, giving rise to a 2D d-scan trace measurement.

3.8.4 Monochromator calibration

We have tested this setup by measuring a d-scan trace of pulses obtained at different values of drive current and reverse bias voltage. However, we quickly noticed that the monochromator was not calibrated, since the retrieved fundamental spectrum has the same shape but was frequency-shifted compared to the measured one. To calibrate the monochromator, we did not change anything in its mechanical components, but instead applied a post-processing calibration function to the measured wavelengths. In this case, we have used a broadband calibration light source (Thorlabs CSL1), which contained very defined peaks in the region of interest (wavelengths corresponding to the second-harmonic signal of the fundamental spectrum of the QD laser). We have then measured the monochromator wavelengths where the peaks appeared and, by plotting them against the actual peak wavelengths (see Figure 3.13), we have obtained a calibration curve that can be applied to the measured data.

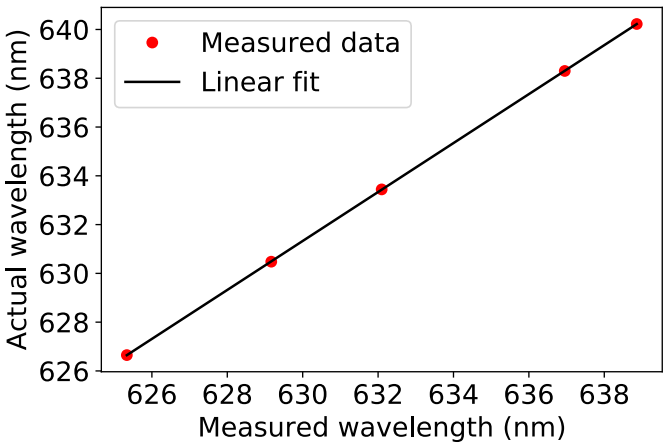


Figure 3.13: Monochromator calibration curve. The linear fit will be used as a post-processing calibration curve for the measured wavelengths in the monochromator.

The calibration curve is given by:

$$\lambda_{actual} = 1.004\lambda_{MC} - 1.006 \tag{3.7}$$

where λ_{MC} is the wavelength measured in the monochromator (in nm), and λ_{actual} is the actual, corrected wavelength (in nm).

3.9. D-scan measurement and retrieval

To test the d-scan experimental setup, we have measured a d-scan trace for pulses obtained at $I_{gain} = 230$ mA and $V_{abs} = 5.4$ V. We performed a d-scan measurement, obtaining a 50 $\times$ 70 matrix (50 dispersion points $\times$ 70 wavelength points). For all measurements, we perform a background signal trace measurement, to subtract from the measured d-scan trace. We have interpolated the wavelengths into a frequency array, obtaining a 50 $\times$ 104 matrix (50 dispersion points $\times$ 104 frequency points). For this measurement, in the single-grating compressor, we have used the grating with 600 lines/mm and a blaze wavelength of $1.25\,\mu m$. Due to the low-power nature of the measured pulses, the obtained d-scan trace suffers from a non-negligible noise. Therefore, a good choice for the retrieval algorithm is the ptychographic algorithm, which can successfully retrieve pulses from low SNR traces. Since the bandwidth of the measured optical spectrum is relatively narrow, the filter correction introduced in the previous chapter is unnecessary, and a simple ptychographic retrieval can be implemented. We have performed a set of 10 retrievals and calculated the retrieved spectral power and phase as the average of the individually retrieved spectral power and phase in each retrieval process. The measured and retrieved

d-scan trace and the retrieved optical pulse in the frequency and time domain can be seen in Figure 3.14.

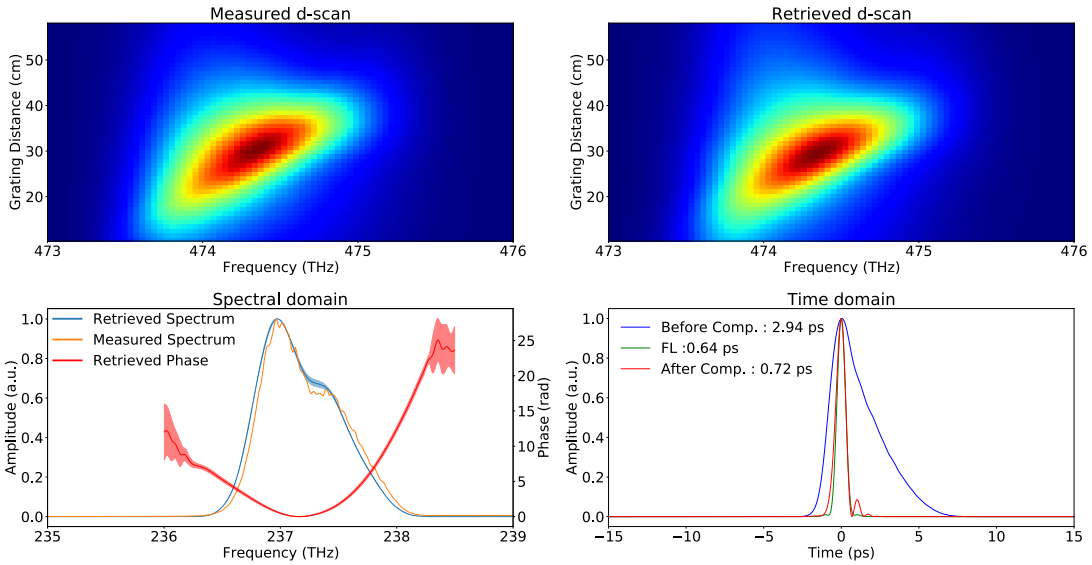


Figure 3.14: Measured (top left) and retrieved (top right) d-scan traces for pulses obtained at $I_{gain} = 230\,\text{mA}$ and $V_{abs} = 5.4\,\text{V}$. Retrieved pulse in the frequency (bottom left) and time (bottom right) domain.

In this retrieval process, the measured d-scan trace is divided by the frequency-dependent response function $\mu(\omega)$, to calibrate the trace effectively. This function is calculated as expressed in Equation 1.32. The mean d-scan error G is $6.6\,\%$, a relatively high value that can be explained by the presence of noise in the d-scan trace (the retrieval algorithm does not retrieve the noise present in the trace). Nevertheless, the retrieved d-scan trace, as well as the retrieved spectral power, are in excellent agreement with their measured counterparts.

Regarding the spectral phase, there is a strong second-order dispersion, which causes a strong temporal broadening as visualized in the temporal domain. The obtained, uncompressed pulse is asymmetric, which will be explained in the next chapter. Regarding the compressibility efficiency of the compressor, we see that the compressed pulse is in the sub-ps regime, and the compressed pulse duration is close to the transform-limit pulse duration, which proves the efficiency of the used single-grating compressor.

3.9.1 Pulse measurement across the dispersion range

One of the advantages of d-scan is the possibility of characterizing not only the uncompressed pulse but also all the pulses obtained at different values of introduced dispersion.

This allows obtaining (and characterizing) different pulse shapes at the output of the compressor according to the dispersion applied to the pulse itself. As an example, we present the pulse shape evolution for the pulses obtained at $I_{gain} = 230\,\text{mA}$ and $V_{abs} = 5.4\,\text{V}$ with the distance between the grating and the retroreflector mirror in Figure 3.15.

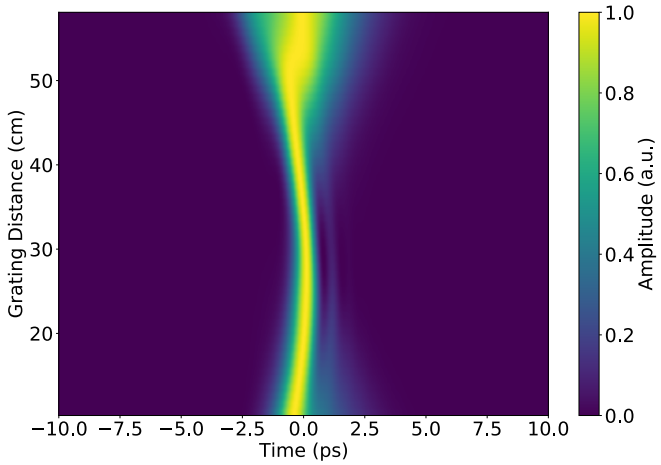


Figure 3.15: Evolution of the temporal profile of the retrieved pulse with the dispersion applied to the pulse driven at $I_{gain} = 230\,\text{mA}$ and $V_{abs} = 5.4\,\text{V}$. The grating with 600 lines/mm and a blaze wavelength of $1.25\,\mu m$ was used in the single-grating compressor.

At low values of applied dispersion, the pulse is asymmetric. However, as we increase the dispersion applied to the pulse, the trailing edge narrows, until we reach the minimum pulse duration obtainable with this compressor. In this case, a post-pulse is visible, a synonym of residual third-order dispersion. As we further increase the dispersion applied to the pulse, the pulse broadens again, but with a different shape, where the asymmetry gets reversed.

3.10. Setup performance

With this setup, we have measured pulses with energies from 1.4 to $2.4\,\text{pJ}$, with a dynamic range of approximately two and a half orders of magnitude. Due to the extremely high sensitivity of the nonlinear detection section, we believe that the minimum energy of the measured pulses is only limited by the intensity threshold for detecting a frequency-resolved second harmonic signal on the nonlinear detection section. The nonlinear generation section could be improved by switching the $LiIO_3$ crystal with a bulk a-PPLN, which would offer a higher nonlinear signal.

The trade-off for this extremely high sensitivity is the long acquisition time. The current limitation is the scanning of two directions (wavelengths and dispersion) instead of one direction (dispersion). To increase the acquisition speed of the setup, the use of a nonlinear

optical crystal with higher conversion efficiency, such as bulk or waveguided fiber-coupled a-PPLN, would allow the use of a non-scanning spectrometer to measure the nonlinear signal, which would drastically increase the measurement speed, although drastically increasing the cost of the setup.

Due to remote communication problems with the monochromator, instead of scanning the nonlinear wavelengths for each dispersion point, we have scanned the grating distance for each nonlinear wavelength, the latter being slower than the former. A single d-scan trace measurement, with 50 grating distance steps and 70 wavelength points (giving rise to a 50x70 matrix) takes approximately 10 minutes, a much longer acquisition time compared to the standard d-scan measurement (tens of seconds) for the same size matrix. For this setup configuration, the only speed increase would be to switch the scanning order, i.e., scanning the nonlinear wavelength for each dispersion point, which would increase the measurement speed by less than an order of magnitude.

Regarding the single-grating compressor, the limitations to the amount of dispersion introduced are determined by the parameters of the used gratings and the achievable distance between the grating and the retroreflector mirror. By using a grating with a higher or lower groove density, the achievable dispersion can easily be tuned to the pulse being compressed.

Although the number of dispersion points was set to 50, this number is subject to changes and can be further reduced without degrading the quality of the retrieval. As proof, we present the retrieval of pulses driven at $I_{gain} = 230\,\text{mA}$ and $V_{abs} = 5.6\,\text{V}$, from d-scan traces that we have interpolated from the original measured d-scan trace, to have 20 or 35 dispersion points. The measured and retrieved d-scan traces can be seen in Figure 3.16.

The measured and retrieved d-scan traces are in excellent agreement. If we plot the temporal profile of the retrieved pulses for all the d-scan traces, we get the results from Figure 3.17, showing that the number of dispersion points can be reduced to at least 20 without degradation of the retrieval process, which would halve the acquisition time.

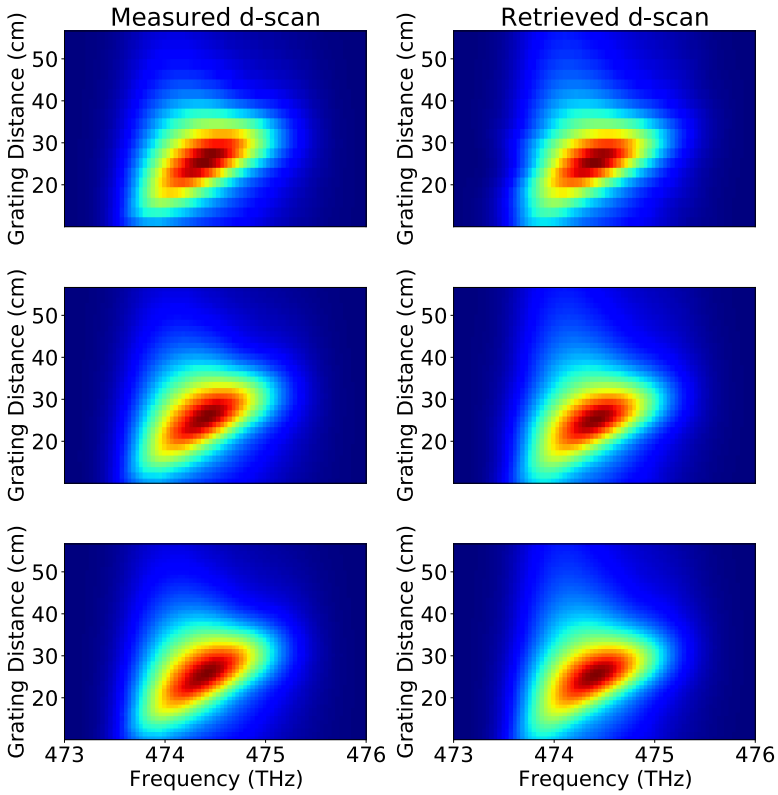


Figure 3.16: Measured (left) and retrieved (right) d-scan traces obtained for the pulses driven at $I_{gain} = 230\,\text{mA}$ and $V_{abs} = 5.6\,\text{V}$, with 20 (top), 35 (middle) and 50 (bottom) dispersion points. The grating with 600 lines/mm and a blaze wavelength of $1.25\,\mu m$ was used in the single-grating compressor.

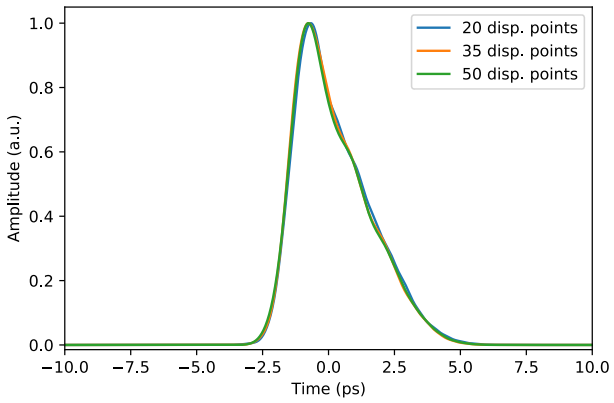


Figure 3.17: Retrieved temporal profiles of the pulses driven at $I_{gain} = 230\,\text{mA}$ and $V_{abs} = 5.6\,\text{V}$, from d-scan traces with 20 (blue), 35 (orange) and 50 (green) dispersion points.

3.11. Conclusions and future work

We have developed a highly-sensitive dispersion-scan setup, based on a single-grating compressor, a standard nonlinear crystal for the second harmonic generation, and a monochromator coupled to a highly-sensitive photomultiplier tube and a multimeter to frequency-resolve the nonlinear signal. The sensitivity acquired with this setup allows the characterization and compression of pulses with ps time duration and pJ pulse energies. The setup has been used to characterize and compress to near the transform-limit ps pulses from a semiconductor laser diode. The minimum energy for the to-be-characterized pulses is only dictated by the sensitivity of the second harmonic frequency-resolved detection section. Using a lock-in amplifier instead of the highly-sensitive multimeter, together with a mechanical chopper installed in the setup, could increase the sensitivity of the setup even further, allowing measuring ultrashort laser pulses with even lower energies.

The acquisition time for a d-scan measurement using this setup and the high loss in the single-grating compressor are the current limitations of the setup. Using bespoke gratings with even higher efficiency at the wavelengths of interest would improve the single-grating compressor regarding output losses.

To improve the acquisition time of a d-scan measurement, a possible solution would be using a bulk a-PPLN crystal for the nonlinear signal generation. These types of crystals use the concept of quasi-phase-matching to provide higher signal generation efficiency and allow for a thicker crystal without the loss of phase-matching. With these crystals, we could achieve a much stronger SHG signal and completely substitute the monochromator (coupled to the PMT and the highly-sensitive multimeter) with a standard spectrometer. With this quality-of-life improvement, the acquisition time of a single d-scan measurement could be drastically improved from a few minutes to a few seconds, which would be up to par with previously developed FROG setups for the characterization of low power, long pulse duration laser sources.

4. Mode-locking dynamics in semiconductor laser diodes

In this chapter, we will describe the use of the developed highly-sensitive d-scan setup to fully compress and characterize pulses from a semiconductor mode-locked laser diode with quantum-dots as the gain medium. With this setup, we have studied the influence of drive current and reverse bias on the pulses' chirp, asymmetry, and time duration, and compressed said pulses to a sub-ps timescale. Part of this work was published in refs. [75, 76].

4.1. Introduction

The compressibility of ultrashort laser pulses from semiconductor laser diodes is an important factor to take into account for the globalization of said laser sources. The pulses from these laser sources are typically up-chirped and need to be compressed to realize their full potential. Several efforts have been made in the past few years, using techniques such as autocorrelation and FROG to measure the uncompressed pulse duration, and then compressing the obtained pulses using either SMF-28 fibers for pulses with central wavelengths around $1.5\,\mu m$ [103, 108, 119, 120] or using grating tunable-compressors [104, 121, 122], allowing for the generation of sub-ps laser pulses from these laser sources. However, different pulse durations may be needed, depending on the application. For each desired pulse duration, a measurement has to be made, to fully characterize each of the desired pulses.

One of the main advantages of the dispersion-scan technique, as concluded in the previous chapter, is the possibility of simultaneously characterizing and compressing an ultrashort laser pulse, using a single d-scan trace measurement. This means that, with a single trace, we can obtain (if the amount of compression obtainable is calibrated for the laser source to be compressed) information regarding the uncompressed laser pulse, compress it to the transform-limit, and also know the pulse shape and temporal duration for all the measured compression points.

Dispersion-scan offers other significant advantages to the field of semiconductor laser diode characterization. Recent numerical simulations [123] predict the existence of a broad trailing edge plateau (TEP) [124] in certain driving conditions, which the authors attributed to non-instant carrier transitions between the carrier reservoir, the excited state,

and the ground state of the QD. These simulations show that pulses with widths at their base that exceed half of the laser cavity round trip time can exist, while still in a stable mode-locking. Experimentally, the authors show the beginning of the formation of a TEP by increasing the drive current. However, for the ultrabroad pulses described before, the autocorrelation trace has non-vanishing wings, and FROG measurements could not reconstruct the pulse properly, particularly due to these non-vanishing wings. However, the measured RF spectra show a strong, defined peak even for these pulses, which suggests a strong mode-locking regime. With d-scan, the situation is different: since d-scan measures a nonlinear signal as a function of the *dispersion* applied to the pulse (and not as a function of a *time delay*), this superimposition between subsequent pulses should not be a problem for a correct and complete pulse characterization using d-scan.

4.2. Dispersion-scan measurements

With the setup fully working, we measured d-scan traces for different values of drive current and reverse bias. The results can be seen in Figure 4.1. For the pulses driven at $V_{abs} = 4.6\,\text{V}$, and for the pulses driven at $I_{gain} = 240\,\text{mA}$ and $V_{abs} = 5.2\,\text{V}$, the grating with 830 lines/mm was used. The grating with 600 lines/mm was used for the other driving conditions. Therefore, for an accurate comparison, the d-scan traces are plotted with the dispersion axis in GDD units.

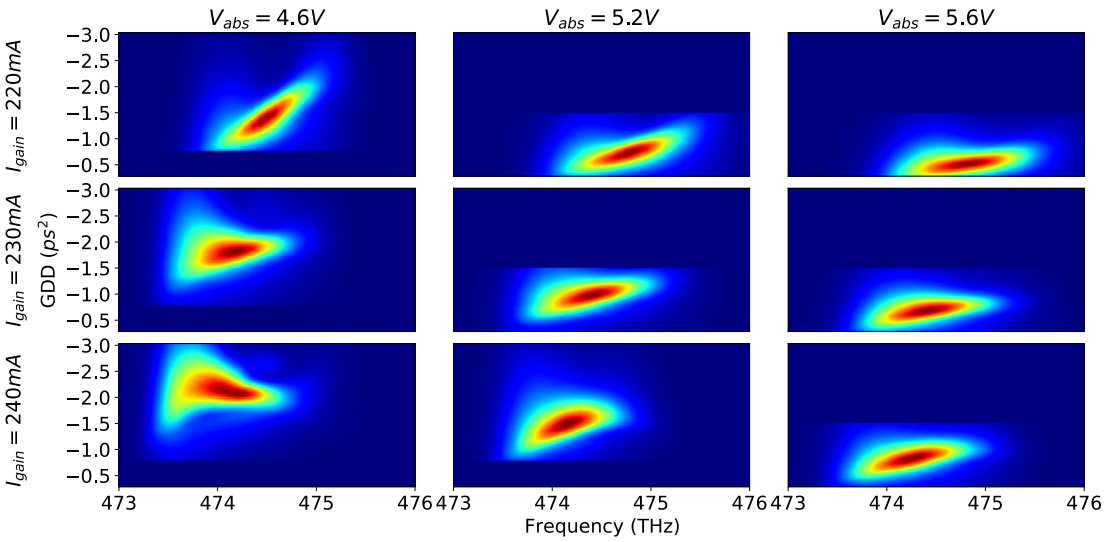


Figure 4.1: Measured d-scan traces for different values of I_{gain} (rows) and V_{abs} (columns).

The traces show that the chirp is heavily influenced by the parameters applied to the QD laser. Namely, increasing I_{gain} strongly increases the chirp of the pulses, which can be directly inferred by the rise of the traces' center of mass on the dispersion axis (meaning

that more negative dispersion needs to be applied to fully compress the pulses regarding second order dispersion). Increasing V_{abs} has a contrary effect, as it decreases the chirp of the pulses. All the traces appear tilted, providing evidence of third-order dispersion (TOD). For I_{gain} = 220 and 230 mA, increasing V_{abs} leads to a decrease of TOD, as the traces appear less tilted. However, for I_{gain} = 240 mA, there is a TOD sign inversion, as for V_{abs} = 4.6 V the trace is tilted in the opposite direction compared to the ones obtained for V_{abs} = 5.2 and 5.6 V.

4.3. Spectral power and phase retrieval

The follow-up retrieval process relies on the ptychographic algorithm, introduced in the previous chapters. As an illustration, the measured and retrieved d-scan traces for $I_{gain} = 230\,\text{mA}$ and $V_{abs} = 5.2\,\text{V}$ are shown in Figure 4.2.

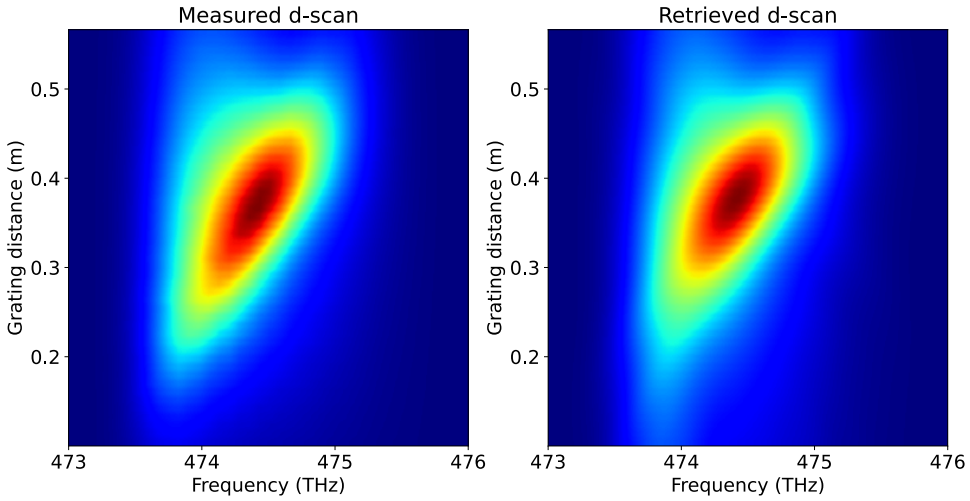


Figure 4.2: Measured and retrieved d-scan trace for $I_{gain} = 230\,\text{mA}$ and $V_{abs} = 5.2\,\text{V}$.

The mean d-scan error G was 8.2% for a set of 10 retrievals, which can again be explained by the presence of noise in the trace that is not retrieved by the algorithm. Nevertheless, the measured and retrieved d-scan traces are in excellent agreement, proving the algorithm's effectiveness. The mean d-scan errors G obtained for each d-scan trace retrieval can be seen in Table 4.1.

$I_{gain} \setminus V_{abs}$	4.6 V	5.2 V	5.6 V
220 mA	7.0%	4.2%	7.4%
230 mA	6.4%	8.2%	7.5%
240 mA	7.0%	5.9%	6.2%

Table 4.1: D-scan error G obtained for the retrieved d-scan traces.

The retrieved mean spectral power and phase, as well as the standard deviation, for the measured pulses, can be seen in Figure 4.3. The retrieved spectral phase shown corresponds to the pulses obtained right after the laser, and not after the grating compressor, to get a better sense of the influence of the bias conditions on the laser behaviour.

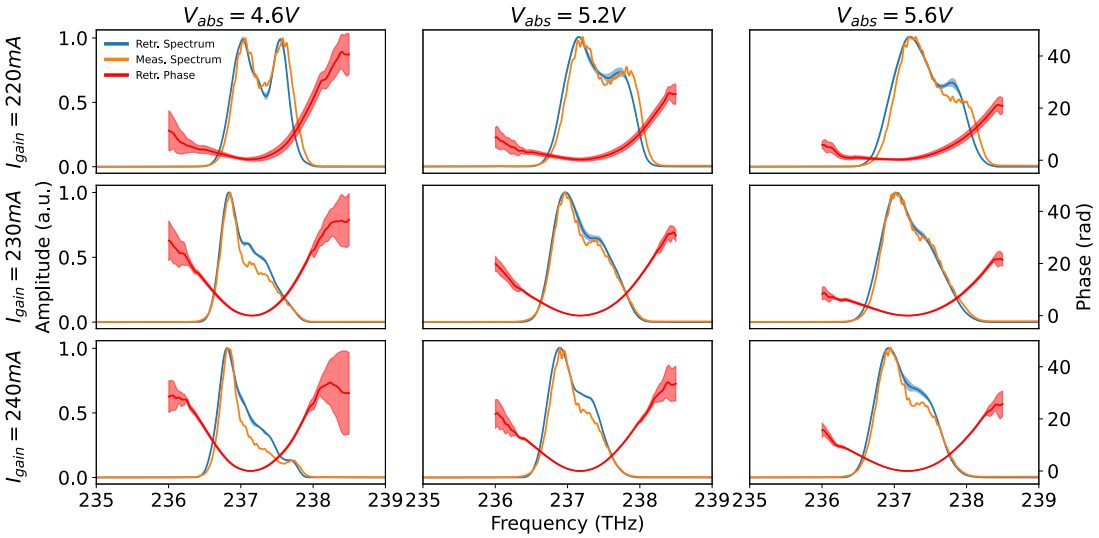


Figure 4.3: Retrieved spectral power (blue) and phase (red), together with an independent spectral measurement (orange) of the pulses obtained at different values of I_{gain} and V_{abs}. The blue and red shaded regions correspond to the standard deviation for the spectral power and phase retrievals, respectively.

For all measurements, we can say that the retrieved spectral power is in good agreement with the measured one. For $I_{gain} = 220\,\text{mA}$, the retrieved spectral power has a lower frequency cut compared to the measured one, which could be indicative of the spectral areas that do not contribute to the mode-locking regime. Nevertheless, they are still in good agreement with the measured spectral powers. Increasing V_{abs} leads to a blue-shift on the measured spectrum, while increasing I_{gain} red-shifts the spectrum. Visually, the spectrum appears to broaden when increasing V_{abs}. The same happens if we decrease I_{gain}.

Regarding the retrieved spectral phase, we can see that the second-order phase term (related to the GDD inherited by the pulses), increases with increasing I_{gain} and decreasing V_{abs}, which was already recognized when analyzing the d-scan traces. We can also see that the spectral phase is asymmetric, with the asymmetry being more accentuated for low drive currents. Due to the presence of a saturable absorber in the QD laser, and the underlying processes that occur in the former, the leading edge of the pulse (which in these cases are the lower frequency components) is more affected by the SA, causing the phase asymmetry that is visible in the retrieved spectral phase.

4.4. Temporal profile visualization

If we visualize the pulses in the temporal domain, we get the results from Figure 4.4.

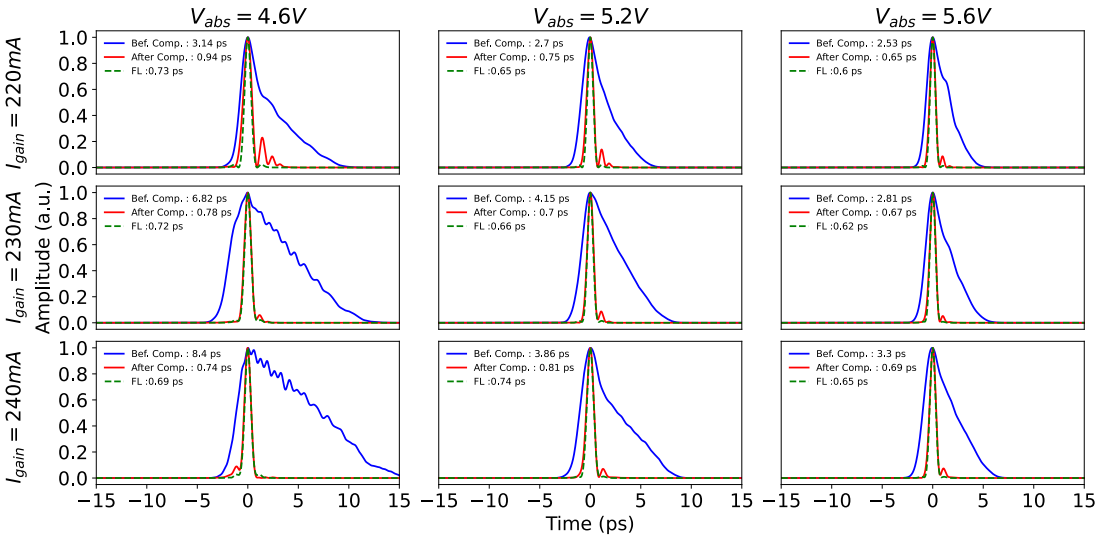


Figure 4.4: Temporal profile of the QD laser pulses obtained at different values of I_{gain} and V_{abs}, uncompressed (blue), compressed (red), and Fourier-limited (green).

As a first analysis, the results show that, before compression, the pulse width increases generally with increasing I_{gain} and decreasing V_{abs}. There is also a clear pulse asymmetry visible for all values of I_{gain} and V_{abs}, where the trailing edge has a slower decay compared to the leading edge, which was already visualized in previous FROG [25, 104], FRMZG [106] and sonogram [109] measurements of similar laser sources.

Let us shift our attention to the chirp of these pulses. As an example, Figure 4.5 shows the retrieved spectral phase, as well as a polynomial fit, of the pulses obtained at $I_{gain} = 230\,\text{mA}$ and $V_{abs} = 4.6\,\text{V}$.

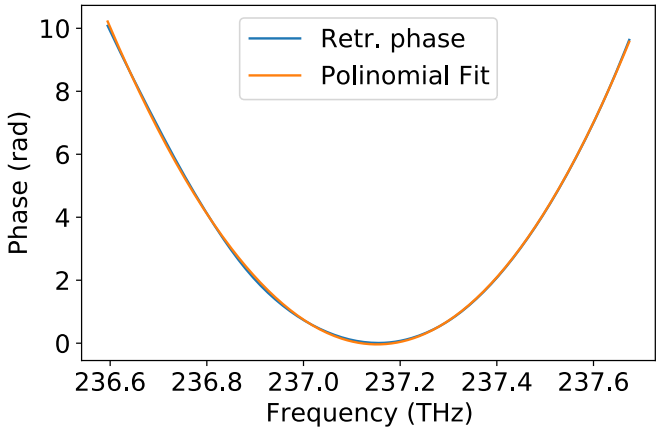


Figure 4.5: Retrieved spectral phase (blue) and the correspondent polynomial fit (orange) of the pulses obtained at $I_{gain} = 230\,\text{mA}$ and $V_{abs} = 4.6\,\text{V}$.

From the polynomial fit, we can estimate a value of GDD equal to $1.8\,\mathrm{ps}^2$, which is in good agreement with previous observations [125], and a value of TOD equal to $0.05\,\mathrm{ps}^3$. However, previous measurements of the Group Velocity Dispersion in InAs/GaAs QD lasers show that this value is around $2270\,\mathrm{fs}^2\mathrm{mm}^{-1}$, mainly due to the dispersion of bulk GaAs [126] which, for a cavity length of $8\,\mathrm{mm}$, translates to a net GDD of $0.036\,\mathrm{ps}^2$. Although these measurements were not performed in the laser investigated in this thesis, they serve as a starting point to state that the dispersion introduced by the QD materials is orders of magnitude below the actual dispersion of the measured pulses, which means that other mechanisms must be responsible for the pulse broadening in QD lasers. This mechanism is self-phase modulation.

Unlike in solid-state lasers, where SPM is caused by the optical Kerr effect, SPM in semiconductor lasers behaves differently. During propagation of the optical pulse inside the cavity, specifically in the gain section, the stimulated emission causes the carriers to recombine, thus depleting the carrier density and, therefore, the gain. The carrier density depletion is dependent on the optical intensity, which changes across the laser pulse. This means that the refractive index changes across the pulse as well, leading to a phase change on the pulse. Since the instantaneous frequency is defined as the time derivative of the phase, the instantaneous frequency changes across the pulse as well, proportionally to the derivative of the time-dependent refractive index. This leads to the creation of new frequencies inside the pulse, which are spread out across the temporal profile (typically the lower frequencies being on the leading edge of the pulse and the higher frequencies being on the trailing edge of the pulse) [127]. Propagating this pulse in a dispersive medium (such as the laser itself) creates a pulse broadening because the trailing edge of the pulse (with higher frequency components) propagates slower than the leading edge of the pulse (with lower frequency components), effectively leading to a positive dispersion across the laser pulse.

At the same time, the saturable absorber behaves oppositely, since it generates carriers due to photon absorption, leading to a contrary effect regarding dispersion to that of the gain section. The relative contribution of both the gain and the absorption sections dictate the pulse behavior regarding temporal shape and chirp, as seen in Figure 4.6.

The effects of self-phase modulation can be seen by changing the drive current applied to the QD laser. For low values of drive current, most of the carriers in the QDs are consumed by the leading part of the pulse. As we increase the drive current further (for a

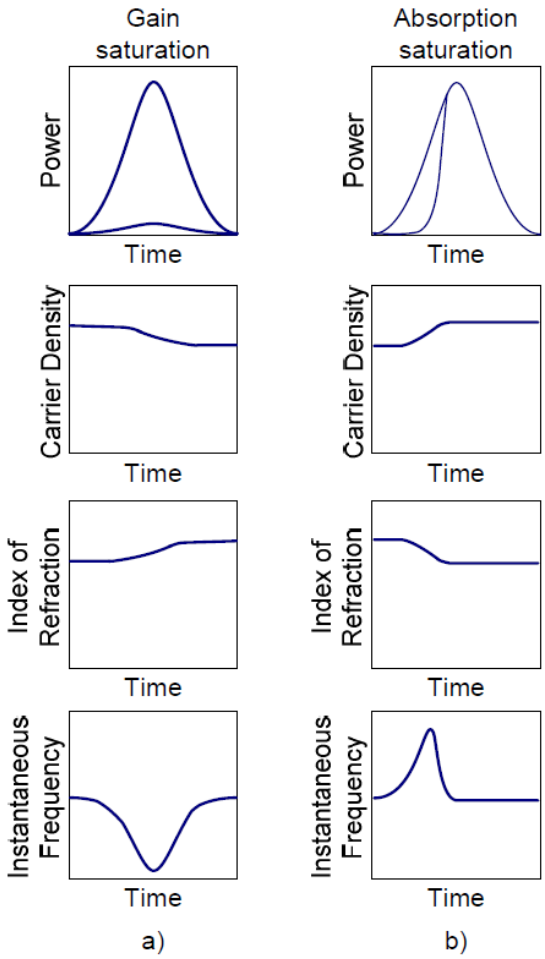


Figure 4.6: Effects of the self-phase modulation in a mode-locked semiconductor laser, regarding optical power, carrier density, index of refraction and instantaneous frequency in gain (a) and absorption (b) saturation regimes [127, 128].

fixed reverse bias voltage), the pulses experience a larger gain and gain-induced self-phase modulation, and the gain dynamics become more pronounced for the pulse shaping, which causes a flattening of the trailing edge and a consequent strong asymmetry in the pulse shape [24, 104], which is in good agreement with the results obtained in this thesis and with previously published experimental [25, 129] and theoretical [130] results. Regarding the saturable absorber dynamics discussed before, increasing the reverse bias voltage leads to a stronger saturable absorption and to an overall reduction of the pulse power within the laser medium, which in turn leads to a less intense SPM and, consequently, less chirped pulses. The strong pulse asymmetry can be explained by the fact that the leading edge of the pulse is more strongly affected by the saturable absorber. We have also seen that the front edge of the pulse remains nearly independent of I_{gain}, [104], and the pulse broadening is due to an increase in the trailing edge width [24].

It is important to mention that both the absorption and gain saturation and recovery times

define the net gain window, where pulse generation is possible, and increasing the reverse bias voltage leads to an overall decrease in the net gain window due to the absorption recovery speed increase.

For specific driving conditions, we can also detect two different decay times for the trailing edge of the pulses (clearly seen for I_{gain} = 240 mA and V_{abs} = 5.2 V, and for I_{gain} = 220 mA and V_{abs} = 4.6 V). Specifically for I_{gain} = 220 mA and V_{abs} = 4.6 V, if we visualize the retrieved spectral phase and the retrieved spectral power, we can easily correlate the existence of two different decay times in the trailing edge of the retrieved pulses with the strong asymmetry of the retrieved spectral phase. The red-sided part of the spectrum has a nearly flat spectral phase, while the blue-sided part of the spectrum has a strong quadratic spectral phase, which in the temporal domain is translated as the red-sided part of the pulse is almost compressed, creating a main pulse that is close to the transform-limited laser pulse, while the blue-sided part of the pulse creates a slow decay on the trailing edge due to the imparted linear chirp.

For low applied reverse bias voltages, a trailing edge modulation appears on the measured pulses, in good agreement with previous sonogram measurements [109].

For a fixed drive current I_{gain} = 220 mA, the decrease on the pulses' FWHM from V_{abs} = 4.6 V to 5.6 V is 19%, a smaller value than the one obtained for I_{gain} = 240 mA (61%). If we now fix V_{abs} = 5.6 V, we see that the pulses' FWHM, for I_{gain} increasing from 220 mA to 240 mA, increases by 30%, a smaller value than the one obtained for V_{abs} = 4.6 V (168%). From this information, we can infer that the influence of V_{abs} on the pulses' chirp gets stronger for higher I_{gain}, whereas the influence of I_{gain} decreases with V_{abs}.

D-scan offers the accompanying compression of the pulses, which can be seen in the red curves in Figure 4.4. At their maximum compression point, all the pulses were compressed to near transform-limit, with pulse widths in the 600-900 fs range (in the sub-ps region). For I_{gain} = 220 and 230 mA, we can see small post-pulses (result of the TOD present in the pulses), whose amplitude decreases with increasing V_{abs}. For I_{gain} = 240 mA and V_{abs} = 4.6 V, there is a small pre-pulse, which converts into a post-pulse for increasing values of V_{abs}, which is in good agreement with the earlier visual analysis of the d-scan traces.

4.5. Pulse measurement across the dispersion range

We can also study the temporal profile evolution of the pulses as a function of the applied dispersion since we have information about the spectral power and phase of the pulses. The evolution of the temporal profile of the retrieved pulses can be seen in Figure 4.7, which can give us some extra information to corroborate previous conclusions.

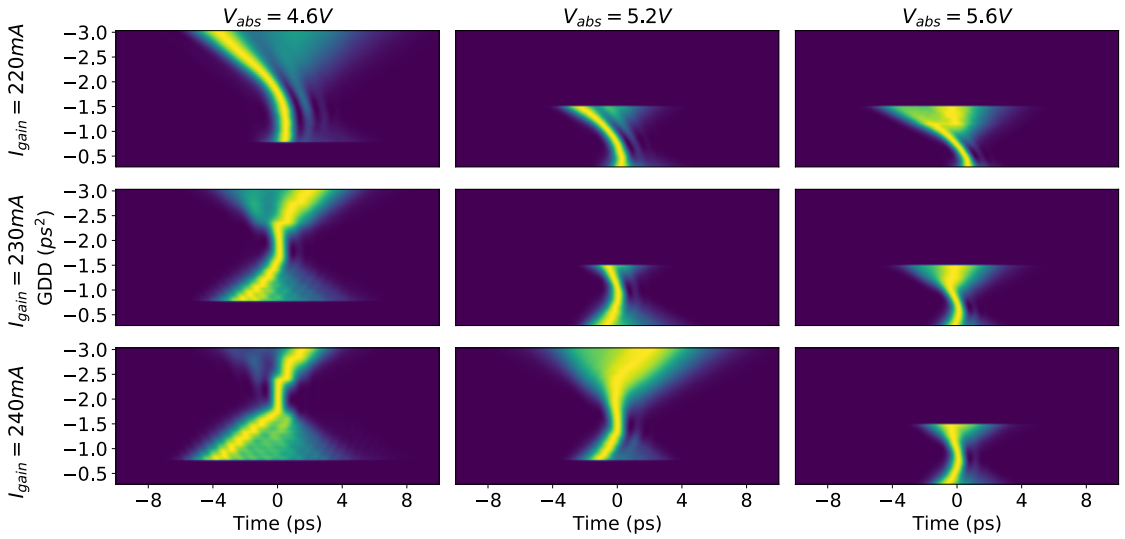


Figure 4.7: Temporal profile evolution of the QD laser pulses obtained at different values of I_{gain} and V_{abs}, as a function of the dispersion applied to the laser pulses.

As an example, let us take into account the evolution of the pulses obtained at $I_{gain} = 240\,\text{mA}$ and $V_{abs} = 5.2\,\text{V}$. The original, uncompressed pulse that is obtained directly from the QD laser is extremely asymmetric, with a trailing edge longer than the leading edge and the trailing edge having two different decay times. However, simply by adding more or less dispersion, we can change the temporal shape of the pulse, from drastically reducing the trailing edge (orange curve in Figure 4.8) to completely reversing the asymmetry and creating a leading edge that is longer than the trailing edge (green curve in Figure 4.8), which can prove useful for many different applications, such as pulse amplification with a minimization of the gain saturation effect.

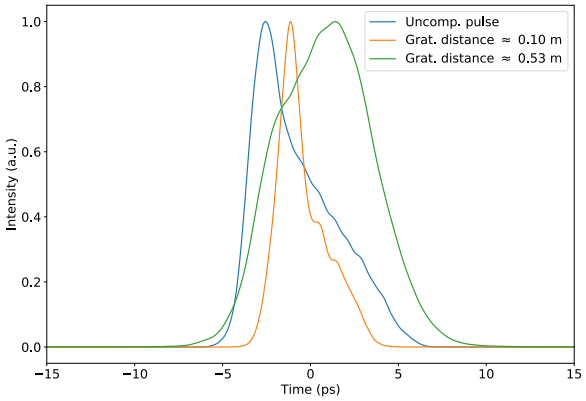


Figure 4.8: Temporal profile of the QD laser pulses at $I_{gain} = 240\,\text{mA}$ and $V_{abs} = 5.2\,\text{V}$, before (blue), and after the compressor with a grating distance of 0.1 (orange) and 0.53 (green) meters.

4.6. Conclusions and future work

In this section, we have used the highly-sensitive dispersion scan setup to characterize pulses from a semiconductor laser diode, study the influence of drive current and reverse bias on the evolution of the pulse temporal profile, as well as correlate our findings with theoretical models, and previous experimental results. We have also compressed these pulses to near their Fourier transform-limit, to a sub-ps regime.

An interesting solution to obtain transform-limited pulses would be to filter out the portion of the spectrum whose spectral phase is not relatively flat. An interesting example would be the case of pulses driven at $I_{gain} = 220\,\text{mA}$ and $V_{abs} = 5.6\,\text{V}$. The lower frequencies have almost a zero linear chirp, which would mean that, by filtering out the higher frequencies, the output pulse would be close to transform-limited. A simulation of this filtering effect can be seen in Figure 4.9, which shows that by filtering some frequencies that have a non-zero linear chirp, the pulses could be close to transform-limited without the need for a post-compression scheme.

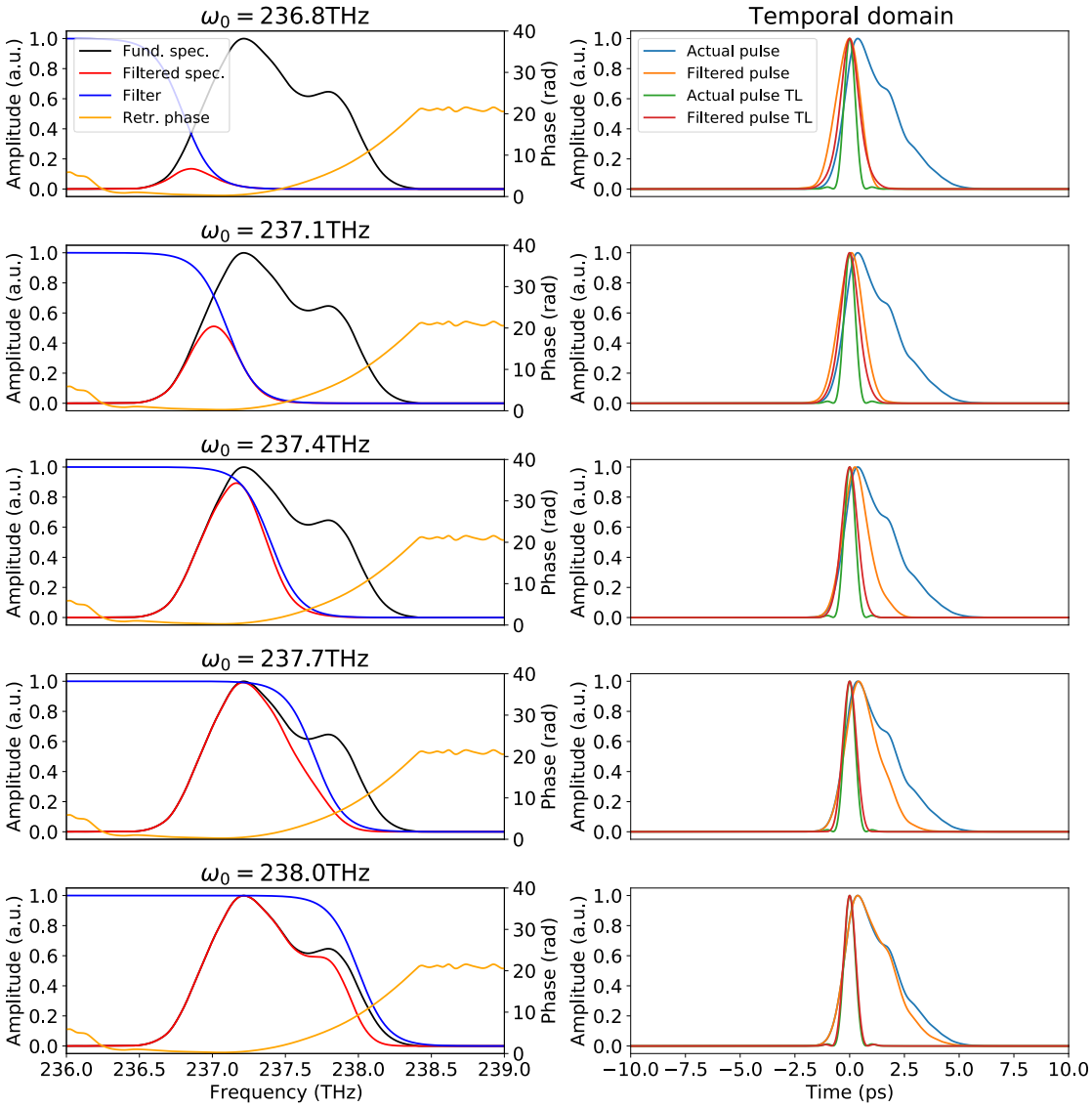


Figure 4.9: Left: retrieved spectral profile (black) and phase (orange) for pulses driven at $I_{gain} = 220$ mA and $V_{abs} = 5.6$ V, together with the filtered spectrum (red), filtered by a logistic filter with central frequency ω_0 (blue). Right: respective temporal profile, uncompressed (blue) and transform-limited (orange) for the retrieved fundamental spectrum, as well as the uncompressed (green) and transform-limited (red) temporal profiles for the filtered pulses.

5. Quantification of pulse train instabilities in semiconductor laser diodes

In this chapter, we will present our results regarding the detection and, for the first time to the best of our knowledge, quantification of pulse train instabilities in semiconductor laser diodes using the developed d-scan setup, together with a self-calibrating d-scan retrieval algorithm. We have identified the different mode-locking regimes that occur on the studied quantum-dot laser, and their dependence on the drive current and reverse bias voltage.

5.1. Pulse train instabilities

The first observation of pulse train instabilities in intensity autocorrelation measurements was made in 1969 by Fisher and Fleck [131], where they saw that, if the pulse shape varies on a timescale shorter than the measurement time, a narrow temporal structure arises at the center of the autocorrelation, which is commonly known as the coherent artifact.

Pulse train instabilities are one of the main problems standing between ultrafast semiconductor laser diodes and their globalization, mainly due to the current limitation in pulse duration for pulses obtained with these laser sources. As stated before, driving these lasers at high drive currents, which could provide the spectral bandwidth necessary for transform-limited sub-100 fs pulses, leads to pulse train instabilities, suppressing the possibility of using these laser sources as stable sources capable of delivering laser pulses with very short pulse duration. Several groups reported the observation of pulse train instabilities in FROG measurements [23, 25] where, for high drive currents, a coherent artifact appeared in the FROG trace, causing the phase retrieval algorithm not to converge, leading to no pulse retrieval. Since FROG is a time-frequency methodology, small variations in the pulse structure result in different spectrograms, and the obtained measurement consists of the sampled pulse train average. Nevertheless, Li *et al.* [23] developed a semi-empirical model to extract qualitative information regarding the pulse train instabilities and coherence from the FROG trace.

The characterization techniques presented in chapter 1 can, with more or less detail retrieve information about the output pulses of arbitrary laser sources. However, unless the method uses a single-shot technique (technically capable of measuring a single instance of the pulse train) an autocorrelation, FROG, SPIDER, or d-scan trace all consist of the

average of a multitude of pulses within the pulse train. If the pulse train is stable, the measurement is not affected and is equivalent to measuring a single pulse. However, suppose there are pulse train instabilities of some sort. These can range from a random group delay dispersion, which can happen when dispersive elements are used with a laser source with pronounced beam pointing instability or when pulse energy fluctuates in a self-phase-modulating medium, to a degraded interpulse coherence or partial mode-locking [132]. If there are pulse train instabilities, each pulse in the pulse train will be different, and the traces obtained will correspond to an average of all these pulses [133]. In a d-scan measurement, for example, the resulting d-scan trace is of the form:

$$T(\omega,z)=\frac{1}{N_p}\sum_{j=1}^{N_p}\left|\mathcal{F}\left[\mathcal{F}^{-1}\left[|E_j(\omega)|e^{i\varphi_j(\omega)}e^{i\phi(\omega,z)}\right]^2\right]\right|^2 \tag{5.1}$$

where N_p is the number of pulses considered. A similar expression can be deduced for the other characterization techniques. Pulse train instabilities and their effect on other pulse measurement techniques have also been studied [51, 134, 135].

Let us study, for example, the influence of these pulse train instabilities in an autocorrelation trace. We will consider three main sources of instability: the first source is a random linear chirp instability, where the spectral phase of each pulse is given by:

$$\varphi(\omega)=\frac{1}{2}\left(GDD_{base}+\alpha\right)\left(\omega-\omega_0\right)^2;\alpha\sim N(0,\Gamma) \tag{5.2}$$

where GDD_{base} is the base, stable GDD that is added to each pulse, and α parametrizes the GDD instability added to the pulses. This instability follows a normal zero-centered distribution $N(0,\Gamma)$ with a standard deviation equal to Γ, which parametrizes the amount of instability added to the pulse train.

The second source of pulse train instabilities consists of a random phase that is added to each pulse:

$$\varphi(\omega)=\frac{1}{2}GDD_{base}\left(\omega-\omega_0\right)^2+\gamma\Phi(\omega);\Phi\sim U(-\pi,\pi) \tag{5.3}$$

where $\Phi(\omega)$ is a random phase that follows a uniform distribution $U(-\pi,\pi)$, and γ is the intensity of this instability. In this case, the generation of the pulse train follows a slightly different approach. Since the spectral phase is random, the temporal field will be infinitely

long. To maintain the desired average pulse duration, we add the spectral phase to the pulse, we apply an inverse Fourier transform to go to the temporal domain, and multiply the obtained temporal profile by a Gaussian filtering function with a width equal to the known average temporal duration of the pulse. This method was used by Pfeifer *et al.* to study partially coherent free-electron laser pulse statistics [136].

The third and last studied source of instability consists of a double-pulsing regime, with mutual (or relative) timing jitter, where the temporal distance between both pulses is not constant:

$$E(t) \rightarrow E(t-\tau) + E(t+\tau); \tau \sim N(\Delta t, \Delta t) \tag{5.4}$$

where τ is a mutual pulse delay equal to half the temporal distance between pulses, which is selected based on a normal distribution $N(\Delta t, \Delta t)$ with center and standard deviation equal to Δt.

We have simulated, for each of these pulse train instabilities, a set of 2000 Gaussian-shaped pulses, each with a center wavelength of $1264\,\text{nm}$ and capable of supporting transform-limited 600 fs pulses. For the first instability, $GDD_{base} = 0.3\,\text{ps}^2$. For the second, $GDD_{base} = 0.5\,\text{ps}^2$ and for the third instability, $GDD_{base} = 0.1\,\text{ps}^2$. The autocorrelation traces obtained can be seen in Figure 5.1.

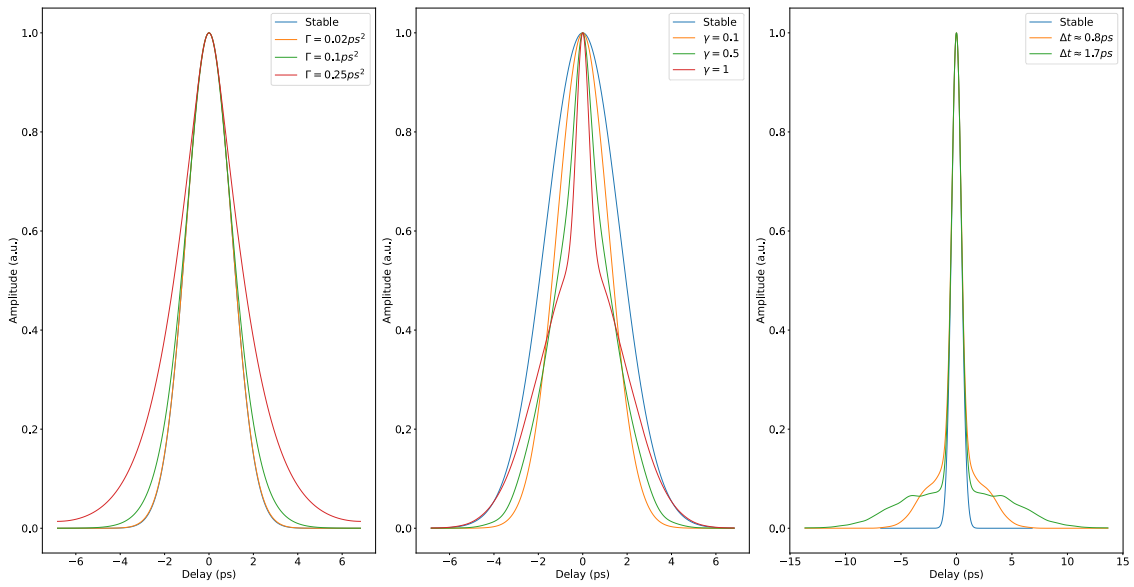


Figure 5.1: Autocorrelation traces for a pulse train with random chirp instability (left), random phase distribution (middle), and double-pulsing with mutual timing jitter (right). The blue curves are the autocorrelation traces of the stable pulse train for each situation. On the left graphic, the blue curve is almost indistinguishable from the orange curve.

One crucial conclusion is that random chirp instability is almost invisible to autocorrelation measurements [132]. With a strong enough random phase distribution, a coherence artifact appears on top of the autocorrelation trace. In the case of a train of variably spaced double pulses, the autocorrelation trace exhibits a coherent artifact, resulting from the non-random coherent component of the double pulses (a single pulse), on top of a broad background resulting from the overall average pulse length (the combination of both pulses) [134]. Although some information can be extracted from these autocorrelation traces, the bigger picture cannot be seen, and the information obtained can be misleading. The non-uniqueness of autocorrelation further degrades this situation.

5.1.1 D-scan simulations

Modern pulse measurement techniques, such as FROG, SPIDER, and d-scan, provide further information regarding pulse train instabilities. On a pulse train with linear chirp instability, SPIDER can measure the correct average spectral phase and should yield an accurate value for the average chirp of the pulse train [132, 137]. FROG can be used to qualitatively separate the contributions of the average pulse and the coherent artifact [50], but quantifying these instabilities remains a problem to be solved since the retrieval algorithms fail as soon as the pulses become unstable.

D-scan, being a one-beam geometry, is not corrupted by time-delay variations unlike SPIDER and FROG, and small chirp fluctuations or even a weak coherent artifact immediately distorts the d-scan trace, which can be used to clarify the presence of unstable mode-locking. Benjamin *et al.* [138] have shown the effect of chirp instability and random phase fluctuations on d-scan traces, concluding that both cause a stretch on the dispersion axis in the d-scan trace. In the presence of instabilities, the optimum dispersion point for compensation of the spectral phase for the different wavelengths of the pulse also inherits that instability and the nonlinear signal is redistributed along the dispersion axis.

A simple simulation showing the effect of a random linear chirp instability can be seen in Figure 5.2. We have generated a set of 3000 Gaussian spectra, each with a center wavelength of 1264 nm, capable of supporting 600 fs pulses. For the simulations shown here, $GDD_{base} = 1.4\,\text{ps}^2$, and Γ ranges from $0.1 ps^2$ to $0.7 ps^2$. In all the presented simulations, for the compressor, we have simulated the single-grating compressor used in chapter 3, using the grating with 800 lines/mm and a blaze wavelength of $1.2\,\mu m$.

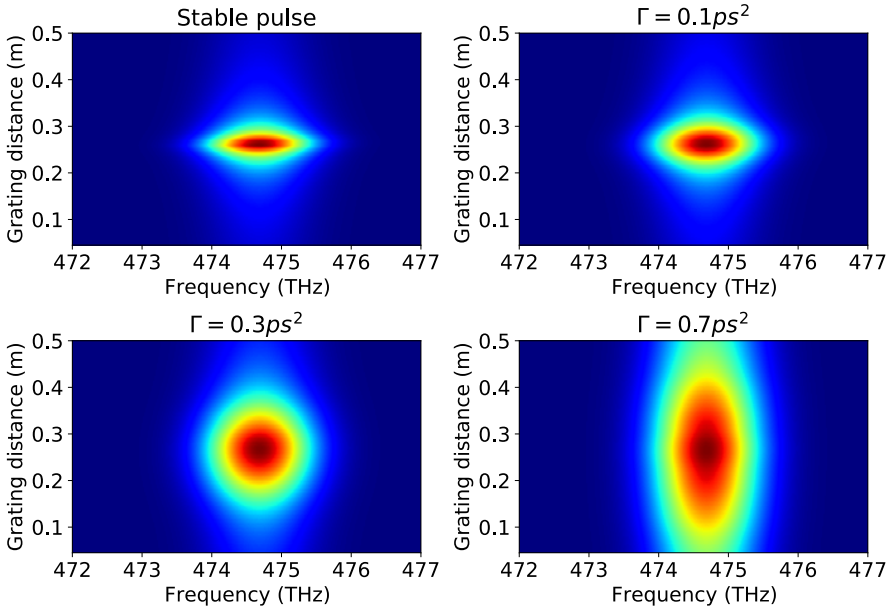


Figure 5.2: (a) Base pulse d-scan trace for comparison. (b) to (d): Simulated d-scan trace using a pulse train with linear chirp instability, with $\Gamma = 0.1\,\text{ps}^2$ (b), $\Gamma = 0.3\,\text{ps}^2$ (c) and $\Gamma = 0.7\,\text{ps}^2$ (d).

The effects of the random phase fluctuation described previously can be seen in Figure 5.3. This effect also distorts the d-scan trace, although its effects are much stronger for high instability values.

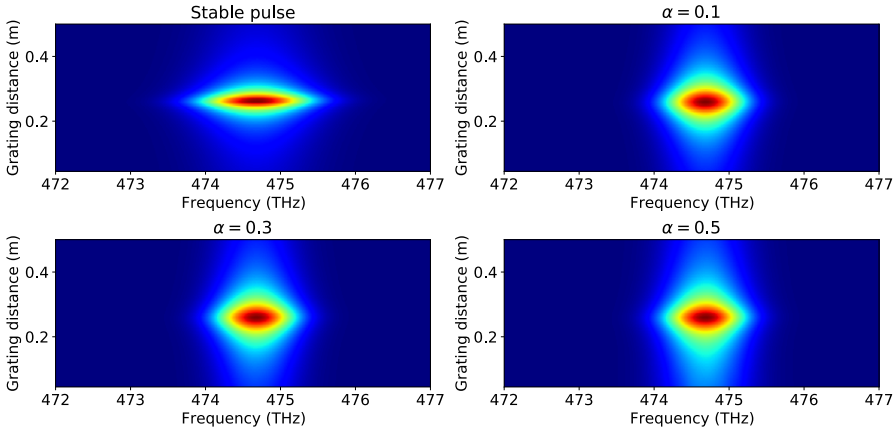


Figure 5.3: D-scan simulation of a random phase fluctuation regime, with a base pulse with $GDD = 1.4ps^2$ and $\alpha = 0.1$ (b), $\alpha = 0.3$ (c) and $\alpha = 0.5$ (d). Base pulse d-scan trace for comparison (a).

5.2. Measurement of pulse train instabilities

The question remains: can we quantify the pulse train instabilities that exist in a laser source?

For the d-scan technique, three main methods have been used to study pulse train instabilities in laser sources: fidelity measurement [139], mixed-state reconstruction [140], and the self-calibrating d-scan [141].

The fidelity measurement $F(z)$, introduced firstly in [139] for Multiphoton Intrapulse Interference Phase Scan (MIIPS), compares the experimental trace $T_{meas}(\omega, z)$ with the theoretical trace of the transform-limited pulse $T_{sim}^{TL}(\omega, z)$:

$$F(z) = \frac{T_{meas}(z)}{T_{sim}^{TL}(z)} \tag{5.5}$$

which indicates the spreading of the trace in the dispersion axis, acting as a quick indication of partial coherence in a pulse train. However, it provides limited information, and the effect of the average pulse width is not linear with the fidelity [142], which limits the information we can extract from the fidelity measurement if the pulses are not transform-limited.

The mixed-state reconstruction method was already used to measure partially coherent attosecond pulses [140]. It consists of retrieving several electric fields that are representative of the d-scan trace obtained, where each field is a variation of the pulse shape in the train. It is a powerful method, that allows retrieving stable pulse trains and typical representations of the pulse shapes obtained in an unstable pulse train. However, since increasing the number of retrieved pulses in the ensemble improves the retrieval accuracy, the computational cost obtained by increasing the number of retrieved pulses becomes a problem when this number is large.

5.3. Self-calibrating d-scan

The method used in this work is the self-calibrating d-scan [141], which allows measuring an ultrashort pulse without knowing the dispersion applied by the compressor by retrieving not only the spectral phase of the laser pulse being measured but also the phase introduced by the compressor during the measurement process. The uncalibrated compressor introduces a phase $\phi(\omega, z)$ that depends on the compressor position (if it is, for example, a prism or grating compressor) or the inserted thickness of the material (if it is, for example, a chirped mirrors and glass wedges compressor). This phase can also be expanded on a Taylor series:

$$\phi(\omega,z) = \phi_0(z) + GD(z)\,(\omega-\omega_0) + \frac{1}{2}GDD(z)\,(\omega-\omega_0)^2 + \frac{1}{6}TOD(z)\,(\omega-\omega_0)^3 + ... \tag{5.6}$$

where ω_0 is the central frequency. The variables ϕ_0 and GD (Group Delay) do not change the d-scan trace and are, therefore, neglected. Since it uses a multi-variable optimization algorithm, the self-calibrating variant adds more variables to be optimized, namely the GDD and the TOD values of the compressor being used (which are typically sufficient to model the dispersion applied by the compressor), allowing the d-scan technique to be implemented with virtually any dispersion scanning setup by retrieving the pulse and calibrating the compressor simultaneously.

The self-calibrating d-scan retrieval has been previously used to detect and quantify pulse train instabilities in fiber lasers [138]. The key factor in this method is retrieving the phase introduced by the compressor, and using this value as an input to an instability metric Γ, described in this work as:

$$\Gamma = 1 - \frac{GDD_{retr}}{GDD_{real}} \tag{5.7}$$

where GDD_{retr} is the GDD retrieved by the self-calibrating algorithm, and GDD_{real} is the real GDD introduced by the compressor. If the pulse train is stable, the GDD retrieved by the algorithm will match the GDD of the compressor. However, suppose pulse train instabilities exist in the laser source. In that case, the algorithm will retrieve a GDD value smaller than the actual GDD from the compressor, to accommodate for the trace stretching along the dispersion axis. By numerically comparing the retrieved GDD with the actual GDD from the compressor through an appropriate metric, we can properly quantify these pulse train instabilities. The algorithm can also retrieve an average spectral phase and an average temporal profile [138].

5.4. Self-calibrating retrieval of stable pulses

To confirm that all pulses obtained in the previous chapter at these currents are stable, we have performed a self-calibrating retrieval algorithm of the pulses obtained at I_{gain} = 230 mA and V_{abs} = 4.6 V. Both measured and retrieved d-scan traces can be seen in Figure 5.4. The self-calibrating retrieval algorithm, as well as all the self-calibrating

retrievals performed in this thesis, were done by Dr. Benjamín Alonso, in collaboration with the University of Salamanca.

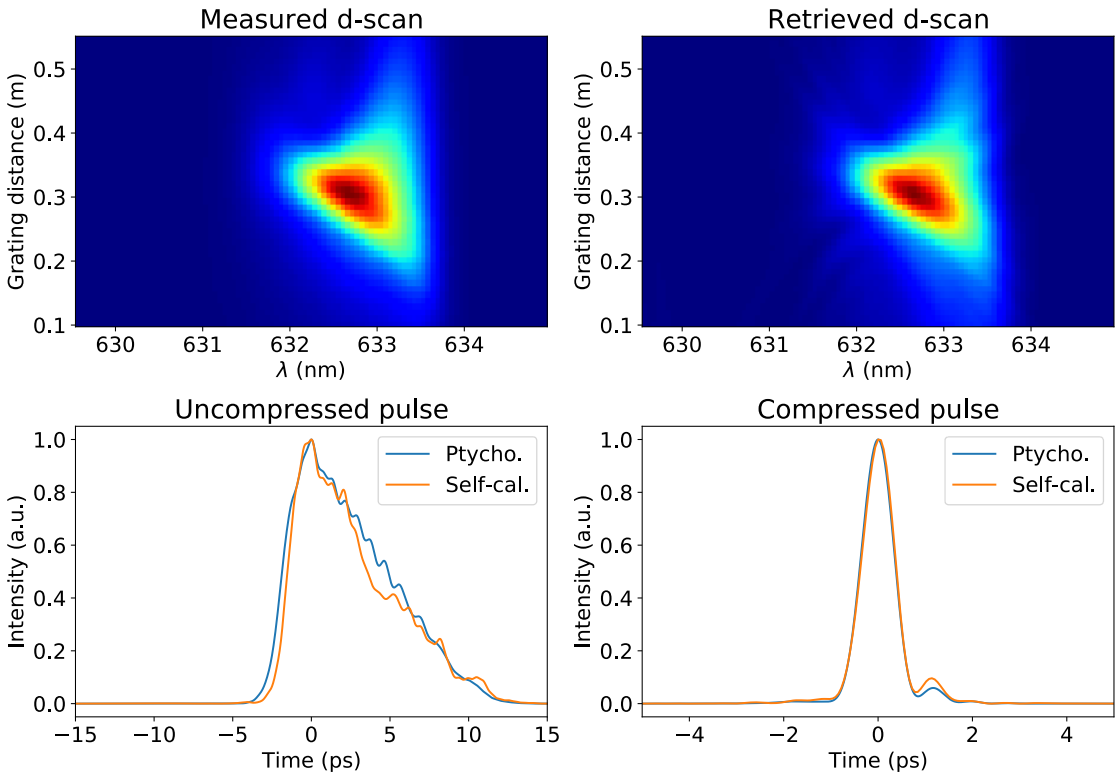


Figure 5.4: Measured (upper left) and retrieved (upper right) d-scan traces obtained at I_{gain} = 230 mA and V_{abs} = 4.6 V, using the self-calibrating retrieval algorithm. Retrieved uncompressed (bottom left) and compressed (bottom right) pulses in the temporal domain, using the ptychographic (blue curves) and the self-calibrating (orange curves) retrieval algorithm.

The retrieved d-scan trace is in good agreement with the measured one, which clearly indicates the algorithm convergence. The self-calibrating algorithm retrieved a GDD_{retr}/L value of $-5.4\,\mathrm{ps}^2/m$, which is in excellent agreement with the real GDD_{real}/L value of $-5.36\,\mathrm{ps}^2/m$ (both of these values were determined at $1265\,\mathrm{nm}$, and this wavelength will serve as reference throughout the rest of the thesis). If we use the instability metric defined by Alonso *et al.* [138], we can quantify the amount of instabilities that exist in a pulse train. For the stable case of I_{gain} = 230 mA and V_{abs} = 4.6 V, the instability metric is equal to -0.7% *, which is rather negligible.

This measurement demonstrates two vital points for this work: first, the pulses measured in the previous chapter are indeed stable (which was already proven by the convergence of the ptychographic retrieval algorithm); and second, the single-grating compressor is well calibrated, since the retrieved GDD_{retr}/L is in excellent agreement with the predicted,

*The negativity of the instability metric in this particular case can be solved by measuring the absolute value of the metric, and it is not significant in this case.

theoretical GDD_{real}/L value for the compressor geometry used in our experimental work. Both the compressed and uncompressed pulses retrieved using the self-calibrating algorithm are in good agreement with the ones obtained using the ptychographic algorithm, as seen in Figure 5.4. It is important to note that the self-calibrating retrieval consists of a single retrieval process, since in multi-variable optimization retrievals there is no significant variation of the retrieved pulse for different runs.

The small differences between the uncompressed pulse obtained through ptychography and the self-calibrating retrieval can be explained by the fact that the self-calibrating algorithm uses the experimental, measured optical spectrum, whereas the ptychography algorithm retrieves a spectral power as well, which is smoother due to the interpolation effect.

5.5. Measurement of pulse train instabilities

Let us first study the influence of drive current on the chirp and stability of the pulse train. We have measured d-scan traces for pulses obtained at a fixed reverse bias $V_{abs} = 4.6\,\mathrm{V}$, with a drive current ranging from 220 to 280 mA. These results can be seen, together with the self-calibrating retrieval results, in Figure 5.5. The retrieved d-scan trace corresponds to the actual d-scan trace obtained through the self-calibrating retrieval algorithm. To provide a visual indication of the presence of instabilities, we added a simulated d-scan trace using the measured spectral power and the retrieved spectral phase, but using the actual dispersion added by the compressor. Therefore, if there are instabilities in the pulse train, this simulated d-scan trace will be squeezed in the dispersion axis compared to the measured one, which provides a clear indication of pulse train instabilities. We should refer that the temporal pulse retrieved with this algorithm is an average of the entire set of pulses that were used in a d-scan measurement (for example, if a d-scan measurement takes 10 minutes, and the repetition rate of the laser is equal to $5\,\mathrm{GHz}$, a total of 3×10^{12} pulses is used in a single d-scan trace measurement).

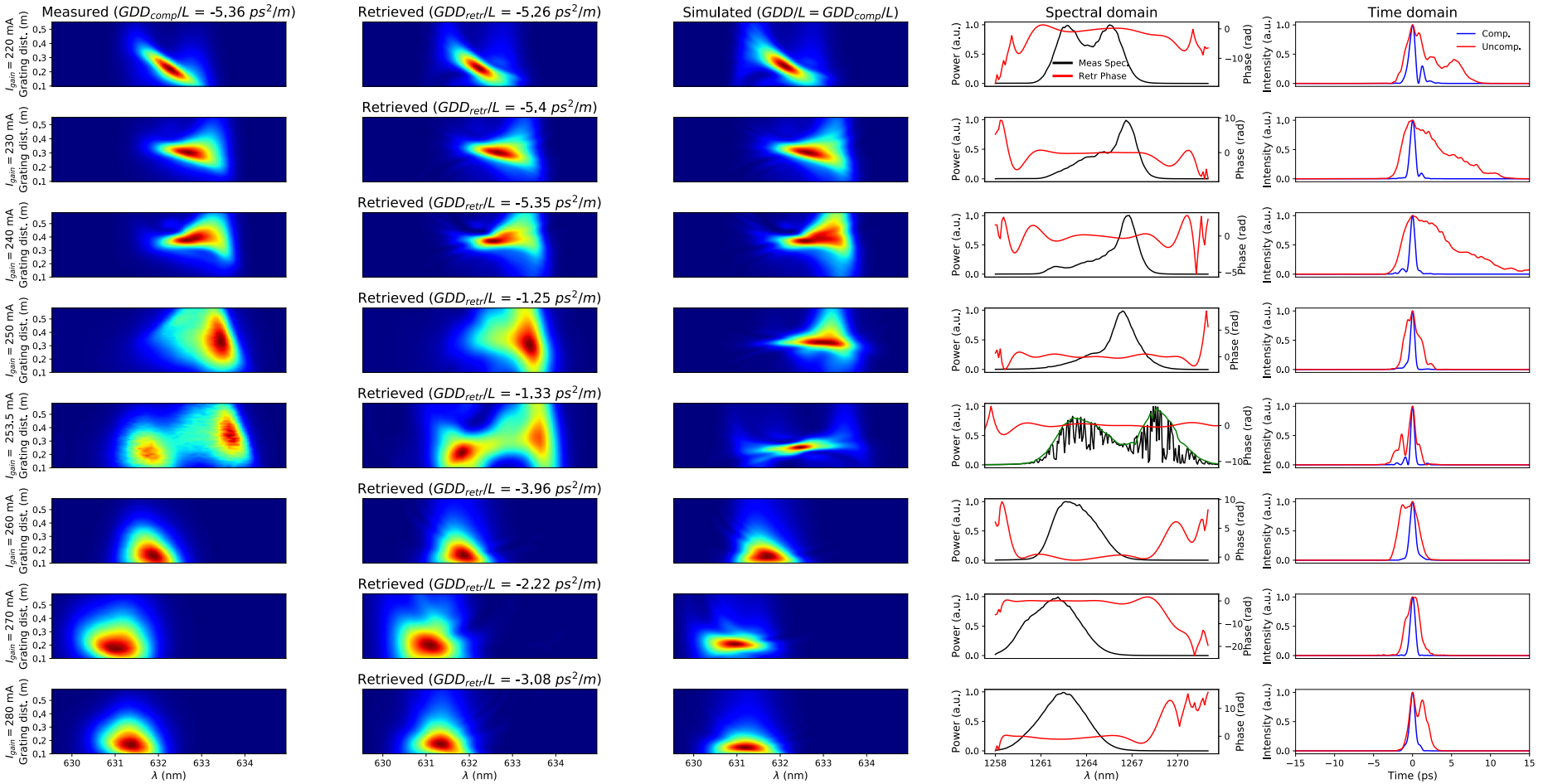


Figure 5.5: Experimental measurements for a constant reverse bias voltage (V_{abs} = 4.6 V). First column: measured d-scan traces for a drive current increasing from 220 mA to 280 mA. Second column: retrieved d-scan traces using the self-calibrating algorithm. Third column: d-scan trace simulation using the retrieved spectral phase, the measured spectral power, and the dispersion imparted by the compressor, for comparison. Fourth column: measured spectral power (black) and retrieved spectral phase (red) for the compressed pulse. For I_{gain} = 253.5 mA, the green curve was obtained by using the max hold function on the OSA. Fifth column: retrieved average pulse in the time domain, both compressed (blue) and uncompressed (red).

5.5.1 Mode-locking transition

Up to 240 mA, the retrieved d-scan traces are in excellent agreement with the measured ones. In these cases, the linear chirp of the pulse train increases as expected, since the amount of dispersion needed to fully compress the pulse (dictated by the grating distance where the nonlinear signal is maximized) increases as well, which was already discussed in the previous chapter.

For a current of 253.5 mA, a mode-locking transition appears, where the fundamental spectrum (and, implicitly, the d-scan trace) has a sudden blue-shift. In the spectral domain, that behavior is visible on the black curve, where the fundamental spectrum shifts constantly between the two mode-locked pulse trains (the green curve was obtained by measuring the spectrum using the max hold function on the OSA). For higher currents, there is a sudden drop in the chirp of the pulse train, due to the mode-locking transition observed, and the fundamental spectrum gets smoother and more Gaussian-like.

By using the instability metric previously defined, we can study the stability of the measured pulse trains. These results can be seen in Table 5.1. It is important to mention that the instability metric is a global measurement that accounts for all instability sources that cause temporal shape differences from pulse to pulse, and it is not defined for every individual kind of instability.

Current (mA)	GDD_{retr}/L (ps^2/m)	Γ (%)
220	-5.26	1.8
230	-5.4	0.8
240	-5.35	0.3
250	**-1.25**	**76.8**
253.5	**-1.33**	**75.2**
260	**-3.96**	**26.2**
270	**-2.22**	**58.6**
280	**-3.08**	**42.5**

Table 5.1: Instability metric for a constant reverse bias voltage (V_{abs} = 4.6 V), and a drive current changing from 220 mA to 280 mA. The real GDD/L introduced by the compressor is equal to $-5.36\,\mathrm{ps}^2/m$. The values in bold indicate driving currents where the retrieved GDD/L differs significantly from the actual GDD/L from the compressor, indicating the presence of pulse train instabilities.

With these results, we can easily indicate the stability regions of the mode-locking regime in semiconductor laser diodes. Up to 240 mA, the instability metric is negligible, indicating a stable mode-locking regime without pulse train instabilities. However, for drive currents between 250 and 260 mA, the instability metric becomes significant, reaching values as

high as 76,8%. For drive currents higher than 260 mA, the instability metric decreases for values between 26 and 58%, which will be explained further in the next section.

5.6. Map of instabilites

With these preliminary results, we can now measure the full map of instabilities for different values of drive current and reverse bias. The obtained d-scan traces can be seen in Figure 5.6. Complementary measurements of the fundamental optical spectrum, the average temporal profile of both compressed and uncompressed pulses, and the RF spectrum can be seen in Figure 5.7, Figure 5.8 and Figure 5.9, respectively.

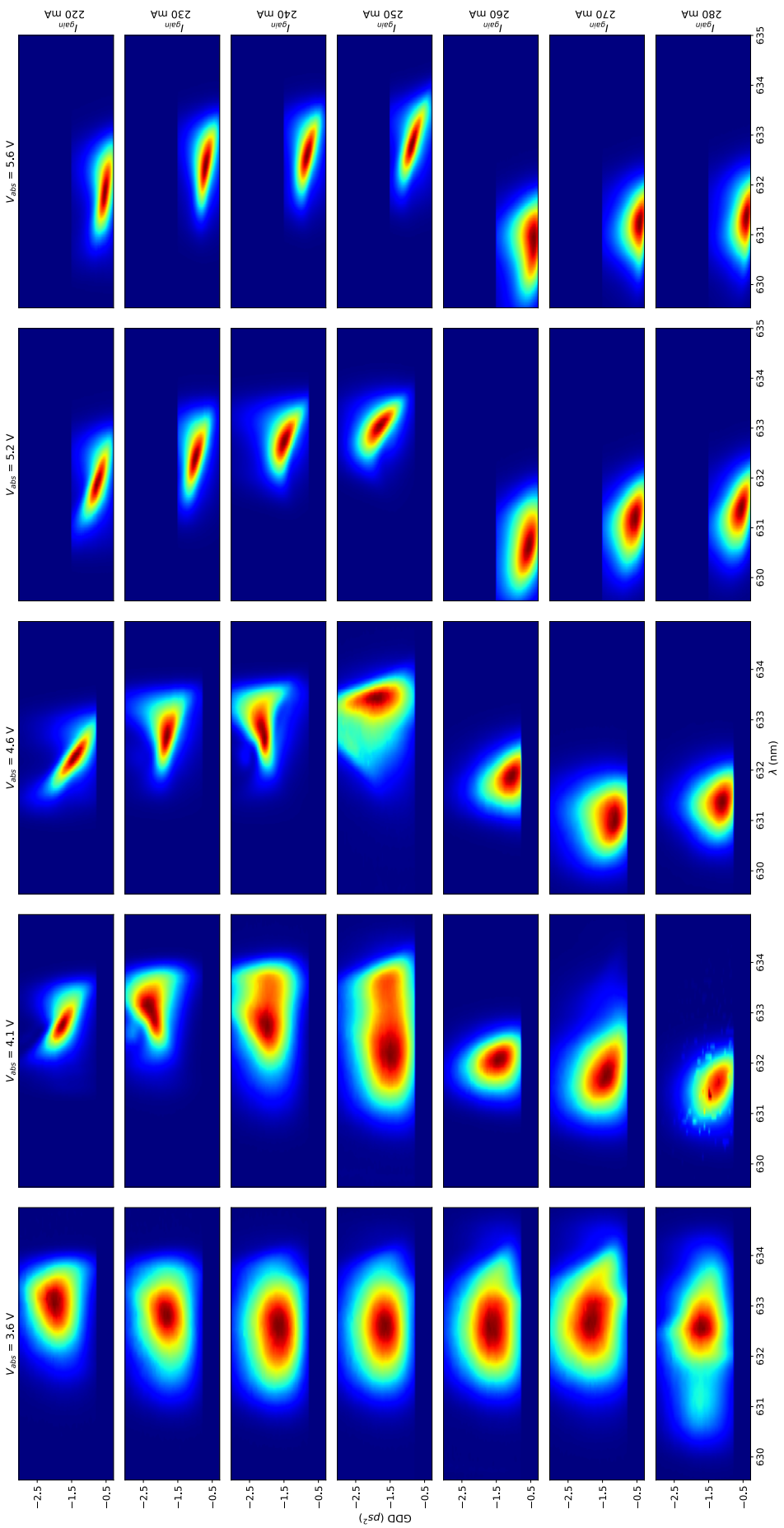


Figure 5.6: Full map of the measured d-scan traces for different values of drive current (220 mA $\leq I_{gain} \leq$ 280 mA) and reverse bias voltage (3.6 V $\leq V_{abs} \leq$ 5.6 V). Since two different gratings were used for different drive conditions, the y-axis was renormalized to the GDD applied by the compressor, for a more direct comparison between d-scan traces.

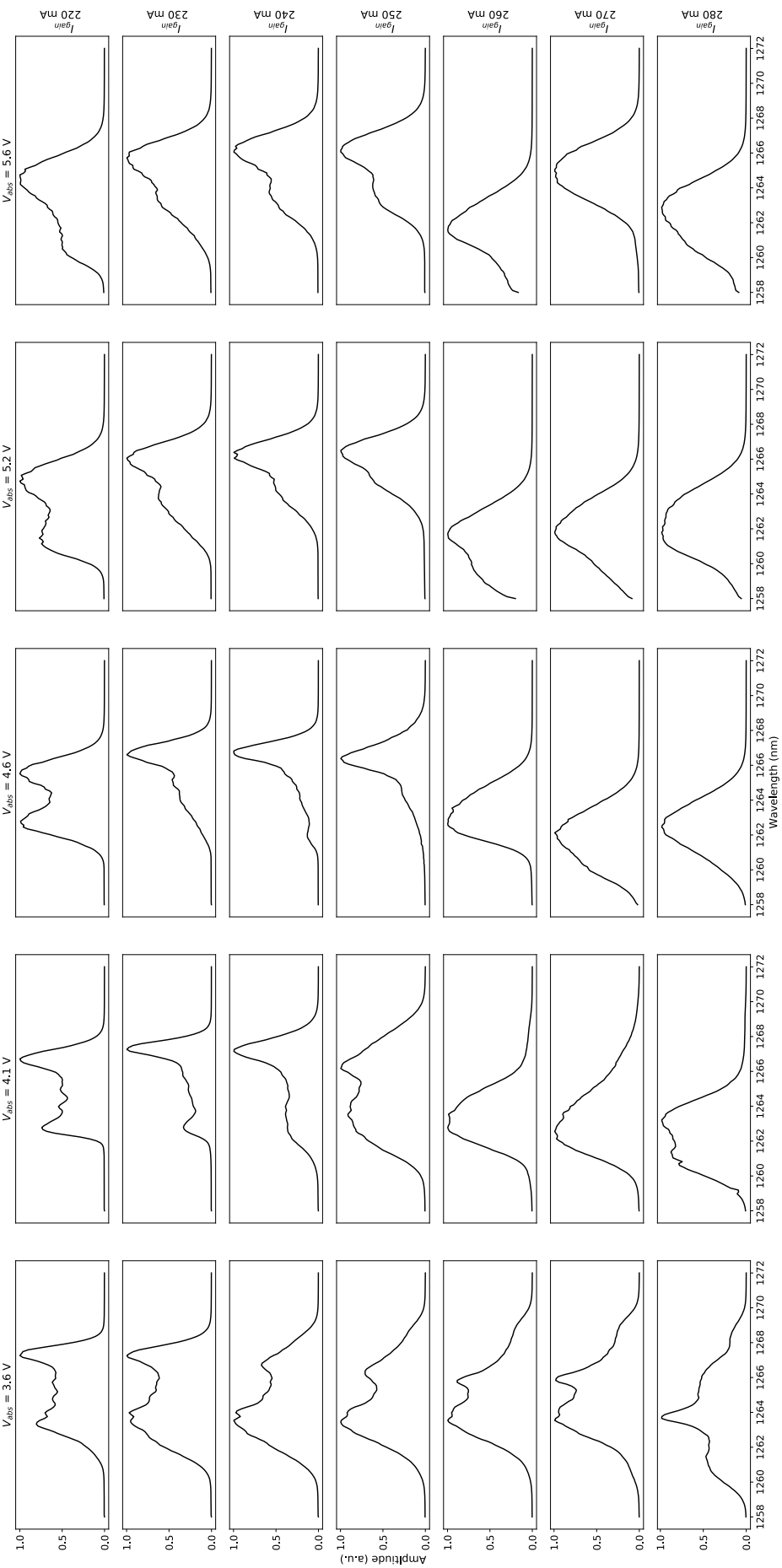


Figure 5.7: Full map of the measured fundamental optical spectrum for different values of drive current (220 mA $\leq I_{gain} \leq$ 280 mA) and reverse bias voltage (3.6 V $\leq V_{abs} \leq$ 5.6 V).

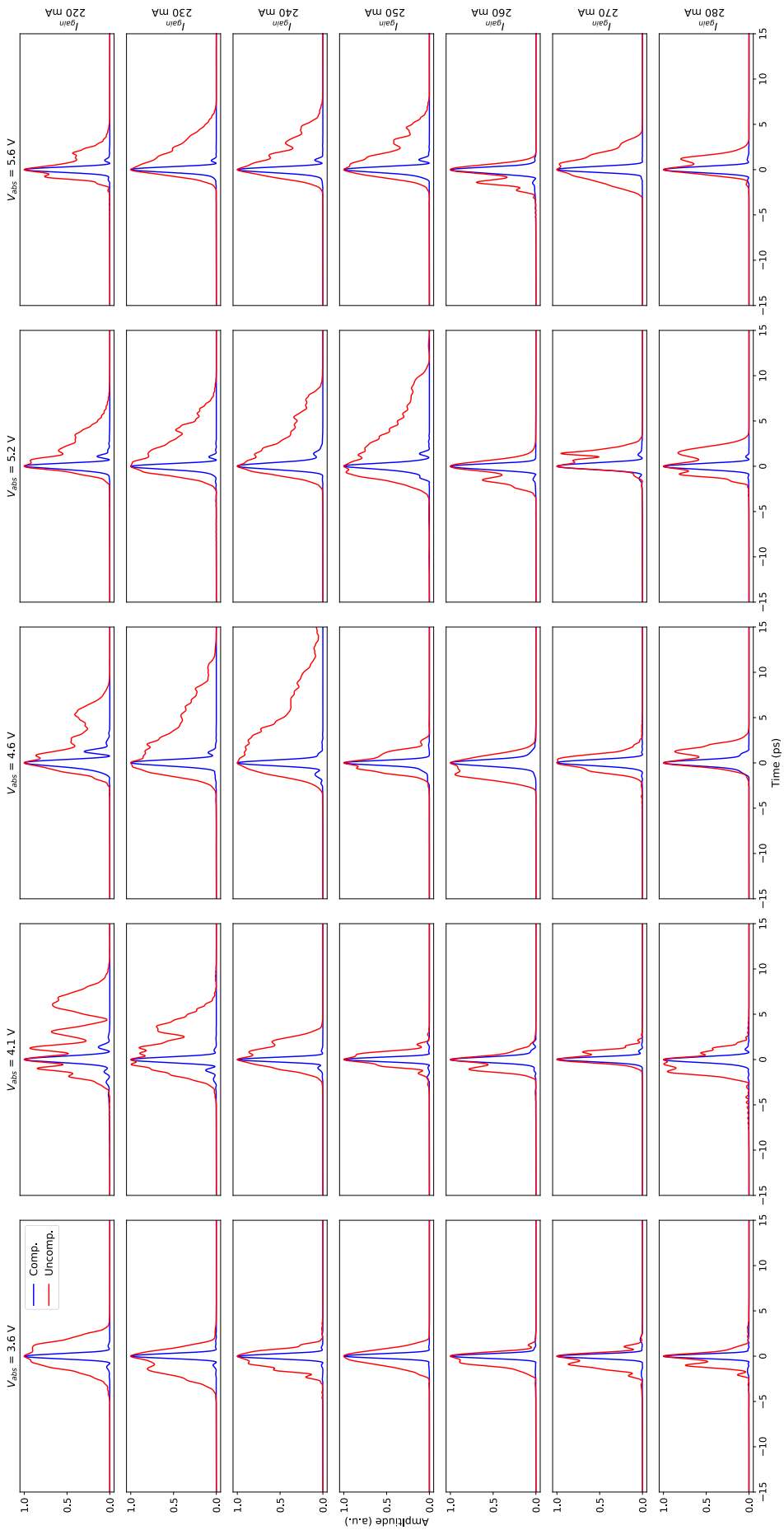


Figure 5.8: Full map of the average temporal profile of the uncompressed (red) and compressed (blue) pulses for different values of drive current (220 mA $\leq I_{gain} \leq$ 280 mA) and reverse bias voltage (3.6 V $\leq V_{abs} \leq$ 5.6 V).

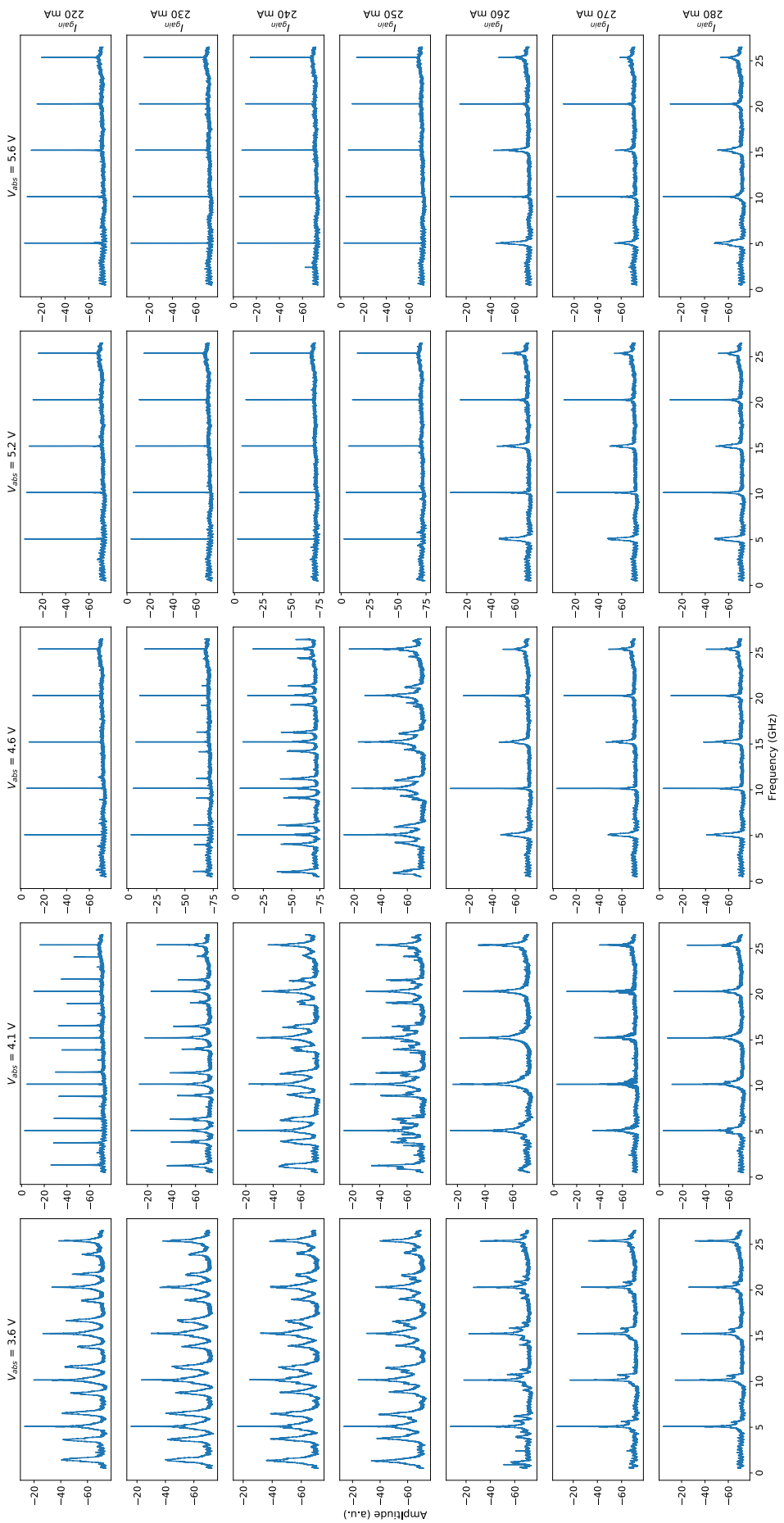


Figure 5.9: Full map of the measured RF spectrum for different values of drive current (220 mA $\leq I_{gain} \leq$ 280 mA) and reverse bias voltage (3.6 V $\leq V_{abs} \leq$ 5.6 V).

For low values of reverse bias voltage, the measured d-scan trace is not strongly affected by the drive current, and the central wavelength does not change significantly with the drive current, whereas for high values, the d-scan trace is red-shifted with an increase in drive current. The second-order dispersion tends to increase with increasing drive current and decreasing reverse bias voltage, as well as the third-order dispersion.

For reverse bias voltages between 4.6 and 5.6 V, there is a strong mode-locking transition for drive currents between 250 and 260 mA, where the d-scan trace (and, therefore, the fundamental spectrum) becomes significantly blue-shifted and the pulses become less chirped. For low values of reverse bias voltage, this mode-locking transition does not occur.

By calculating the instability metric for each measured d-scan trace, we can create a map of instabilities with the different mode-locking regimes obtained for varying driving conditions. This map can be seen in Figure 5.10.

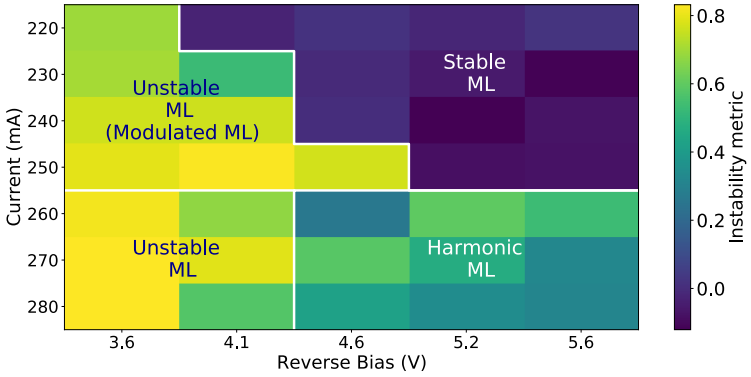


Figure 5.10: Instability metric map, together with the representation of the regions of different mode-locking regimes, obtained for the pulses from the QD laser for different values of drive current and reverse bias.

We have separated the full map of instabilities into 4 different regions: stable ML, unstable ML, unstable and modulated ML, and harmonic mode-locking (HML). The stable ML regime is obtained when the metric of instabilities is close to zero. We will discuss each of the other 3 regions in detail in the next sections.

5.6.1 Unstable ML and modulated ML

A high instability metric dictates the unstable mode-locking regime. However, in this case, two different situations occur, as shown by the RF spectra. Figure 5.11 shows the RF spectra measured for pulses driven at $V_{abs} = 3.6\,\mathrm{V}$, but with different drive currents. For the pulses driven at 240 mA, there is a main peak on the RF spectra at approximately 5

GHz. However, this peak is quite broad, and there are secondary peaks that evidence the presence of an amplitude modulation of the pulses. This strong amplitude modulation has a frequency of approximately 1.37 GHz (indicated by the frequency of the first occurring peak in the RF spectra), and could be responsible for the chirp modulation that creates the instability in the pulse train, since a change of the amplitude from pulse to pulse will lead to a change of the self-phase modulation experienced by the pulse inside the cavity, therefore changing its chirp. However, for a drive current of 270 mA, there is no strong amplitude modulation, only a broad baseline in the main RF peak (which could be indicative of amplitude and phase noise). In this situation, the mode-locking is not amplitude-modulated, and the instability is created in a different way. The RF harmonics also decay very rapidly, at a rate of approximately 10 dB per harmonic peak, which also indicates unstable mode-locking [143]. The appearance of a broad noise level on the RF spectrum due to instabilities in the pulse temporal duration has been previously predicted by Bandelow *et al.* [144].

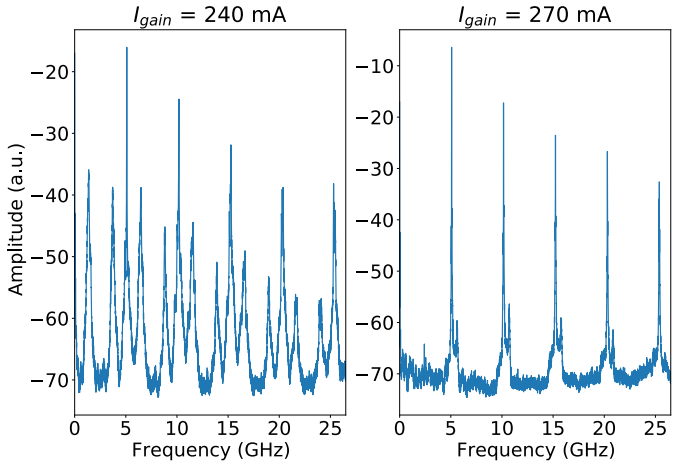


Figure 5.11: RF spectra obtained for the pulses driven at $V_{abs} = 3.6$ V and drive current of 240 mA (left) and 270 mA (right).

5.6.2 Harmonic mode-locking

Let us analyze the autocorrelation and the RF spectrum for the mode-locking transition conditions. Let us focus on the pulses obtained at different drive currents, but a fixed reverse bias voltage $V_{abs} = 5.6$ V, whose RF spectra and autocorrelation traces can be seen in Figure 5.12.

Looking at the RF spectra, we see, up to a drive current of 250 mA, a main, defined peak at approximately 5 GHz, with the subsequent harmonics having defined peaks as well. However, on the mode-locking transition, the main peak shifts to approximately

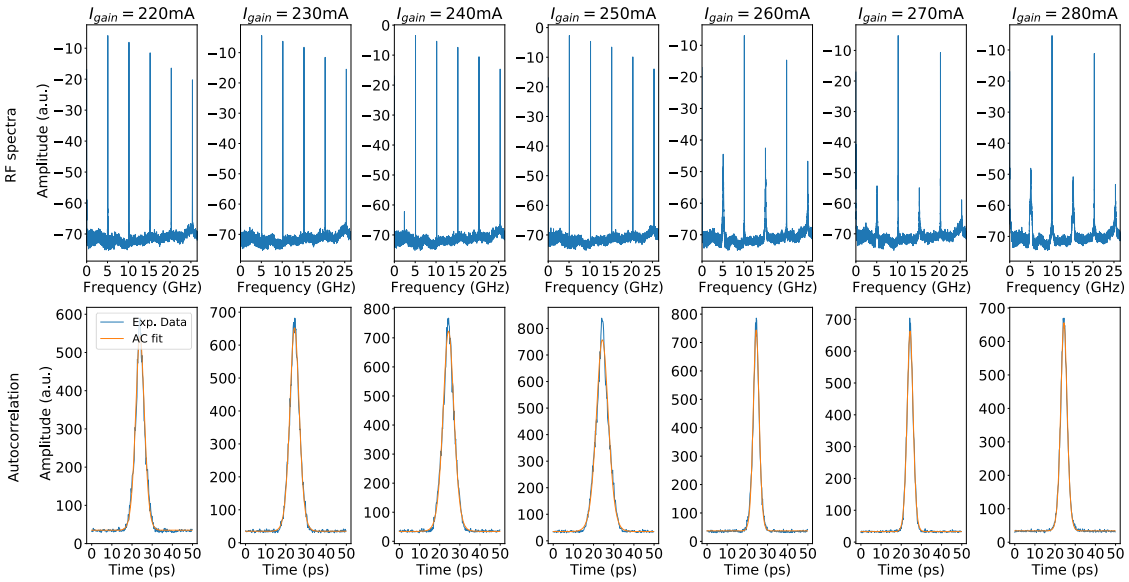


Figure 5.12: RF spectra (top row) and autocorrelation traces (bottom row) obtained for pulses driven at $V_{abs} = 5.6\,\mathrm{V}$ and different drive currents.

10 GHz, which indicates harmonic mode-locking. In this case, two pulses are traveling simultaneously inside the cavity, where the total energy is divided by these two pulses. If we measure the average power for the conditions studied in these measurements, we see that it increases with the drive current. However, since the total energy of each pulse depends on the repetition rate of the pulse train, when the laser enters the harmonic mode-locking regime the energy of each pulse actually decreases, which should decrease the effect of self-phase modulation in the gain section. As a result, both the chirp and the pulse train instabilities would also decrease, which is in good agreement with previous measurements with other types of semiconductor lasers [145, 146].

Although the RF spectra obtained for pulses in HML appear to define a stable ML, the instability metric calculated in these conditions tells a different story. In an HML regime, two pulses are traveling in the cavity simultaneously. The d-scan technique cannot distinguish one from the other, *if the two pulses are equal*.

However, if the two pulses that co-exist in the laser cavity in an HML regime have different chirps, then the situation changes. The measured d-scan trace will be a superimposition of the individual d-scan trace of each pulse. If each pulse is different, then each d-scan trace will be different (independently of the presence of timing jitter), and the measured d-scan trace will reflect this effect. To further study this effect, we have performed a simulation of a d-scan trace, resulting from pulses with a center wavelength of 1264 nm and a Fourier transform-limited FWHM of 600 nm with a pure quadratic spectral phase

corresponding to a GDD equal to $1.4\,\mathrm{ps}^2$. To this pulse, we have added a second pulse (thus simulating the HML regime) with different values of GDD. The simulations can be seen in Fig. 5.13.

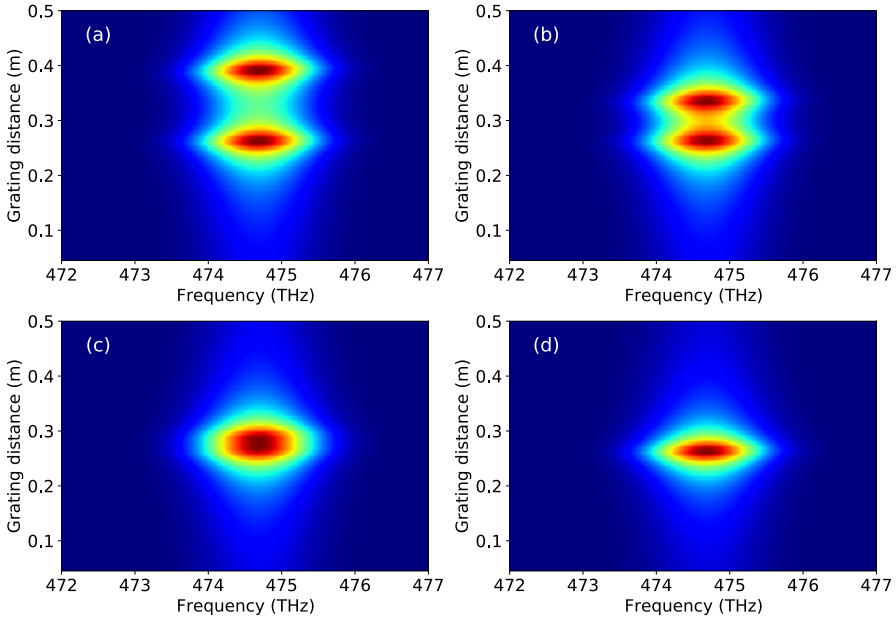


Figure 5.13: HML regime d-scan simulation, with a base pulse with $GDD = 1.4ps^2$ and another pulse with $GDD = 2.1ps^2$ (a), $GDD = 1.8ps^2$ (b) and $GDD = 1.55ps^2$ (c). Base pulse with $GDD = 1.4ps^2$ d-scan trace for comparison (d).

In the cases where the GDD difference of the two pulses is significant, we can see the superimposition of both d-scan traces, and distinguish one from the other. However, as the GDD difference gets smaller, the two d-scan traces (each corresponding to each pulse in the HML regime) start to merge. In the case of Fig. 5.13(c), the d-scan trace for each pulse is not distinguishable, but the resulting d-scan trace is broader in the dispersion axis compared to the single-pulsing d-scan trace. In this case, the broadening is strictly caused by the different chirps of each pulse in the HML regime, in which each pulse is completely stable. Therefore, with only a d-scan measurement, it is not possible to distinguish between HML where each pulse can have a different, but stable chirp, and unstable mode-locking. A secondary RF measurement has to be made to draw further conclusions regarding the stability of the mode-locking regime in these conditions.

Previous work has been done on investigating HML regimes and their stability. Bandelow *et al.* [144] were able to study HML using a Delay Differential Equation model and concluded that, at high driving currents, there is a self-starting HML regime, that is stable for a finite range of driving parameters. Experimentally, they have seen HML in a 40 GHz semiconductor mode-locked laser, and the measured RF spectrum is similar to the one

seen in Fig. 5.12 (for drive currents higher than 260 mA). Other authors were able to predict HML, namely Raghunathan *et al.* [147], who developed a nonlinear delay differential equation model for passively mode-locked semiconductor lasers. The model predicts the appearance of higher-order HML for higher reverse bias voltage. The model also predicts that the threshold drive current for HML increases with reverse bias voltage.

In 2014, Mee *et al.* [148] stimulated HML of higher order repetition rates, which was electronically induced in a multi-section device. By continuously increasing the drive current, they obtained stable ML at the fundamental repetition rate, followed by a region of unstable pulses. By further increasing the drive current, they obtained narrow pulses at double the fundamental repetition rate, followed again by a region of unstable pulse generation, which is in very good agreement with the results obtained in this thesis (particularly for $V_{abs} = 4.6\,\mathrm{V}$).

5.7. Conclusions and future work

In this section, we have applied the self-calibrating retrieval algorithm, together with our implementation of a highly-sensitive d-scan experimental setup, to successfully quantify pulse train instabilities in semiconductor laser diodes. With these measurements, we were able to investigate the influence of drive current and reverse bias on the mode-locking regime and distinguish between stable mode-locking, unstable mode-locking (with or without amplitude modulation), and harmonic mode-locking, as well as perform simulations to confirm our experimental results. Measuring a d-scan trace, applying the self-calibrating retrieval, and measuring the RF spectrum gives us enough information to distinguish between the different mode-locking regimes successfully.

An interesting approach to eliminate the pulse train instabilities in a modulated ML regime, obtained at specific driving conditions, would be to implement a (active or passive) feedback loop either on the gain section or the saturable absorber, to eliminate the amplitude modulations and enable stable mode-locking. In the passive feedback loop [149], the absorber is grounded by a high-frequency DC-block and a high-frequency $50\,\Omega$ resistor in series and connected to the voltage source by a low-pass filter (see Figure 5.14 for more details). The amplitude-modulated envelope directly induces a modulated photocurrent in the absorber section, and the DC-block eliminates the modulations.

Some variations of the active feedback loop have been implemented [150–152]. A particular case consists of an optoelectronic feedback of the amplified RF beats of the longitudinal

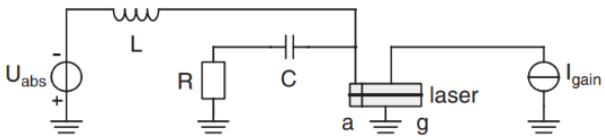


Figure 5.14: Experimental setup for the passive suppression of Q-switching. U_{abs}: voltage source. I_{gain}: DC current source. L: lowpass filter. R: resistance. C: DC-block. a, g: absorber and gain section, respectively. Reproduced from [149].

modes onto the injection current [150], causing a forced modulation of the carrier concentration and effectively reducing the modulation instabilities. A photodetector is used to measure the RF beats which, in turn, is coupled to a bias tee that modulates either the drive current or reverse bias (see Figure 5.15 for further details). In this case, the length of the feedback loop has to be carefully adjusted to achieve coincidence between optical and electrical pulses within the laser medium, employing either an electrical or optical delay line. The main conclusion is that a direct modulation of the diode current would enable control of the intracavity loss or gain modulation, which would, in turn, enable the reduction of pulse train instabilities.

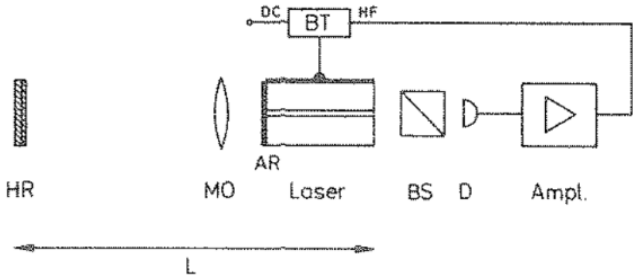


Figure 5.15: Experimental setup for the active suppresion of Q-switching. BT: Bias Tee. D: photodetector. BS: beam splitter. $Ampl.$: amplifier. Reproduced from [150].

Further investigations could be made on even higher drive currents and reverse bias, to observe higher orders of harmonic mode-locking, as well as obtain broader fundamental spectra capable of supporting even shorter transform-limited pulses. With the added knowledge of the stability of the mode-locking regime with the self-calibrating retrieval, the capability of obtaining even shorter pulses from semiconductor laser diodes is a dream that may come true in the near future.

6. Characterization of pulses amplified by semiconductor optical amplifiers

In this chapter, we will present our results regarding pulse amplification in a semiconductor optical amplifier based on quantum dots. We have studied the amplification influence on the amplified pulses' temporal shape, and studied the spectral broadening caused by the self-phase modulation in the amplification process. We have also investigated the amplification of an unstable pulse train and calculated the corresponding instability metric.

6.1. The need for pulse amplification

Laser sources that can deliver high average and peak power optical pulses are crucial for a set of applications, such as nonlinear frequency conversion [153] and nonlinear biomedical imaging, which include two-photon excited fluorescence imaging [154] and nonlinear imaging techniques based on SHG [155]. Laser sources that deliver ultrashort laser pulses with center wavelengths around $1.3\,\mu m$ are promising for this application, since they have a high penetration depth into biological tissue [156] due to decreased scattering [157] and reduced probability of photo-damage [158]. This compels the use of QD lasers as stable, high-power, and compact laser sources, ideal for these types of applications.

In the previous chapters, we have demonstrated a range of mode-locking regimes. Figure 6.1 shows the corresponding measured average power as a function of drive current and reverse bias.

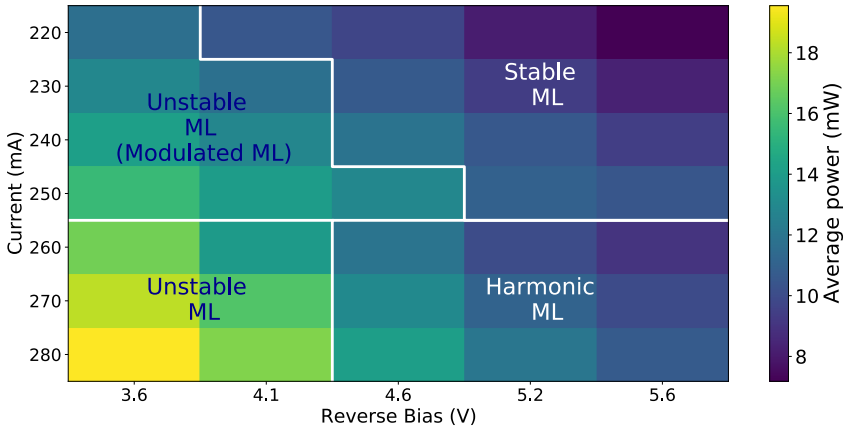


Figure 6.1: Measured average power from the QD mode-locked laser, as a function of drive current and reverse bias.

The average power of the pulse train increases with the drive current, as expected. The average output power decreases with reverse bias, due to a weaker absorption saturation in the saturable absorber [130].

For this set of driving conditions, the maximum achieved average power was approximately $19.5\,\text{mW}$, achieved in driving conditions that create unstable mode-locking. For a stable, fundamental mode-locking, the maximum average power obtained was approximately $12\,\text{mW}$ which, when compressed and taking into account the losses of the single-grating compressor, yields a very modest peak power of $1.28\,\text{W}$.

To increase the applicability of these laser sources, it is therefore necessary to amplify these pulses and fully characterize them. It is also important to understand the influence of pulse amplification on the temporal profile of the pulse since often an optical amplifier is implemented before the pulse characterization setup (and assumed to have negligible influence on the pulse temporal evolution) [159].

Thanks to technological developments driven by telecommunications, some of the most common amplification systems involve the use of Erbium-doped fiber amplifiers (EDFA), due to their high gain, low noise, and low polarization dependence, being one of the staples for pulse amplification in the C-band ($1530 - 1565\,\text{nm}$), for data communication [160]. However, their spectral bandwidth is limited, and the maintenance costs are high. EDFAs also require using a pump laser for pulse amplification, which increases the cost of these systems. In the O-band ($1260 - 1360\,\text{nm}$), semiconductor optical amplifiers (SOAs) are highly efficient, with the advantage of being electrically pumped, which allows for easy integration in complex systems and enhancing system flexibility. Compared to EDFAs, SOAs offer low-cost mass production, reduced power consumption, and a smaller footprint, at the small cost of a slightly increased noise [161].

6.2. Semiconductor Optical Amplifiers

A semiconductor optical amplifier consists of an optical amplifier based on a semiconductor gain medium *, and was first implemented during the 1980s, having been strongly investigated in that period [162–168] and used as integrable on-chip amplifiers within optical transmitters and receivers. They are extremely similar to semiconductor laser diodes, but their facets are tilted and have anti-reflection coatings to eliminate back reflections into the amplifier, thus preventing optical feedback and lasing and acting simply as a gain

*Who would've thought?

medium in which light is amplified by stimulated emission. The gain dynamics are generally similar to that of the gain section of passively mode-locked laser diodes, which are strongly affected by refractive index changes that cause self-phase modulation.

A SOA works in two different regimes, depending on the input signal power and its influence on the gain dynamics. In the unsaturated regime, the input signal power is not high enough to influence the gain, and therefore the output scales linearly with the input power. The gain starts to saturate above a certain input power threshold, decreasing as the input power increases, and the output power tends to a maximum, saturated value. However, in a pulsed light amplification process, the peak power is typically much higher than the average power, and the signal gain may change inside the pulse itself, which can cause an asymmetrical gain curve in the time domain, where the leading edge experiences a higher gain than the trailing edge.

SOAs have been widely used for semiconductor laser pulse amplification in recent years. In particular, QD-based SOAs show ultrafast gain recovery dynamics [90, 169, 170], an enhanced linewidth enhancement factor [171, 172] and have been intensively investigated over the past few years for their pattern-free amplification [173, 174] and wavelength conversion [175]. QD SOAs have been used to amplify pulses at $1.26\,\mu m$, either from an external cavity QD laser [176], achieving 16 ps pulses with 26 W of peak power, or from a tapered InAs/InGaAs QD laser [177], achieving 1.37 ps pulses with a peak power up to 42 W. In both cases, the amplified pulses were measured using second-harmonic autocorrelation, which does not resolve the full temporal profile of the amplified pulses. Romstad *et al.* [178] have studied the propagation of 175 fs, $1.53\,\mu m$, 300 kHz pulses from an optical parametric amplifier through a bulk InGaAsP-InP SOA using cross-frequency-resolved optical gating (XFROG), a variation of the FROG technique where the pulse to be measured is correlated with a strong reference pulse. They have observed effects from pulse narrowing to pulse breakup. Recently, Schmeckebier *et al.* [179] used the FROG technique to study the gain dynamics of QD SOAs when boosting pulses from a hybrid mode-locked QD laser. The authors have investigated the evolution of the pulses' duration and chirp with the input power and amplification current, but no trend was observed.

To the best of our knowledge, no investigation of pulse compression capability after amplification using SOAs (particularly QD SOAs) has been made so far. Also, for techniques

such as Chirped Pulse Amplification (CPA) [180], where the pulse is highly-chirped before the amplification process, having full control of the temporal profile of the pulses is crucial for an efficient pulse amplification. The d-scan technique offers this capability: it allows measuring the pulses prior to the amplification process and changing the pulses' chirp and, therefore, the pulse shape (within the range of dispersion of the used compressor). It also offers the built-in compression and characterization of the amplified pulses, allowing to compress the amplified pulses to near the transform-limit duration. The use of the self-calibrating retrieval algorithm to measure the instability metric of unstable pulses allows us to study the amplification dynamics on unstable pulse trains which, to the best of our knowledge, has not been done so far.

In this chapter, we will present our results regarding the amplification of laser pulses in a QD SOA, and the evolution of the temporal profile of the amplified pulses (both stable and unstable) with the amplification current using the d-scan technique. We hope that these results will provide further insights into the amplification process of QD SOAs, and using their high nonlinearities in our favor, namely for spectral broadening through SPM.

6.3. Experimental setup

The experimental setup used in this section can be seen in Figure 6.2. The output of the QD laser follows through the same isolator used throughout the measurements presented in the previous chapters but is then fiber-coupled, using a polarization-maintaining (PM) fiber, to a 3-paddle fiber polarization controller, to maximize the amplification efficiency in the following semiconductor optical amplifier. The output of the SOA is then coupled to free-space, to allow measuring the pulses with the developed d-scan setup.

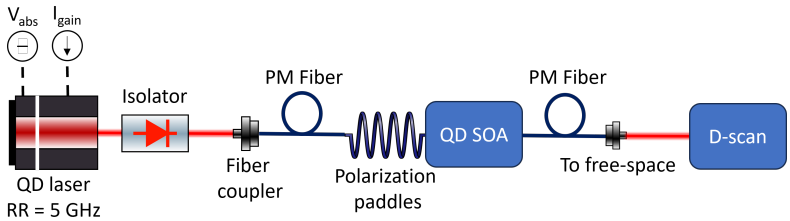


Figure 6.2: Setup for studying the amplification process using a semiconductor optical amplifier. The polarization paddles are used to match the polarization of the laser to the one that provides the higher amplification efficiency.

The d-scan measurement without amplification was made by bypassing the amplifier completely, using the same beamline as described in chapter 3. This could mean that the measurement conditions were different for the non-amplified and the amplified pulses,

namely regarding the total GDD of the pulse. To investigate this, we have calculated the total GDD introduced by the chromatic dispersion of the fiber system used in the amplification experimental setup, given by:

$$GDD(\lambda) = L\frac{\lambda^3}{2\pi c^2}\frac{\partial^2 n(\lambda)}{\partial \lambda^2} \tag{6.1}$$

where L is the total length of the fibers, and $n(\lambda)$ is the wavelength-dependent refractive index. Assuming that we have fused silica single-mode fibers with a total length of $10\,\text{m}$ and $\lambda = 1265\,\text{nm}$, we estimate a total GDD introduced by chromatic dispersion equal to $0.009\,\text{ps}^2$. Together with the dispersion introduced by the SOA (assumed to be that of bulk GaAs [126], mentioned in chapter 4, which is not exact but serves as an estimation of orders of magnitude), we get a total GDD equal to $0.017\,\text{ps}^2$, which is negligible compared to the GDD of the measured pulses. We did not calculate the waveguide dispersion of the used fibers, since we do not have access to its dispersion parameter, but we have assumed that it is negligible.

The used SOA is commercially available through Innolume (SOA-1250-110-YY-27dB), based on an InAs/InGaAs quantum dot chip, providing a broad gain curve (from 1190 to 1310 nm). The measured amplified spontaneous emission (ASE) curves for different values of drive current and operating temperature can be seen in Figure 6.3.

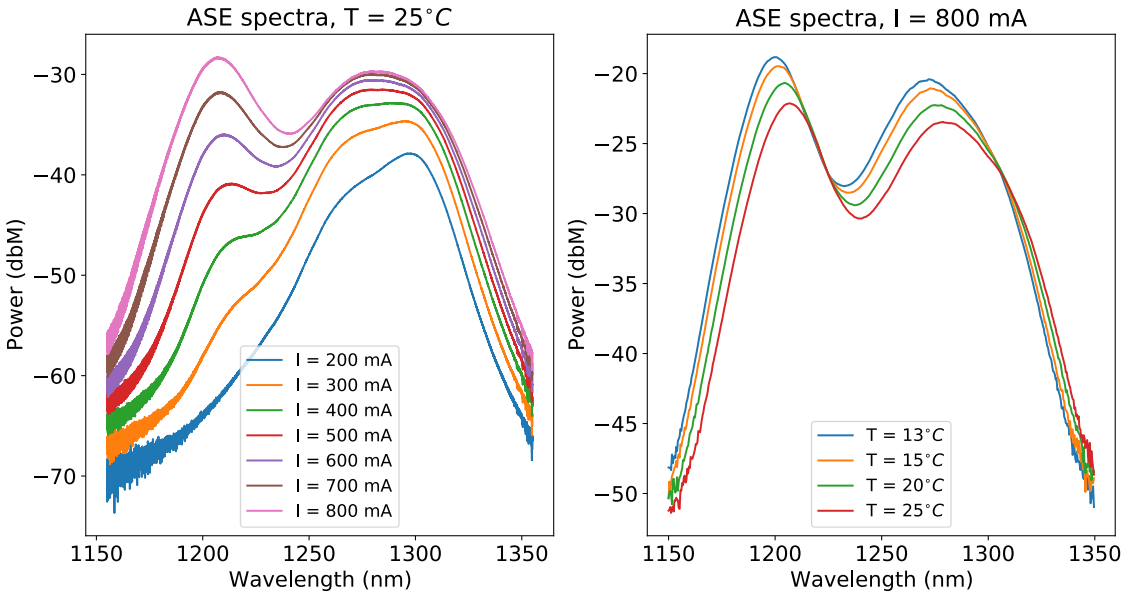


Figure 6.3: Amplified spontaneous emission (ASE) spectrum of the QD SOA, for fixed operating temperature and variable drive current (left), and fixed drive current and variable operating temperature (right).

Both the driving current and the operation temperature have a strong influence on the ASE spectrum (related to the gain curve) of the SOA. Decreasing the operating temperature leads to a strong overall blue-shift of the ASE spectrum and a general gain increase. Increasing the driving current leads to an increase in the optical power of the ASE curve and, for high values of driving current, to the appearance of the excited state emission (seen as the appearance of a broad ASE peak around 1200 nm, corresponding to the excited state of the QDs used in the SOA). Throughout the rest of this chapter, the temperature of the QD SOA was set to $25°C$.

As an example, Figure 6.4 shows the ASE spectrum of the QD SOA driven at $800\,\text{mA}$ and set at $25°C$, together with the input and output spectra of the amplified QD laser pulses driven at a drive current of $240\,\text{mA}$ and a reverse bias of $5.2\,\text{V}$.

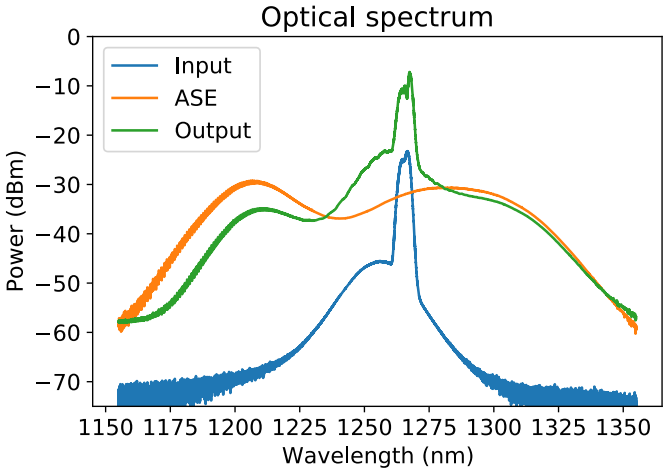


Figure 6.4: Input (blue), output (green) and ASE (orange) spectra for pulses with $I_{gain} = 240\,\text{mA}$ and $V_{abs} = 5.2\,\text{V}$, amplified in the SOA with an amplification current of 800 mA.

6.4. Amplification of stable pulse trains

To study the efficiency and the behavior of the SOA used throughout this experiment, we have amplified pulses from the QD laser studied in the previous chapter in three different driving conditions, whose results will be analysed in detail in the next sections.

6.4.1 Case 1

For this first investigation, we applied a drive current $I_{gain} = 240\,\text{mA}$ and a reverse bias $V_{abs} = 5.2\,\text{V}$ to the QD laser. To study the evolution of the temporal profile of the pulses with the amplification process, we have measured d-scan traces for the pulses amplified by the SOA and compared them to the ones obtained for non-amplified pulses. For

these measurements, in the single-grating compressor, we have used the grating with 830 lines/mm and a blaze wavelength of $1.2\,\mu m$. The d-scan traces measured without amplification and with amplification at 200, 500, and 800 mA of amplification current can be seen in Figure 6.5.

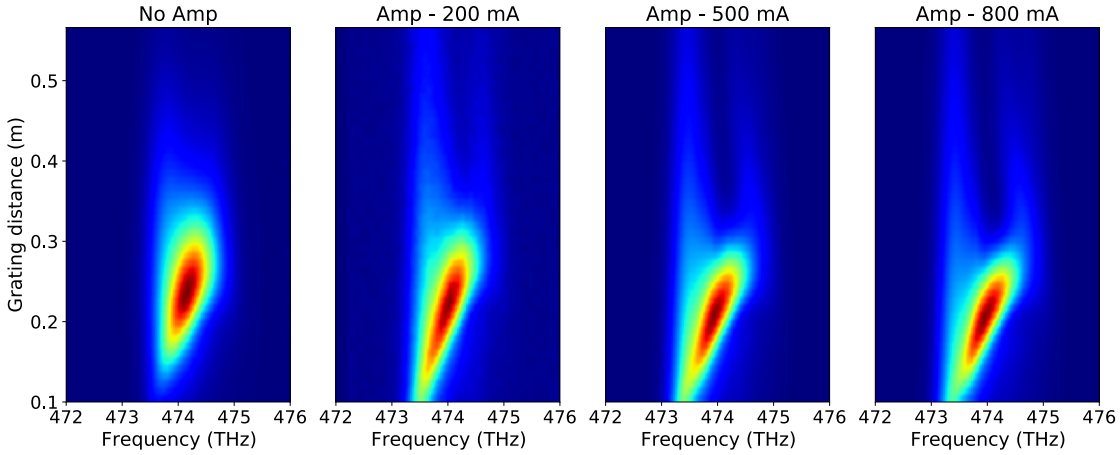


Figure 6.5: From left to right: measured d-scan trace for pulses from the QD laser driven at $I_{gain} = 240\,\text{mA}$ and $V_{abs} = 5.2\,\text{V}$ without amplification; and with amplification with the SOA driving current equal to 200; 500; and 800 mA.

There is a clear difference between the d-scan traces obtained before amplification and after amplification. The overall shape of the d-scan trace changes, where the small features observed at higher dispersion are more prominent after amplification. This can be explained by the non-linearity of the SOA gain (lower power features are further amplified). As an example, the retrieval of the d-scan trace obtained for pulses driven at $I_{gain} = 240\,\text{mA}$ and $V_{abs} = 5.2\,\text{V}$, amplified with the SOA driven at a current of 800 mA can be seen in Figure 6.6.

The measured d-scan error for this measurement is equal to $3.8\,\%$, and the retrieved d-scan trace is in excellent agreement with the measured one. The d-scan errors obtained for the pulses in these driving conditions with different amplification drive currents can be seen in Table 6.1.

I_{amp}	No amp.	200 mA	300 mA	400 mA	500 mA	600 mA	700 mA	800 mA
G error	11.6%	7.7%	3.8%	4.5%	3.4%	4.2%	5.2%	3.8%

Table 6.1: G error obtained for the retrieved d-scan traces for the amplified pulses.

The G error is very low for drive currents higher than $200\,\text{mA}$. However, the d-scan error is relatively high for the pulses obtained with no amplification (i.e., directly from the QD laser), even though similar measurements have been made previously with these driving conditions. Since the setup has been changed multiple times throughout this work

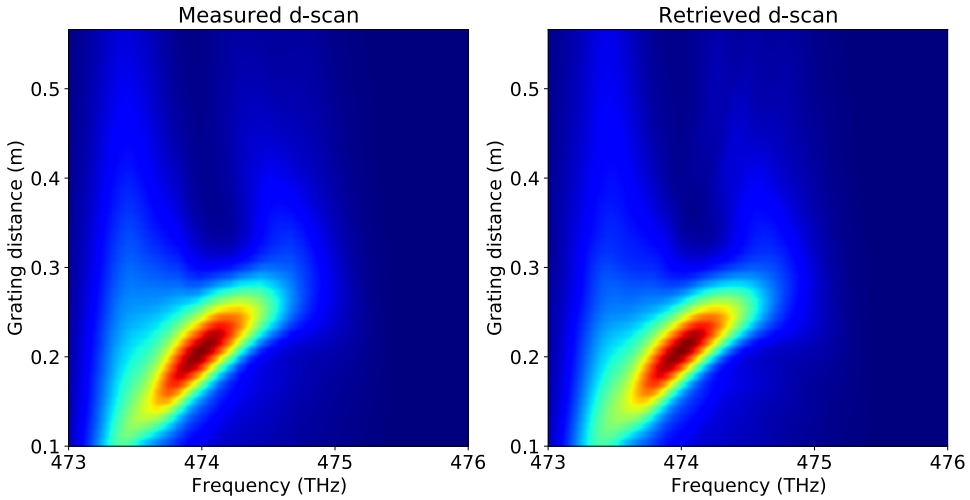


Figure 6.6: Measured and retrieved d-scan trace for $I_{gain} = 240\,\text{mA}$ and $V_{abs} = 5.2\,\text{V}$, amplified with the SOA driven at 800 mA.

(namely grating changes and aligning the setup to measure either the pulses directly from the QD laser or the ones amplified by the SOA), we have noticed a lower SNR on these measurements, which can explain the relatively high d-scan error. Nevertheless, the retrieved d-scan traces for all amplification currents are in good agreement with their measured counterparts, and it is worth noting that increasing the amplification current (therefore increasing the average power of the measured pulses) increases the SNR of the d-scan trace, which leads to an overall reduction of the G error.

The retrieved spectral power and phase, as well as the temporal profiles obtained for the QD laser pulses driven at $I_{gain} = 240\,\text{mA}$ and $V_{abs} = 5.2\,\text{V}$ and further amplified with the SOA can be seen in Figure 6.7.

If we analyze the retrieved spectral power, we see that the amplification process causes a red-shift, together with spectral broadening, that increases with the SOA drive current, caused by the initial chirp of the optical pulse. When entering the SOA, the longer wavelength components of the optical pulse will enter and, therefore, be amplified first in the SOA [166, 167]. This will cause a gain saturation, reducing the amplification efficiency for the shorter wavelength components. An interesting feature occurs if we analyze the uncompressed temporal profile of the laser pulses. Although the pulse variations are not significant when changing the amplification drive current, the amplification process actually creates shorter pulses directly after the SOA (as can be seen in the bottom left graphic of Figure 6.7). This can be explained if we take a closer look at the effects of self-phase modulation in SOAs [167].

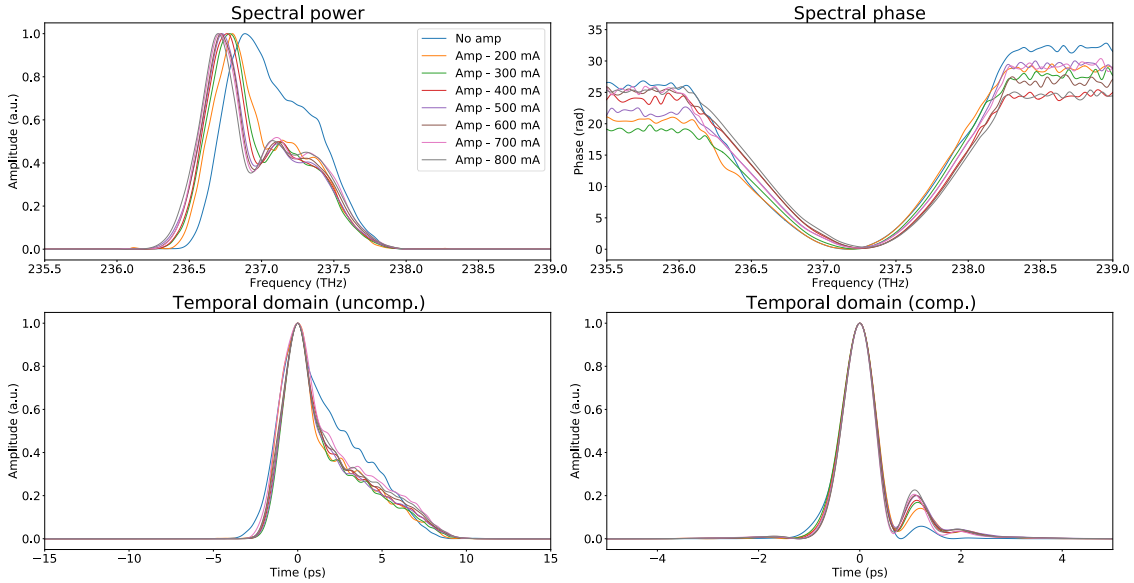


Figure 6.7: Retrieved spectral power (top left) and phase (top right), as well as the uncompressed (bottom left) and compressed (bottom right) temporal profiles for the pulses at $I_{gain} = 240$ mA and $V_{abs} = 5.2$ V, amplified with the SOA driven at different amplification currents.

The parameter α_{LEF}, the linewidth enhancement factor, is introduced into the equations that are used to study the amplification process to reflect the refractive-index changes caused by carrier density variations due to gain saturation. This parameter is responsible, in the amplification process, for simulating self-phase modulation. There are no spectral or temporal distortions when the amplifier is being operated below saturation. However, for energy values close to saturation, the self-phase modulation plays a key role in pulse amplification [166]. In this case, a red-shift of the spectrum is visible, and the optical spectrum becomes broader. Pulse distortions happen because the leading edge of the pulse saturates the amplifier and reduces the gain available for the trailing edge, which was previously seen in SOAs [181] and other type of amplifiers [182–184]. Depending on the input pulse shape [165] (and particularly if there is a positive chirp imparted on the input pulse), pulse compression can happen in the amplification process [185]. It is also interesting that, regarding the compressed pulse, the amplification process increases the power of the post-pulse, leading to a higher secondary peak. If we analyze the temporal chirp of both the non-amplified and the amplified pulses, we see no clear trend regarding the amplification process (see Figure 6.8), as previously concluded by Schmeckebier *et al.* [179].

If we calculate the peak power obtained for each amplification current, we get the results from Figure 6.9.

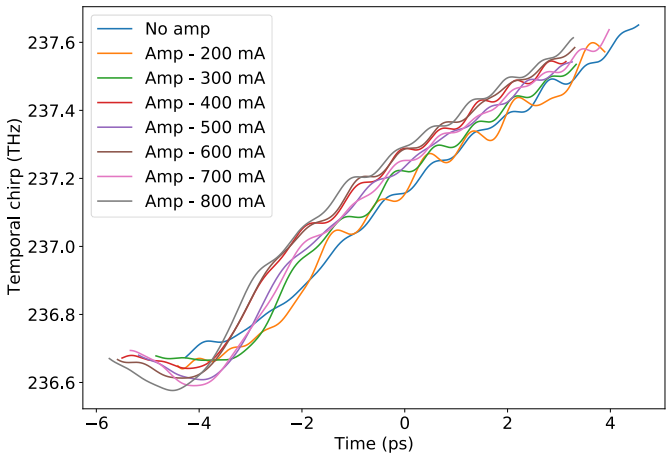


Figure 6.8: Temporal chirp of the pulses driven at $I_{gain} = 240\,\text{mA}$ and $V_{abs} = 5.2\,\text{V}$, with and without amplification using the SOA at different amplification currents.

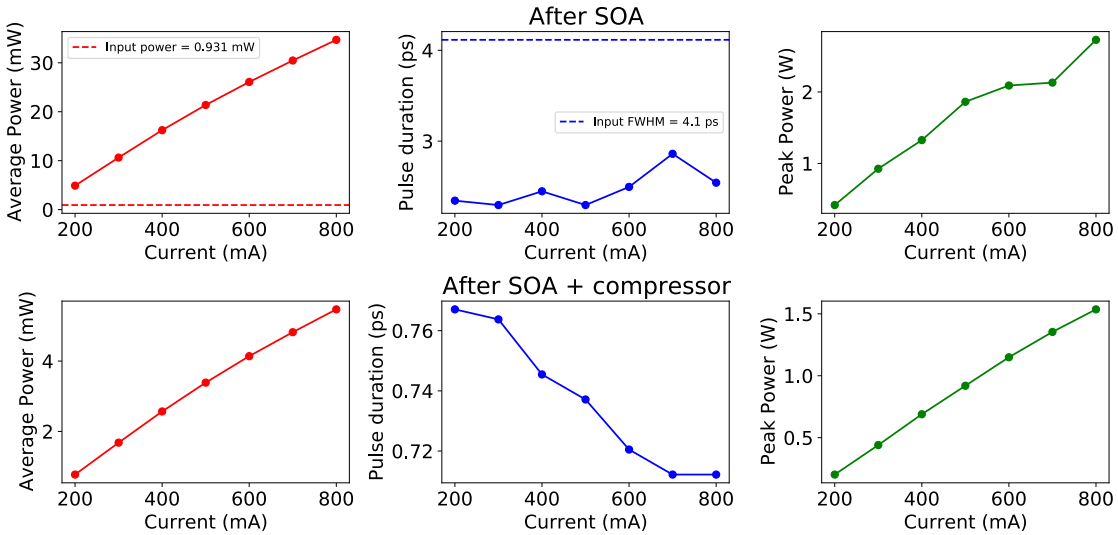


Figure 6.9: Average power (red), pulse duration (blue), and peak power (green) of the pulses obtained directly after the SOA (top row) and after the SOA + single-grating compressor (bottom row) for the pulses driven at $I_{gain} = 240\,\text{mA}$ and $V_{abs} = 5.2\,\text{V}$.

We can see that the pulse duration decreases, both for the uncompressed pulse (which was previously explained) and for the compressed pulses (which can be explained by the spectral broadening caused by the SOA, which decreases the minimum obtainable pulse width). Remarkably, we can have spectral broadening due to self-phase modulation at relatively low optical powers which is already sufficient to reduce the minimum obtainable pulse width significantly [167].

The output power of the amplified QD laser increases with the current provided to the SOA, as expected. It is worth mentioning that the input power coupled to the SOA is equal to 0.931 mW, leading to an optical gain equal to 15.7 dB at 800 mA of driving current.

6.4.2 Case 2

As another example, we present the retrieved spectral power and phase, as well as the temporal profiles (both compressed and uncompressed) of the pulses driven at $I_{gain} = 220\,\text{mA}$ and $V_{abs} = 4.6\,\text{V}$ and amplified in the SOA in Figure 6.10. The grating used in the single-grating compressor was the one with 830 lines/mm and a blaze wavelength of $1.2\,\mu m$.

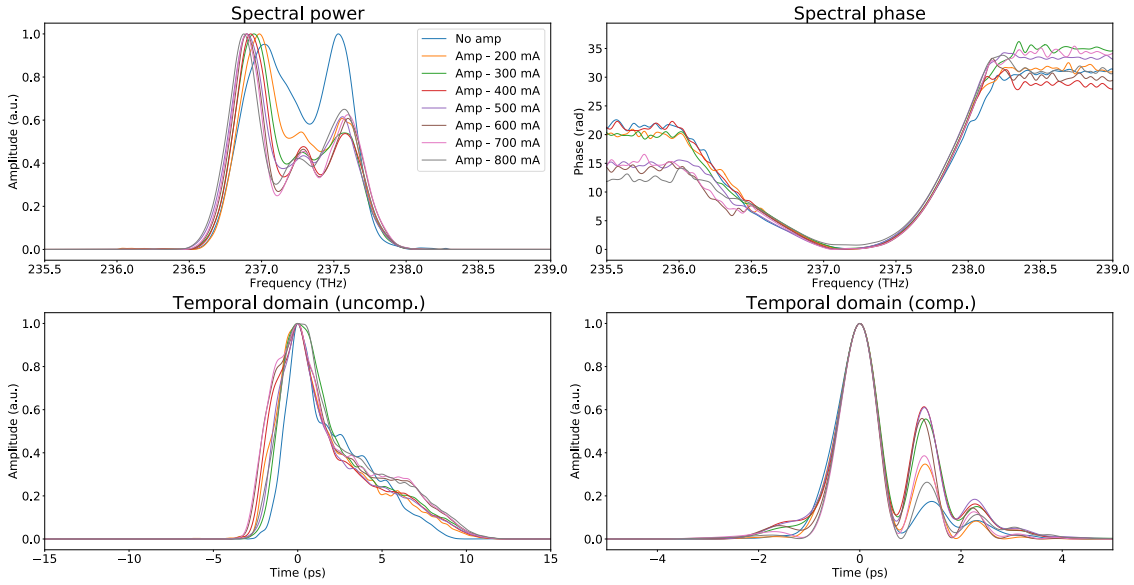


Figure 6.10: Retrieved spectral power (top left) and phase (top right), as well as the uncompressed (bottom left) and compressed (bottom right) temporal profiles for the pulses at $I_{gain} = 220\,\text{mA}$ and $V_{abs} = 4.6\,\text{V}$, amplified with the SOA driven at different amplification currents.

The optical spectrum of the amplified spectrum behaves the same way, with a red-shift and spectral broadening that increases with the amplification current. In the temporal domain, however, the evolution of the temporal profile of the amplified pulses follows a different trend. In this case, regarding the uncompressed temporal profile, the main peak of the pulse becomes stretched. For the compressed pulses, we see that increasing the amplification current up to $500\,\text{mA}$ leads to a relative increase in the intensity of the post-pulse compared to the main pulse. However, as the amplification current increases even further, this effect is reversed. The evolution of the temporal chirp with the amplification current can be seen in Figure 6.11. As in the previous case, no trend is observed.

The output average and peak power, together with the temporal duration of both the compressed and uncompressed pulses, can be seen in Figure 6.12. We see that the pulse

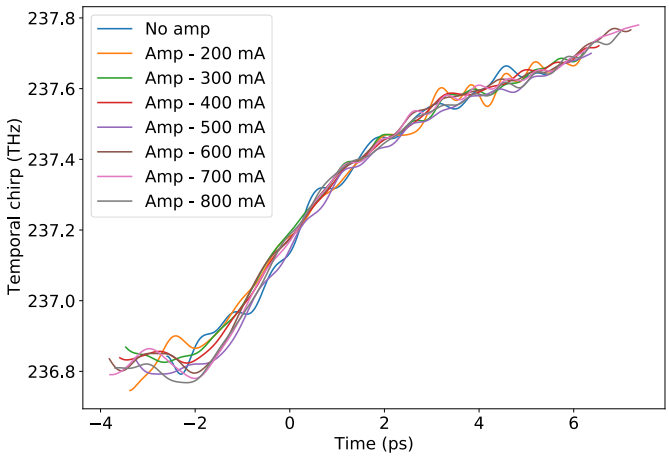


Figure 6.11: Temporal chirp of the pulses driven at $I_{gain} = 220\,\text{mA}$ and $V_{abs} = 4.6\,\text{V}$, with and without amplification using the SOA at different amplification currents.

duration for the uncompressed pulse increases, but once again due to the spectral broadening, the obtainable pulse duration after the compressor decreases with the amplification current, allowing an increase in the pulse's peak power.

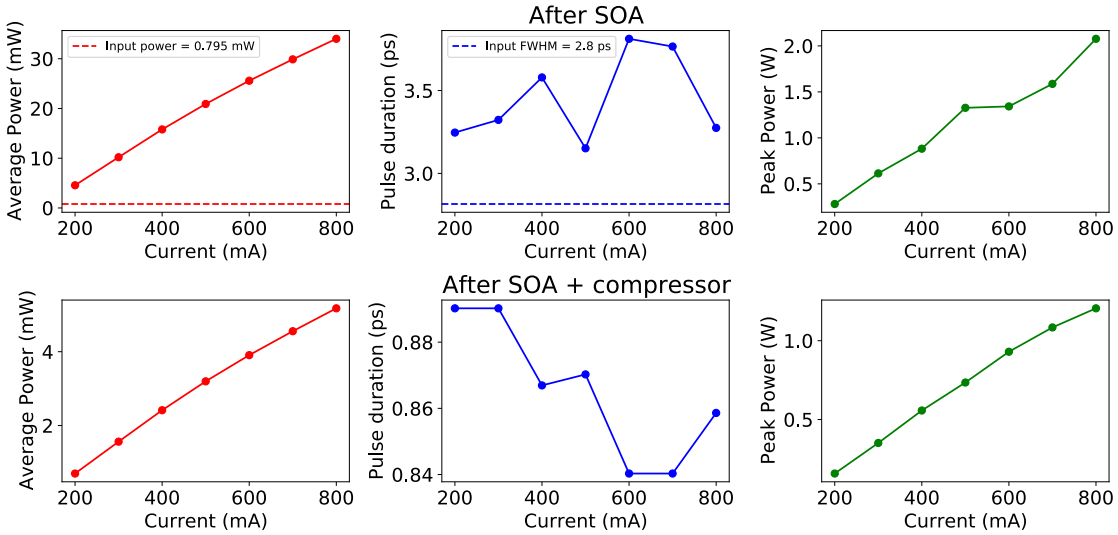


Figure 6.12: Average power (red), pulse duration (blue), and peak power (green) of the pulses obtained directly after the SOA (top row) and after the SOA + single-grating compressor (bottom row) for the pulses driven at $I_{gain} = 220\,\text{mA}$ and $V_{abs} = 4.6\,\text{V}$.

6.4.3 Case 3

As a final example, we present the retrieved spectral power and phase, as well as the temporal profiles (both compressed and uncompressed) of the pulses driven at $I_{gain} = 230\,\text{mA}$ and $V_{abs} = 5.6\,\text{V}$ and amplified in the SOA in Figure 6.13. The grating used in the single-grating compressor was the one with 600 lines/mm and a blaze wavelength of $1.25\,\mu m$.

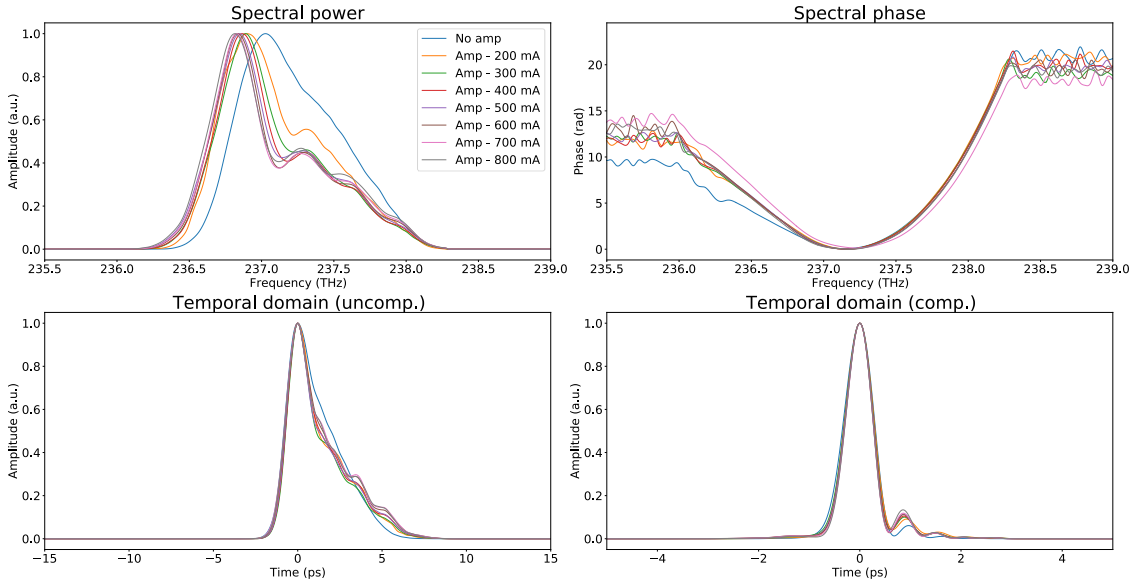


Figure 6.13: Retrieved spectral power (top left) and phase (top right), as well as the uncompressed (bottom left) and compressed (bottom right) temporal profiles for the pulses at $I_{gain} = 230\,\text{mA}$ and $V_{abs} = 5.6\,\text{V}$, amplified with the SOA driven at different amplification currents.

The spectral power evolves similarly to the previous measurements, with a red-shift and an overall spectral broadening that increases with the amplification current. An overall reduction of the temporal duration of the uncompressed pulse can be seen with the amplification process, as well as the appearance of a trailing edge modulation. This could be caused by the appearance of a spectral modulation on the blue side of the spectral power, which is strongly correlated to the trailing edge of the pulse due to its strong linear chirp.

Regarding the compressed pulse, we see that the post-pulse gets more intense with the amplification current, as seen in the previous measurements. As in the previous cases, the temporal chirp does not change significantly with the amplification current, as shown in Figure 6.14.

The output average and peak power, together with the temporal duration of both the compressed and uncompressed pulses, can be seen in Figure 6.15.

Once again, we can see that, due to the spectral broadening caused by SPM, the pulse duration after compression decreases with the amplification current. For these driving conditions, we have obtained pulses as short as $580\,\text{fs}$.

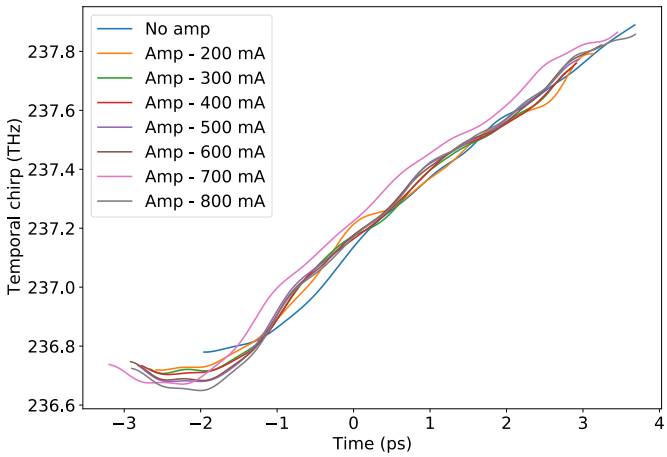


Figure 6.14: Temporal chirp of the pulses driven at $I_{gain} = 230\,\text{mA}$ and $V_{abs} = 5.6\,\text{V}$, with and without amplification using the SOA at different amplification currents.

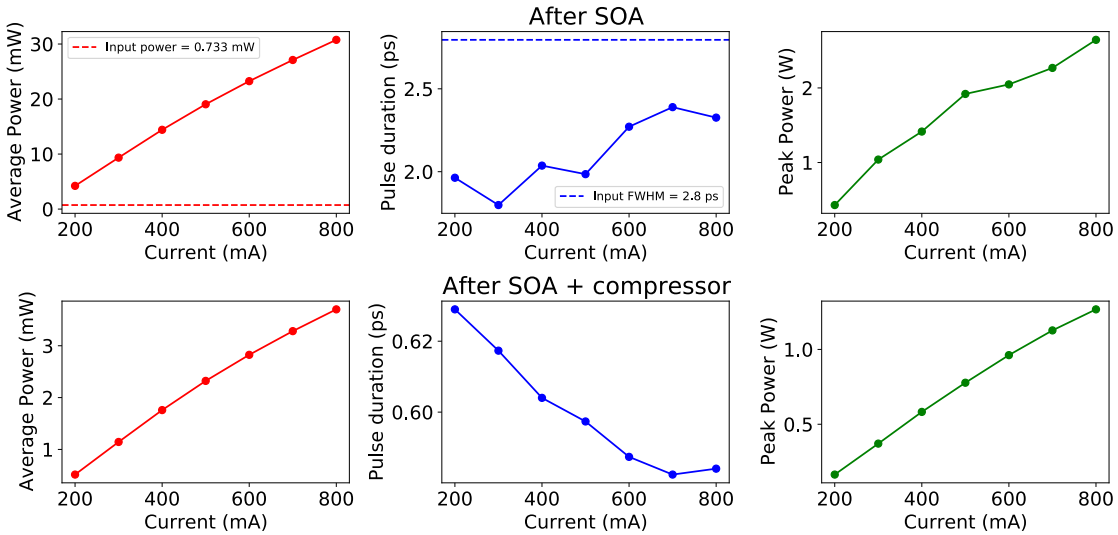


Figure 6.15: Average power (red), pulse duration (blue), and peak power (green) of the pulses obtained directly after the SOA (top row) and after the SOA + single-grating compressor (bottom row) for the pulses driven at $I_{gain} = 230\,\text{mA}$ and $V_{abs} = 5.6\,\text{V}$.

6.5. Amplification of unstable pulse trains

We have also studied the influence of the SOA on the amplification of an unstable pulse train, obtained by driving the QD laser at $I_{gain} = 230\,\text{mA}$ and $V_{abs} = 3.6\,\text{V}$. Let us first analyze the obtained output power and optical spectrum, whose results can be seen in Figure 6.16.

The output optical power increases as expected, as seen in previous examples of stable pulses. However, regarding the output optical spectrum, we see a spectral broadening that increases with the amplification drive current, as expected, but the evolution of the spectral shape is different compared to the evolution of stable pulses. The red-shift of

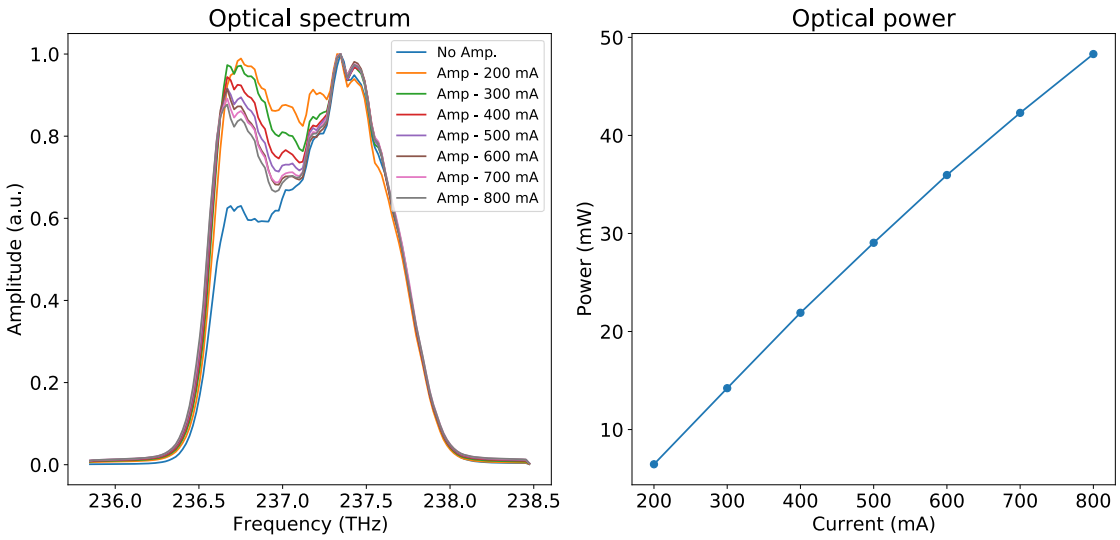


Figure 6.16: Left: Evolution of the amplified optical spectrum from the pulses driven at $I_{gain} = 230\,\text{mA}$ and $V_{abs} = 3.6\,\text{V}$, amplified in the SOA with varying amplification currents. Right: evolution of the optical power of the amplified pulses as a function of the SOA drive current. The blue line serves as a guide for the eyes.

the peak wavelength is not visible, but the spectral broadening tends to the longer wavelengths (lower frequencies). A possible explanation for this difference is the fact that the measured fundamental spectrum is an average of the fundamental spectrum of each unstable pulse, and each pulse is amplified individually. Therefore, the effect of gain saturation occurs in different frequency points depending on the input pulse, and the overall red-shift is not visible.

To study the evolution of the pulse train instabilities with the amplification process, we measured d-scan traces of both the amplified and the non-amplified unstable pulses. We have applied the self-calibrating retrieval algorithm to these measurements and studied the influence of the amplification current in the instability metric. The self-calibrating retrieval algorithm, as well as all the self-calibrating retrievals performed in these measurements, were done by Dr. Benjamín Alonso, in collaboration with the University of Salamanca. The retrievals can be seen in Figure 6.17.

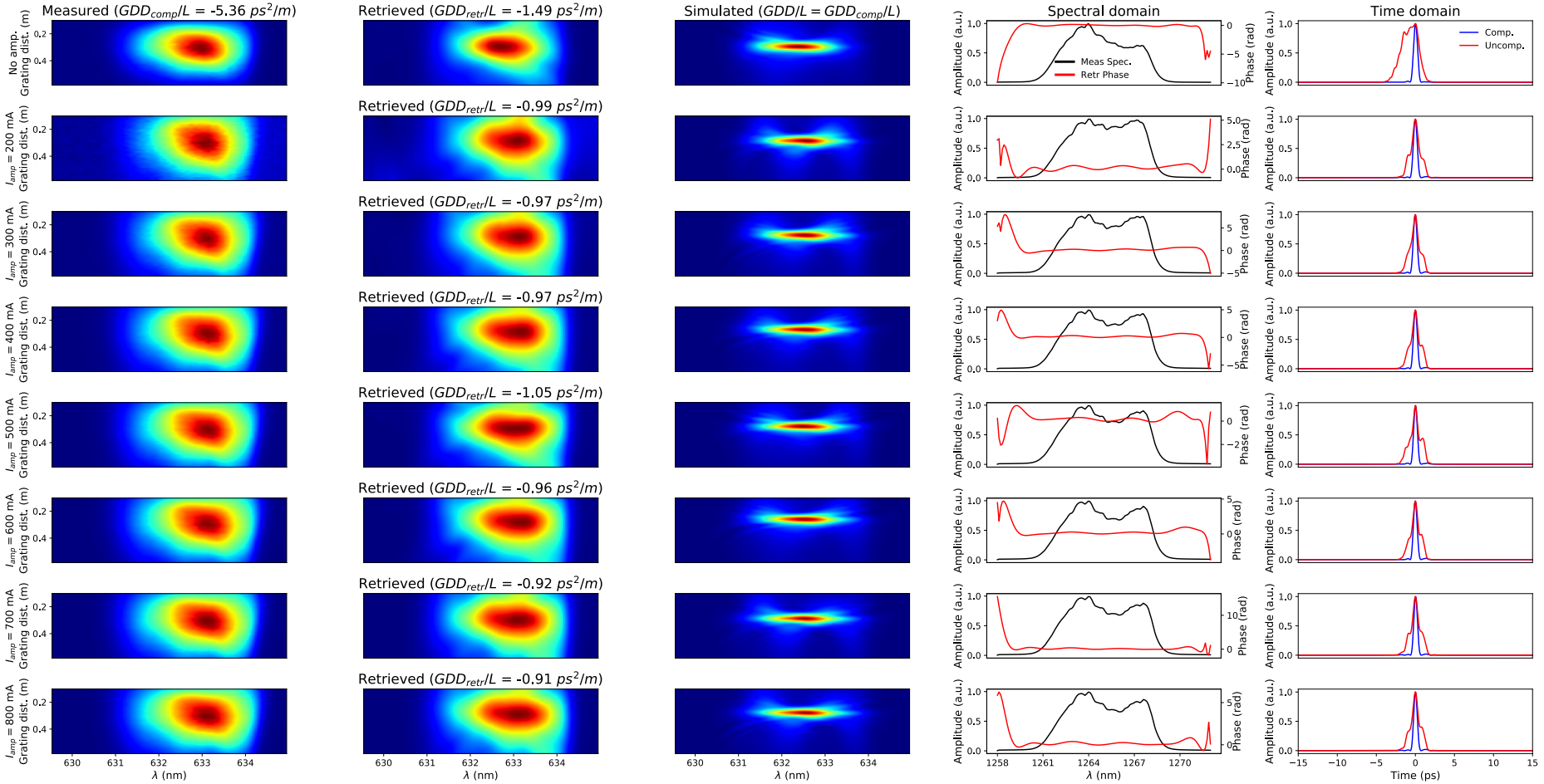


Figure 6.17: Experimental measurements for the amplification of an unstable pulse train, driven at $I_{gain} = 230$ mA and $V_{abs} = 3.6$ V. First column: measured d-scans for an amplification drive current increasing from 0 mA to 800 mA. Second column: retrieved d-scan traces using the self-calibrating algorithm. Third column: d-scan trace simulation using the retrieved spectral phase, the measured spectral power, and the dispersion imparted by the compressor, for comparison. Fourth column: measured spectral power (black) and retrieved spectral phase (red) for the compressed pulse. Fifth column: retrieved average pulse in the time domain, both compressed (blue) and uncompressed (red).

The presented measurements show a clear overall broadening of the d-scan trace in the dispersion axis in the amplification process, which is a clear sign of an instability increase. If we calculate the instability metric for each d-scan measurement, we see a steep increase from $72.2\,\%$ to values around $81.5\,\%$, with the amplification process. Still, the instability metric does not change significantly when increasing the amplification current, as seen in Figure 6.18.

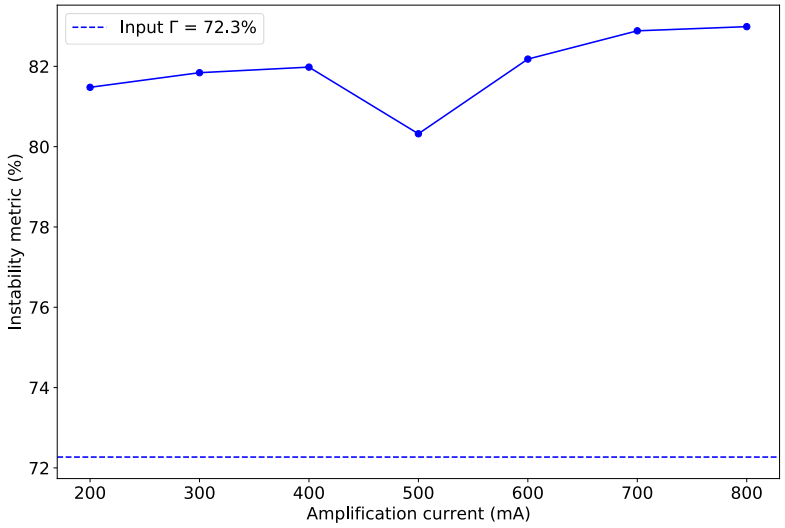


Figure 6.18: Evolution of the instability metric of the amplified pulses with the amplification current.

6.6. Conclusions and future work

In this section, we have studied the amplification process using a semiconductor optical amplifier and its effect on the pulse shape. We have concluded that, depending on the initial pulse shape, a pulse narrowing can occur, which increases with the amplification current. The spectral power experiences a red-shift and a spectral broadening, both increasing with the amplification current. We have correlated our findings with previously developed theoretical models. Driving the amplifier at higher currents or using a lower operating temperature would allow an even higher output power after amplification. The amplification of unstable pulse trains leads to a higher instability metric, as well as shorter pulses, both after the amplifier and after the single-grating compressor. Further investigation of the used SOA can be made, namely studying the influence of the input power on the amplification gain.

To obtain higher output power pulses directly from the SOA, a possible solution would be to use an additional single-grating compressor to fully reverse the pulse asymmetry (i.e., having a pulse with a slowly rising leading edge compared to the trailing edge), as

suggested in section 4.5, chapter 4. In this case, the gain saturation effects could be minimized, and pulse deformation could potentially be reduced. In fact, knowing the temporal profile of the amplified pulses is crucial for employing techniques such as CPA, where the to-be-amplified pulse is highly chirped before the amplification stage. The possibility of further increasing the spectral broadening due to self-phase modulation by using a double-pass configuration [186] could prove useful to further reduce the obtainable pulse width and increase the output power.

7. Conclusions and future work

This doctoral thesis describes the work developed in a joint collaboration between the University of Porto and Heriot-Watt University, intending to further investigate the pulse generation dynamics in semiconductor laser diodes using the dispersion-scan technique.

Firstly, we consolidated previous work developed at University of Porto, by developing a d-scan variation based on surface third-harmonic generation, that allows measuring ultra-broadband, low energy pulses with a ptychographic retrieval algorithm adapted for broadband sources. We have used this variation to characterize sub-10 fs pulses from a Ti:Sapphire oscillator, whose results are in good agreement with the ones obtained using a standard SHG-based d-scan technique. The developed variation allows characterizing ultrashort pulses with arbitrary frequencies and bandwidths, only limited by the detection method. Further work could be developed by measuring ultrashort laser pulses in the mid-infrared (MIR) region, to prove the validity of the method for different spectral regions.

At Heriot-Watt University, we have developed another variation of the d-scan technique, which allows measuring pulses with long durations (tens of picoseconds) and low energies (picoJoules). This setup relies on a single-grating compressor, that applies variable dispersion while being relatively easy to align, a lithium iodate crystal for second harmonic generation, and a monochromator coupled to a photomultiplier tube and a highly-sensitive multimeter to frequency-resolve the nonlinear signal. The minimum energy needed for pulse measurement is only limited by the nonlinear signal detection section sensitivity. We have fully characterized and compressed pulses from a quantum-dot passively mode-locked laser. We have investigated the influence of the driving conditions in the pulse evolution and correlated our findings with theoretical models, as well as compressed the output pulses to a sub-ps regime. The replacement of the $LiIO_3$ crystal with bulk a-PPLN would drastically increase the SHG signal, which could prove sufficient to replace the nonlinear signal detection section with a highly-sensitive non-scanning spectrometer. This would allow a decrease of the typical acquisition time for a d-scan measurement, which would put the technique up to par with previously developed pulse characterization techniques for these spectral bandwidths and pulse energies.

With this setup, we have investigated and, for the first time, quantified pulse train instabilities in semiconductor laser diodes using a self-calibrating retrieval algorithm that retrieves

not only the spectral phase of the pulses but also the dispersion applied by the compressor itself. By comparing the retrieved dispersion with the actual dispersion applied by the compressor, we can create an instability metric that successfully accounts for pulse train instabilities. Coupled with RF measurements, this allows for the distinction of different mode-locking regimes, namely stable mode-locking, unstable mode-locking and harmonic mode-locking (where the repetition rate of the laser is a harmonic of the fundamental repetition rate of the laser). The implementation of feedback loops, either in a active or passive configuration, could eliminate pulse train amplitude modulations, which would improve the pulse train stability for a wide range of driving conditions.

The last developed work during this doctoral thesis was studying the pulse amplification process using semiconductor optical amplifiers. We have used the developed d-scan setup to study the influence of a semiconductor optical amplifier in the amplified pulses. We have concluded that this pulse amplification leads to spectral broadening and a red-shift that increases with the amplification current. We have also seen a pulse compression directly after the amplification process, which has already been predicted theoretically and observed experimentally in other laser sources. These effects depend on the initial pulse shape. The spectral broadening also allows for the generation of even shorter pulses after pulse compression. We have also concluded that the amplification process further increases the pulse train instabilities in an unstable pulse train. Further studies include reversing the asymmetry of the pulses prior to their amplification, to reduce gain saturation effects in the semiconductor optical amplifier, and the use of a double-pass amplification configuration to further increase the output optical power of the amplified laser pulses.

In conclusion, we have developed a new variation of the d-scan technique that allowed gaining new insight into the dynamics of pulse generation in semiconductor laser diodes, as well as study pulse train instabilities in these laser sources. With this privileged information, we can find strategies to cope with these pulse train instabilities, such as optical feedback loops (either active or passive). The further amplification of these light sources using semiconductor optical amplifiers could pave the way to generate shorter, more energetic laser pulses from semiconductor laser diodes, potentially leading to a revolution in the field of ultrafast laser science.

References

[1] T. H. Maiman, “Stimulated optical radiation in ruby,” *Nature*, vol. 187, pp. 493–494, 1960. [Online]. Available: https://ui.adsabs.harvard.edu/abs/1960Natur.187..493M [Cited on page 1.]

[2] F. J. McClung and R. W. Hellwarth, “Giant optical pulsations from ruby,” *Applied Optics*, vol. 1, no. S1, pp. 103–105, 1962. [Online]. Available: https://opg.optica.org/ao/abstract.cfm?URI=ao-1-S1-103 [Cited on page 1.]

[3] L. E. Hargrove, R. L. Fork, and M. A. Pollack, “Locking of He-Ne laser modes induced by synchronous intracavity modulation,” *Applied Physics Letters*, vol. 5, pp. 4–5, 1964. [Online]. Available: https://ui.adsabs.harvard.edu/abs/1964ApPhL...5....4H [Cited on page 1.]

[4] L. A. Fernandes, J. R. Grenier, P. R. Herman, J. S. Aitchison, and P. V. S. Marques, “Femtosecond laser writing of waveguide retarders in fused silica for polarization control in optical circuits,” *Optics Express*, vol. 19, pp. 18 294–18 301, 2011. [Online]. Available: <GotoISI>://WOS:000294781200060 [Cited on page 1.]

[5] A. M. Kowalevicz, V. Sharma, E. P. Ippen, J. G. Fujimoto, and K. Minoshima, “Three-dimensional photonic devices fabricated in glass by use of a femtosecond laser oscillator,” *Optics Letters*, vol. 30, no. 9, pp. 1060–1062, 2005. [Online]. Available: <GotoISI>://WOS:000228562600038

[6] A. Tünnermann, C. Momma, and S. Nolte, “Perspective on ultrashort pulse laser micromachining,” *Applied Physics A*, vol. 129, no. 157, 2023. [Online]. Available: https://doi.org/10.1007/s00339-023-06403-9 [Cited on page 1.]

[7] M. Niemz, *Laser-Tissue Interactions: Fundamentals and Applications*, 2019. [Cited on page 1.]

[8] F. Brightbill, *Corneal Surgery: Theory, Technique and Tissue*. Mosby/Elsevier, 2009. [Online]. Available: https://books.google.pt/books?id=TbFyvZSx6W0C [Cited on page 1.]

[9] C. Maibohm, F. Silva, E. Figueiras, P. T. Guerreiro, M. Brito, R. Romero, H. Crespo, and J. B. Nieder, “SyncRGB-FLIM: synchronous fluorescence imaging

of red, green and blue dyes enabled by ultra-broadband few-cycle laser excitation and fluorescence lifetime detection," *Biomedical Optics Express*, vol. 10, no. 4, pp. 1891–1904, 2019. [Online]. Available: <GotoISI>://WOS:000462887400027 [Cited on page 1.]

[10] D. Huang, F. Li, Z. He, Z. Cheng, C. Shang, and P. K. A. Wai, "400 MHz ultrafast optical coherence tomography," *Optics Letters*, vol. 45, no. 24, pp. 6675–6678, 2020. [Online]. Available: https://opg.optica.org/ol/abstract.cfm?URI=ol-45-24-6675 [Cited on page 1.]

[11] X. Wang, X. Yuan, and L. Shi, "Optical coherence tomography—in situ and high-speed 3D imaging for laser materials processing," *Light: Science Applications*, vol. 11, no. 280, 2022. [Online]. Available: https://doi.org/10.1038/s41377-022-00981-8 [Cited on page 1.]

[12] W. H. Knox, "Ultrafast technology in telecommunications," *IEEE Journal of Selected Topics in Quantum Electronics*, vol. 6, no. 6, pp. 1273–1278, 2000. [Cited on page 1.]

[13] G. A. Keeler, B. E. Nelson, D. Agarwal, C. Debaes, N. C. Helman, A. Bhatnagar, and D. A. B. Miller, "The benefits of ultrashort optical pulses in optically interconnected systems," *IEEE Journal of Selected Topics in Quantum Electronics*, vol. 9, no. 2, pp. 477–485, 2003. [Cited on page 1.]

[14] P. J. Delfyett, C. DePriest, and T. Yilmaz, "Signal processing at the speed of light-waves [photonic ADCs]," *IEEE Circuits and Devices Magazine*, vol. 18, no. 5, pp. 28–35, 2002. [Cited on page 1.]

[15] C. S. Gonçalves, A. S. Silva, D. Navas, M. Miranda, F. Silva, H. Crespo, and D. S. Schmool, "A dual-colour architecture for pump-probe spectroscopy of ultrafast magnetization dynamics in the sub-10-femtosecond range," *Sci Rep*, vol. 6, 2016. [Cited on page 1.]

[16] A. S. Silva, S. P. Sa, S. A. Bunyaev, C. Garcia, I. J. Sola, G. N. Kakazei, H. Crespo, and D. Navas, "Dynamical behaviour of ultrathin [CoFeB (t(CoFeB))/Pd] films with perpendicular magnetic anisotropy," *Scientific Reports*, vol. 11, no. 1, 2021. [Online]. Available: <GotoISI>://WOS:000634374700035 [Cited on page 1.]

[17] A. H. Zewail, “Femtochemistry: Atomic-scale dynamics of the chemical bond using ultrafast lasers (nobel lecture),” *Angew Chem Int Ed Engl*, vol. 39, no. 15, pp. 2586–2631, 2000. [Cited on page 1.]

[18] T. Udem, R. Holzwarth, and T. W. Hänsch, “Optical frequency metrology,” *Nature*, vol. 416, no. 6877, pp. 233–237, 2002. [Online]. Available: https://doi.org/10.1038/416233a [Cited on page 1.]

[19] S. Li, L. Lu, S. Bhattacharyya, C. Pearce, K. Li, E. T. Nienhuis, G. Doumy, R. D. Schaller, S. Moeller, M.-F. Lin, G. Dakovski, D. J. Hoffman, D. Garratt, K. A. Larsen, J. D. Koralek, C. Y. Hampton, D. Cesar, J. Duris, Z. Zhang, N. Sudar, J. P. Cryan, A. Marinelli, X. Li, L. Inhester, R. Santra, and L. Young, “Attosecond-pump attosecond-probe x-ray spectroscopy of liquid water,” *Science*, vol. 383, no. 6687, pp. 1118–1122, 2024. [Online]. Available: https://www.science.org/doi/abs/10.1126/science.adn6059 [Cited on page 1.]

[20] M. Krüger, M. Schenk, and P. Hommelhoff, “Attosecond control of electrons emitted from a nanoscale metal tip,” *Nature*, vol. 475, no. 7354, pp. 78–81, 2011. [Online]. Available: https://doi.org/10.1038/nature10196 [Cited on page 1.]

[21] S. J. Soundararajan, L. Yang, S. Q. Zhang, H. Jani, and L. Z. Duan, “Time-wavelength optical sampling spectroscopy based on dynamic laser cavity tuning,” *Journal of the Optical Society of America B-Optical Physics*, vol. 35, no. 5, pp. 1186–1191, 2018. [Online]. Available: <GotoISI>://WOS:000431180600036 [Cited on page 1.]

[22] G. P. Agrawal and N. K. Dutta, *Semiconductor lasers*. Springer Science Business Media, 2013. [Cited on page 1.]

[23] Y. Li, L. F. Lester, D. Chang, C. Langrock, M. M. Fejer, and D. J. Kane, “Characteristics and instabilities of mode-locked quantum-dot diode lasers,” *Optics Express*, vol. 21, no. 7, pp. 8007–8017, 2013. [Cited on pages 2, 36, and 67.]

[24] M. Radziunas, A. G. Vladimirov, E. A. Viktorov, G. Fiol, H. Schmeckebier, and D. Bimberg, “Strong pulse asymmetry in quantum-dot mode-locked semiconductor lasers,” *Applied Physics Letters*, vol. 98, no. 031104, 2011. [Cited on page 61.]

[25] Y. C. Xin, D. J. Kane, and L. F. Lester, “Frequency-resolved optical gating characterisation of passively modelocked quantum-dot laser,” *Electronics Letters*,

vol. 44, no. 21, pp. 1255–1256, 2008. [Online]. Available: <GotoISI>://WOS:000260471700020 [Cited on pages 36, 59, 61, and 67.]

[26] M.-T. Choi, W. Lee, J.-M. Kim, and P. J. Delfyett, “Ultrashort, high-power pulse generation from a master oscillator power amplifier based on external cavity mode locking of a quantum-dot two-section diode laser,” *Applied Physics Letters*, vol. 87, no. 221107, 2005. [Cited on page 2.]

[27] M. Miranda, T. Fordell, C. Arnold, A. L’Huillier, and H. Crespo, “Simultaneous compression and characterization of ultrashort laser pulses using chirped mirrors and glass wedges,” *Optics Express*, vol. 20, no. 1, pp. 688–697, 2011. [Cited on pages xv, 2, 12, 15, 30, and 39.]

[28] M. Miranda, C. L. Arnold, T. Fordell, F. Silva, B. Alonso, R. Weigand, A. L’Huillier, and H. Crespo, “Characterization of broadband few-cycle laser pulses with the d-scan technique,” *Optics Express*, vol. 20, no. 17, pp. 18 732–18 743, 2012. [Cited on pages 2, 12, and 16.]

[29] O. Svelto, *Principles of Lasers*. Springer US, 2010. [Online]. Available: https://books.google.pt/books?id=ioywRI5W2HEC [Cited on page 3.]

[30] M. Canhota, “Ultrashort light pulses over large spectral ranges: novel sources and dispersion-scan-based spatiotemporal diagnostics,” Thesis, 2018. [Cited on page 3.]

[31] F. Träger, *Springer Handbook of Lasers and Optics*. Springer New York, 2007. [Online]. Available: https://books.google.pt/books?id=YOHJGz-9UNoC [Cited on page 4.]

[32] C. Rulliere, *Femtosecond Laser Pulses: Principles and Experiments*. Springer, 2005. [Online]. Available: https://books.google.pt/books?id=zlFtbKVLJbwC [Cited on page 4.]

[33] R. L. Fork, O. E. Martinez, and J. P. Gordon, “Negative dispersion using pairs of prisms,” *Optics Letters*, vol. 9, no. 5, pp. 150–152, 1984. [Online]. Available: https://opg.optica.org/ol/abstract.cfm?URI=ol-9-5-150 [Cited on page 7.]

[34] V. Chauhan, P. Bowlan, J. Cohen, and R. Trebino, “Single-diffraction-grating and grism pulse compressors,” *Journal of the Optical Society of America*

B-Optical Physics, vol. 27, no. 4, pp. 619–624, 2010. [Online]. Available: <GotoISI>://WOS:000276196000001 [Cited on pages xv, 7, 41, and 42.]

[35] E. Treacy, "Optical pulse compression with diffraction gratings," *IEEE Journal of Quantum Electronics*, vol. 5, no. 9, pp. 454–458, 1969. [Cited on page 7.]

[36] R. Szipöcs, K. Ferencz, C. Spielmann, and F. Krausz, "Chirped multilayer coatings for broadband dispersion control in femtosecond lasers," *Optics Letters*, vol. 19, no. 3, pp. 201–203, 1994. [Online]. Available: https://opg.optica.org/ol/abstract.cfm?URI=ol-19-3-201 [Cited on page 7.]

[37] G. Steinmeyer, D. H. Sutter, L. Gallmann, N. Matuschek, and U. Keller, "Frontiers in ultrashort pulse generation: Pushing the limits in linear and nonlinear optics," *Science*, vol. 286, no. 5444, pp. 1507–1512, 1999. [Online]. Available: https://www.science.org/doi/abs/10.1126/science.286.5444.1507 [Cited on pages xv and 8.]

[38] J.-C. M. Diels, J. J. Fontaine, I. C. McMichael, and F. Simoni, "Control and measurement of ultrashort pulse shapes (in amplitude and phase) with femtosecond accuracy," *Applied Optics*, vol. 24, no. 9, pp. 1270–1282, 1985. [Online]. Available: https://opg.optica.org/ao/abstract.cfm?URI=ao-24-9-1270 [Cited on page 12.]

[39] D. J. Kane and R. Trebino, "Characterization of arbitrary femtosecond pulses using frequency-resolved optical gating," *IEEE Journal of Quantum Electronics*, vol. 29, no. 2, pp. 571–579, 1993. [Cited on page 12.]

[40] C. Iaconis and I. A. Walmsley, "Spectral phase interferometry for direct electric-field reconstruction of ultrashort optical pulses," *Optics Letters*, vol. 23, no. 10, pp. 792–794, 1998. [Online]. Available: https://opg.optica.org/ol/abstract.cfm?URI=ol-23-10-792 [Cited on page 12.]

[41] V. Lozovoy, I. Pastirk, and M. Dantus, "Multiphoton intrapulse interference. IV. ultrashort laser pulse spectral phase characterization and compensation," *Optics letters*, vol. 29, pp. 775–777, 2004. [Cited on page 12.]

[42] C. Iaconis and I. A. Walmsley, "Self-referencing spectral interferometry for measuring ultrashort optical pulses," *IEEE Journal of Quantum Electronics*, vol. 35, no. 4, pp. 501–509, 1999. [Cited on page 13.]

[43] I. A. Walmsley, *Characterization of Ultrashort Optical Pulses in the Few-Cycle Regime Using Spectral Phase Interferometry for Direct Electric-Field Reconstruction*. Berlin, Heidelberg: Springer Berlin Heidelberg, 2004, pp. 265–292. [Online]. Available: https://doi.org/10.1007/978-3-540-39849-3_6 [Cited on page 13.]

[44] B. Xu, J. M. Gunn, J. M. D. Cruz, V. V. Lozovoy, and M. Dantus, "Quantitative investigation of the multiphoton intrapulse interference phase scan method for simultaneous phase measurement and compensation of femtosecond laser pulses," *Journal of the Optical Society of America B*, vol. 23, no. 4, pp. 750–759, 2006. [Online]. Available: https://opg.optica.org/josab/abstract.cfm?URI=josab-23-4-750 [Cited on page 14.]

[45] M. Miranda, J. Penedones, C. Guo, A. Harth, M. Louisy, L. Neoričić, A. L'Huillier, and C. L. Arnold, "Fast iterative retrieval algorithm for ultrashort pulse characterization using dispersion scans," *Journal of the Optical Society of America B*, vol. 34, no. 1, pp. 190–197, 2016. [Cited on page 16.]

[46] E. Escoto, A. Tajalli, T. Nagy, and G. Steinmeyer, "Advanced phase retrieval for dispersion scan: a comparative study," *Journal of the Optical Society of America B*, vol. 35, no. 1, pp. 8–19, 2017.

[47] D. Gerth, E. Escoto, G. Steinmeyer, and B. Hofmann, "Regularized differential evolution for a blind phase retrieval problem in ultrashort laser pulse characterization," *Review of Scientific Instruments*, vol. 90, no. 4, 2019. [Online]. Available: https://doi.org/10.1063/1.5085937

[48] N. C. Geib, M. Zilk, T. Pertsch, and F. Eilenberger, "Common pulse retrieval algorithm: a fast and universal method to retrieve ultrashort pulses," *Optica*, vol. 6, no. 4, pp. 495–505, 2019. [Cited on page 16.]

[49] S. Kleinert, A. Tajalli, T. Nagy, and U. Morgner, "Rapid phase retrieval of ultrashort pulses from dispersion scan traces using deep neural networks," *Optics Letters*, vol. 44, no. 4, pp. 979–982, 2019. [Cited on page 16.]

[50] E. Escoto, R. Jafari, R. Trebino, and G. Steinmeyer, "Retrieving the coherent artifact in frequency-resolved optical gating," *Optics Letters*, vol. 44, no. 12, pp. 3142–3145, 2019. [Online]. Available: https://www.ncbi.nlm.nih.gov/pubmed/31199401 [Cited on pages 17 and 70.]

[51] M. Rhodes, Z. Guang, and R. Trebino, “Unstable and multiple pulsing can be invisible to ultrashort pulse measurement techniques,” *Applied Sciences*, vol. 7, no. 40, 2017. [Online]. Available: https://www.mdpi.com/2076-3417/7/1/40 [Cited on pages 17 and 68.]

[52] T. Gomes, M. Canhota, and H. Crespo, “Temporal characterization of broadband femtosecond laser pulses by a surface third-harmonic dispersion scan with ptychographic retrieval,” *Optics Letters*, vol. 47, no. 15, pp. 3660–3663, 2022. [Cited on pages xv, 19, 21, 26, 27, 28, and 29.]

[53] F. Silva, M. Miranda, S. Teichmann, M. Baudisch, M. Massicotte, F. Koppens, J. Biegert, and H. Crespo, “Near to mid-IR ultra-broadband third harmonic generation in multilayer graphene: few-cycle pulse measurement using THG dispersion-scan,” in *CLEO: 2013*, ser. OSA Technical Digest (online). Optica Publishing Group, Conference Proceedings, p. CW1H.5. [Cited on page 19.]

[54] M. Hoffmann, T. Nagy, T. Willemsen, M. Jupé, D. Ristau, and U. Morgner, “Pulse characterization by THG d-scan in absorbing nonlinear media,” *Optics Express*, vol. 22, no. 5, pp. 5234–5234, 2013. [Cited on page 19.]

[55] A. Tajalli, B. Chanteau, M. Kretschmar, H. G. Kurz, D. Zuber, M. Kovačev, U. Morgner, and T. Nagy, “Few-cycle optical pulse characterization via cross-polarized wave generation dispersion scan technique,” *Optics Letters*, vol. 41, no. 22, pp. 5246–5249, 2016. [Cited on page 19.]

[56] A. Tajalli, M. Ouille, A. Vernier, F. Bottle, E. Escoto, S. Kleinert, R. Romero, J. Csontos, U. Morgner, G. Steinmeyer, H. M. Crespo, R. L. Martens, and T. Nagy, “Propagation effects in the characterization of 1.5-cycle pulses by XPW dispersion scan,” *Ieee Journal of Selected Topics in Quantum Electronics*, vol. 25, no. 4, 2019. [Online]. Available: <GotoISI>://WOS:000447076500001

[57] A. Tajalli, T. K. Kalousdian, M. Kretschmar, S. Kleinert, U. Morgner, and T. Nagy, “Full characterization of 8 fs deep UV pulses via a dispersion scan,” *Optics Letters*, vol. 44, no. 10, pp. 2498–2501, 2019. [Cited on page 19.]

[58] M. Canhota, F. Silva, R. Weigand, and H. M. Crespo, “Inline self-diffraction dispersion-scan of over octave-spanning pulses in the single-cycle regime,” *Optics Letters*, vol. 42, no. 15, pp. 3048–3051, 2017. [Cited on page 19.]

[59] M. Canhota, R. Weigand, and H. M. Crespo, “Simultaneous measurement of two ultrashort near-ultraviolet pulses produced by a multiplate continuum using dual self-diffraction dispersion-scan,” *Optics Letters*, vol. 44, no. 4, pp. 1015–1018, 2019. [Cited on page 19.]

[60] H. M. Crespo, T. Witting, M. Canhota, M. Miranda, and J. W. G. Tisch, “In situ temporal measurement of ultrashort laser pulses at full power during high-intensity laser–matter interactions,” *Optica*, vol. 7, no. 8, pp. 995–1002, 2020. [Cited on page 19.]

[61] F. Silva, B. Alonso, W. Holgado, R. Romero, J. S. Román, E. C. Jarque, H. Koop, V. Pervak, H. Crespo, and I. J. Sola, “Strategies for achieving intense single-cycle pulses with in-line post-compression setups,” *Optics Letters*, vol. 43, no. 2, pp. 337–340, 2018. [Online]. Available: https://opg.optica.org/ol/abstract.cfm?URI=ol-43-2-337 [Cited on page 19.]

[62] F. Silva, M. Miranda, B. Alonso, J. Rauschenberger, V. Pervak, and H. Crespo, “Simultaneous compression, characterization and phase stabilization of GW-level 1.4 cycle VIS-NIR femtosecond pulses using a single dispersion-scan setup,” *Optics Express*, vol. 22, no. 9, pp. 10 181–10 191, 2014. [Online]. Available: https://opg.optica.org/oe/abstract.cfm?URI=oe-22-9-10181 [Cited on page 19.]

[63] T. Y. F. Tsang, “Optical third-harmonic generation at interfaces,” *Physical Review A*, vol. 52, no. 5, pp. 4116–4125, 1995. [Online]. Available: https://link.aps.org/doi/10.1103/PhysRevA.52.4116 [Cited on page 19.]

[64] T. Tsang, “Third- and fifth-harmonic generation at the interfaces of glass and liquids,” *Physical Review A*, vol. 54, no. 6, pp. 5454–5457, 1996. [Online]. Available: https://link.aps.org/doi/10.1103/PhysRevA.54.5454 [Cited on page 19.]

[65] G. Yi, H. Lee, J. Jiannan, B. J. Chun, S. Han, H. Kim, Y. W. Kim, D. Kim, S.-W. Kim, and Y.-J. Kim, “Nonlinear third harmonic generation at crystalline sapphires,” *Optics Express*, vol. 25, no. 21, pp. 26 002–26 010, 2017. [Online]. Available: https://opg.optica.org/oe/abstract.cfm?URI=oe-25-21-26002 [Cited on page 20.]

[66] T. Tsang, M. A. Krumbügel, K. W. DeLong, D. N. Fittinghoff, and R. Trebino, “Frequency-resolved optical-gating measurements of ultrashort pulses using surface third-harmonic generation,” *Optics Letters*, vol. 21, no. 17, pp.

1381–1383, 1996. [Online]. Available: https://opg.optica.org/ol/abstract.cfm?URI=ol-21-17-1381 [Cited on page 20.]

[67] J. Hyyti, E. Escoto, and G. Steinmeyer, "Third-harmonic interferometric frequency-resolved optical gating," *Journal of the Optical Society of America B*, vol. 34, no. 11, pp. 2367–2375, 2017. [Online]. Available: https://opg.optica.org/josab/abstract.cfm?URI=josab-34-11-2367 [Cited on page 20.]

[68] A. S. Johnson, E. B. Amuah, C. Brahms, and S. Wall, "Measurement of 10 fs pulses across the entire visible to near-infrared spectral range," *Scientific Reports*, vol. 10, no. 4690, 2020. [Online]. Available: https://doi.org/10.1038/s41598-020-61620-z [Cited on page 20.]

[69] P. Sidorenko, O. Lahav, Z. Avnat, and O. Cohen, "Ptychographic reconstruction algorithm for frequency-resolved optical gating: super-resolution and supreme robustness," *Optica*, vol. 3, no. 12, pp. 1320–1330, 2016. [Cited on page 22.]

[70] A. M. Wilhelm, D. D. Schmidt, D. E. Adams, and C. G. Durfee, "Measuring simultaneously spatially and temporally focused ultrafast laser pulses using the dispersion scan technique," in *Conference on Lasers and Electro-Optics*, ser. OSA Technical Digest (online). Optica Publishing Group, Conference Proceedings, p. SM3H.6. [Cited on pages 22 and 24.]

[71] D.-M. Spangenberg, E. Rohwer, M. Brügmann, and T. Feurer, "Extending time-domain ptychography to generalized phase-only transfer functions," *Optics Letters*, vol. 45, no. 2, pp. 300–303, 2020. [Cited on page 22.]

[72] Z. Chen, Y. Jiang, Y.-T. Shao, M. E. Holtz, M. Odstrčil, M. Guizar-Sicairos, I. Hanke, S. Ganschow, D. G. Schlom, and D. A. Muller, "Electron ptychography achieves atomic-resolution limits set by lattice vibrations," *Science*, vol. 372, no. 6544, pp. 826–831, 2021. [Online]. Available: https://doi.org/10.1126/science.abg2533 [Cited on page 22.]

[73] J. Deng, C. Preissner, J. A. Klug, S. Mashrafi, C. Roehrig, Y. Jiang, Y. Yao, M. Wojcik, M. D. Wyman, D. Vine, K. Yue, S. Chen, T. Mooney, M. Wang, Z. Feng, D. Jin, Z. Cai, B. Lai, and S. Vogt, "The velociprobe: An ultrafast hard x-ray nanoprobe for high-resolution ptychographic imaging," *Rev Sci Instrum*, vol. 90, no. 083701, 2019. [Cited on page 22.]

[74] A. M. Wilhelm, D. D. Schmidt, D. E. Adams, and C. G. Durfee, “Multi-mode root preserving ptychographic phase retrieval algorithm for dispersion scan,” *Optics Express*, vol. 29, no. 14, pp. 22 080–22 095, 2021. [Cited on pages 22 and 24.]

[75] T. d. S. Gomes, H. Crespo, and M. A. Cataluna, “Characterization and compression of ultrashort pulses from mode-locked laser diodes using dispersion-scan,” in *CLEO 2023*, ser. Technical Digest Series. Optica Publishing Group, Conference Proceedings, p. STh3Q.3. [Online]. Available: https://opg.optica.org/abstract.cfm?URI=CLEO_SI-2023-STh3Q.3 [Cited on pages xvi, 31, 40, and 55.]

[76] T. Gomes, H. Crespo, and M. A. Cataluna, “Detection and investigation of pulse asymmetries in passively mode-locked quantum-dot laser diodes using dispersion-scan,” in *2023 Conference on Lasers and Electro-Optics Europe European Quantum Electronics Conference (CLEO/Europe-EQEC)*, Conference Proceedings, pp. 1–1. [Cited on pages xvi, 31, 40, and 55.]

[77] R. N. Hall, G. E. Fenner, J. D. Kingsley, T. J. Soltys, and R. O. Carlson, “Coherent light emission from gaas junctions,” *Physical Review Letters*, vol. 9, no. 9, pp. 366–368, 1962. [Online]. Available: https://link.aps.org/doi/10.1103/PhysRevLett.9.366 [Cited on page 31.]

[78] R. D. Dupuis, P. D. Dapkus, J. Holonyak, Nick, E. A. Rezek, and R. Chin, “Room−temperature laser operation of quantum−well $Ga_{(1x)}Al_xAs$−$GaAs$ laser diodes grown by metalorganic chemical vapor deposition,” *Applied Physics Letters*, vol. 32, no. 5, pp. 295–297, 1978. [Online]. Available: https://doi.org/10.1063/1.90026 [Cited on page 31.]

[79] R. Dingle, W. Wiegmann, and C. H. Henry, “Quantum states of confined carriers in very thin $Al_xGa_{1-x}As$-$GaAs$-$Al_xGa_{1-x}As$ heterostructures,” *Physical Review Letters*, vol. 33, no. 14, pp. 827–830, 1974. [Online]. Available: https://link.aps.org/doi/10.1103/PhysRevLett.33.827 [Cited on page 31.]

[80] E. U. Rafailov, M. Cataluna, and E. Avrutin, *Ultrafast Lasers Based on Quantum Dot Structures: Physics and Devices*, 2011. [Cited on pages xv and 32.]

[81] P. S. Zory, *Quantum well lasers*. Academic Press, 1993. [Cited on page 31.]

[82] P. Vasil’ev, *Ultrafast Diode Lasers: Fundamentals and Applications*, 1995. [Cited on pages 32 and 33.]

[83] S. Bischoff, J. Mørk, T. Franck, S. D. Brorson, M. Hofmann, K. Fröjdh, L. Prip, and M. P. Sørensen, "Monolithic colliding pulse mode-locked semiconductor lasers," *Quantum and Semiclassical Optics: Journal of the European Optical Society Part B*, vol. 9, no. 655, 1997. [Online]. Available: https://dx.doi.org/10.1088/1355-5111/9/5/002 [Cited on page 32.]

[84] X. Huang, A. Stintz, H. Li, L. F. Lester, J. Cheng, and K. J. Malloy, "Passive mode-locking in 1.3 μm two-section InAs quantum dot lasers," *Applied Physics Letters*, vol. 78, no. 19, p. 2825–2827, 2001. [Cited on pages 32 and 35.]

[85] L. Zhang, L.-S. Cheng, A. Gray, H. Huang, S. Kutty, H. Li, J. Nagyvary, F. Nabulsi, L. Olona, E. Pease, Q. Sun, C. Wiggins, J. Zilko, Z. Zou, and P. Varangis, *High-power low-jitter quantum-dot passively mode-locked lasers*, ser. Integrated Optoelectronic Devices 2006. SPIE, 2006, vol. 6115. [Online]. Available: https://doi.org/10.1117/12.661322 [Cited on page 32.]

[86] E. U. Rafailov, M. A. Cataluna, and W. Sibbett, "Mode-locked quantum-dot lasers," *Nature Photonics*, vol. 1, no. 7, p. 395–401, 2007. [Cited on pages xv, xvi, 33, and 34.]

[87] M. G. Thompson, A. R. Rae, M. Xia, R. V. Penty, and I. H. White, "InGaAs quantum-dot mode-locked laser diodes," *IEEE Journal of Selected Topics in Quantum Electronics*, vol. 15, no. 3, pp. 661–672, 2009. [Online]. Available: <GotoISI>://WOS:000266928700023 [Cited on pages xv, 34, and 35.]

[88] Z. Bakonyi, S. Hui, G. Onishchukov, L. F. Lester, A. L. Gray, T. C. Newell, and A. Tunnermann, "High-gain quantum-dot semiconductor optical amplifier for 1300 nm," *IEEE Journal of Quantum Electronics*, vol. 39, no. 11, pp. 1409–1414, 2003. [Cited on page 34.]

[89] E. U. Rafailov, P. Loza-Alvarez, W. Sibbett, G. S. Sokolovskii, D. A. Livshits, A. E. Zhukov, and V. M. Ustinov, "Amplification of femtosecond pulses over by 18 dB in a quantum-dot semiconductor optical amplifier," *IEEE Photonics Technology Letters*, vol. 15, no. 8, pp. 1023–1025, 2003. [Cited on page 34.]

[90] P. Borri, S. Schneider, W. Langbein, and D. Bimberg, "Ultrafast carrier dynamics in InGaAs quantum dot materials and devices," *Journal of Optics A: Pure and Applied Optics*, vol. 8, no. 4, p. S33, 2006. [Online]. Available: https://dx.doi.org/10.1088/1464-4258/8/4/S03 [Cited on pages 35 and 91.]

[91] D. B. Malins, A. Gomez-Iglesias, S. J. White, W. Sibbett, A. Miller, and E. U. Rafailov, "Ultrafast electroabsorption dynamics in an InAs quantum dot saturable absorber at 1.3μm," *Applied Physics Letters*, vol. 89, no. 17, pp. 171 111–171 114, 2006. [Cited on page 35.]

[92] V. Ustinov, A. Zhukov, A. Egorov, and N. Maleev, *Quantum Dot Lasers*. Oxford Science Publications, 2003. [Cited on page 35.]

[93] S. S. Mikhrin, A. R. Kovsh, I. L. Krestnikov, A. V. Kozhukhov, D. A. Livshits, N. N. Ledentsov, Y. M. Shernyakov, I. I. Novikov, M. V. Maximov, V. M. Ustinov, and Z. I. Alferov, "High power temperature-insensitive 1.3 μm InAs/InGaAs/GaAs quantum dot lasers," *Semiconductor Science and Technology*, vol. 20, no. 340, 2005. [Online]. Available: https://dx.doi.org/10.1088/0268-1242/20/5/002 [Cited on page 35.]

[94] M. G. Thompson, K. T. Tan, C. Marinelli, K. A. Williams, R. V. Penty, I. H. White, M. Kuntz, D. Ouyang, D. Bimberg, V. M. Ustinov, A. Zhukov, A. Kovsh, N. Ledentsov, D. J. Kang, and M. Blamire, "Transform-limited optical pulses from 18 GHz monolithic modelocked quantum dot lasers operating at $\approx$ 1.3 μm," *Electronics Letters*, vol. 40, pp. 346–347, 2004. [Cited on page 35.]

[95] E. U. Rafailov, M. A. Cataluna, W. Sibbett, N. D. Il'inskaya, Y. M. Zadiranov, A. E. Zhukov, V. M. Ustinov, D. A. Livshits, A. R. Kovsh, and N. N. Ledentsov, "High-power picosecond and femtosecond pulse generation from a two-section mode-locked quantum-dot laser," *Applied Physics Letters*, vol. 87, no. 8, 2005. [Online]. Available: <GotoISI>://WOS:000231310700007 [Cited on page 35.]

[96] M. Laemmlin, G. Fiol, C. Meuer, M. Kuntz, F. Hopfer, A. R. Kovsh, N. N. Ledentsov, and D. H. Bimberg, "Distortion-free optical amplification of 20-80 GHz modelocked laser pulses at 1.3 μm using quantum dots," *Electronics Letters*, vol. 42, pp. 697–699, 2006. [Cited on page 35.]

[97] M. G. Thompson, A. Rae, R. L. Sellin, C. Marinelli, R. V. Penty, I. H. White, A. R. Kovsh, S. S. Mikhrin, D. A. Livshits, and I. L. Krestnikov, "Subpicosecond high-power mode locking using flared waveguide monolithic quantum-dot lasers," *Applied Physics Letters*, vol. 88, no. 13, 2006. [Online]. Available: https://doi.org/10.1063/1.2186110 [Cited on page 35.]

[98] J. K. Mee, M. T. Crowley, N. Patel, D. Murrell, R. Raghunathan, A. Aboketaf, A. Elshaari, S. F. Preble, P. Ampadu, and L. F. Lester, "A passively mode-locked quantum-dot laser operating over a broad temperature range," *Applied Physics Letters*, vol. 101, no. 7, 2012. [Online]. Available: <GotoISI>://WOS:000308263100012 [Cited on page 35.]

[99] M. A. Cataluna, E. A. Viktorov, P. Mandel, W. Sibbett, D. A. Livshits, J. Weimert, A. R. Kovsh, and E. U. Rafailov, "Temperature dependence of pulse duration in a mode-locked quantum-dot laser," *Applied Physics Letters*, vol. 90, no. 10, 2007. [Online]. Available: <GotoISI>://WOS:000244791700002 [Cited on page 35.]

[100] P. Finch, P. Blood, P. M. Smowton, A. Sobiesierski, R. M. Gwilliam, and I. O'Driscoll, "Femtosecond pulse generation in passively mode locked InAs quantum dot lasers," *Applied Physics Letters*, vol. 103, no. 13, 2013. [Online]. Available: https://doi.org/10.1063/1.4822433 [Cited on page 35.]

[101] F. Lelarge, B. Dagens, J. Renaudier, R. Brenot, A. Accard, F. v. Dijk, D. Make, O. L. Gouezigou, J. G. Provost, F. Poingt, J. Landreau, O. Drisse, E. Derouin, B. Rousseau, F. Pommereau, and G. H. Duan, "Recent advances on InAs/InP quantum dash based semiconductor lasers and optical amplifiers operating at 1.55 μm," *IEEE Journal of Selected Topics in Quantum Electronics*, vol. 13, no. 1, pp. 111–124, 2007. [Cited on page 35.]

[102] A. R. Rae, M. G. Thompson, R. V. Penty, I. H. White, A. R. Kovsh, S. S. Mikhrin, D. A. Livshits, and I. L. Krestnikov, "Harmonic mode-locking of a quantum-dot laser diode," in *LEOS 2006 - 19th Annual Meeting of the IEEE Lasers and Electro-Optics Society*, Conference Proceedings, pp. 874–875. [Cited on page 35.]

[103] S. Latkowski, R. Maldonado-Basilio, and P. Landais, "Sub-picosecond pulse generation by 40-GHz passively mode-locked quantum-dash 1-mm-long fabry-perot laser diode," *Optics Express*, vol. 17, no. 21, pp. 19 166–19 172, 2009. [Online]. Available: <GotoISI>://WOS:000270766800084 [Cited on pages 36 and 55.]

[104] H. Schmeckebier, G. Fiol, C. Meuer, D. Arsenijević, and D. Bimberg, "Complete pulse characterization of quantum dot mode-locked lasers suitable for optical communication up to 160 gbit/s," *Optics Express*, vol. 18, no. 4, pp. 3415–3425, 2010. [Cited on pages 36, 55, 59, and 61.]

[105] C. Dorrer and I. Kang, “Simultaneous temporal characterization of telecommunication optical pulses and modulators by use of spectrograms,” *Optics Letters*, vol. 27, no. 15, pp. 1315–1317, 2002. [Online]. Available: https://opg.optica.org/ol/abstract.cfm?URI=ol-27-15-1315 [Cited on page 37.]

[106] T. Habruseva, S. O’Donoghue, N. Rebrova, D. A. Reid, L. P. Barry, D. Rachinskii, G. Huyet, and S. P. Hegarty, “Quantum-dot mode-locked lasers with dual-mode optical injection,” *IEEE Photonics Technology Letters*, vol. 22, no. 6, p. 359–361, 2010. [Cited on pages 37 and 59.]

[107] D. A. Reid, S. G. Murdoch, and L. P. Barry, “Stepped-heterodyne optical complex spectrum analyzer,” *Optics Express*, vol. 18, no. 19, pp. 19 724–19 731, 2010. [Online]. Available: https://opg.optica.org/oe/abstract.cfm?URI=oe-18-19-19724 [Cited on page 37.]

[108] S. G. Murdoch, R. T. Watts, Y. Q. Xu, R. Maldonado-Basilio, J. Parra-Cetina, S. Latkowski, P. Landais, and L. P. Barry, “Spectral amplitude and phase measurement of a 40 GHz free-running quantum-dash modelocked laser diode,” *Optics Express*, vol. 19, no. 14, pp. 13 628–13 635, 2011. [Online]. Available: https://opg.optica.org/oe/abstract.cfm?URI=oe-19-14-13628 [Cited on pages 37 and 55.]

[109] P. M. Stolarz, G. Mezosi, M. J. Strain, A. C. Bryce, and M. Sorel, “Highly-sensitive sonogram for assessment of chirp in semiconductor mode-locked lasers,” *IEEE Journal of Quantum Electronics*, vol. 48, no. 8, pp. 995–1003, 2012. [Online]. Available: <GotoISI>://WOS:000306514400001 [Cited on pages 37, 38, 59, and 62.]

[110] C. Dorrer and M. Joffre, “Characterization of the spectral phase of ultrashort light pulses,” *Comptes Rendus de l’Académie des Sciences - Series IV - Physics*, vol. 2, no. 10, pp. 1415–1426, 2001. [Online]. Available: https://www.sciencedirect.com/science/article/pii/S1296214701012793 [Cited on page 37.]

[111] D. Duchesne, L. Razzari, L. Halloran, R. Morandotti, A. J. SpringThorpe, D. N. Christodoulides, and D. J. Moss, “Two-photon photodetector in a multiquantum well GaAs laser structure at 1.55μm,” *Optics Express*, vol. 17, no. 7, pp. 5298–5310, 2009. [Online]. Available: https://opg.optica.org/oe/abstract.cfm?URI=oe-17-7-5298 [Cited on page 37.]

[112] T. F. Albrecht, K. Seibert, and H. Kurz, “Chirp measurement of large-bandwidth femtosecond optical pulses using two-photon absorption,” *Optics Communications*, vol. 84, no. 5, pp. 223–227, 1991. [Online]. Available: https://www.sciencedirect.com/science/article/pii/003040189190076P [Cited on page 37.]

[113] D. Burghoff, Y. Yang, D. J. Hayton, J.-R. Gao, J. L. Reno, and Q. Hu, “Evaluating the coherence and time-domain profile of quantum cascade laser frequency combs,” *Optics Express*, vol. 23, no. 2, pp. 1190–1202, 2015. [Online]. Available: https://opg.optica.org/oe/abstract.cfm?URI=oe-23-2-1190 [Cited on page 38.]

[114] D. Burghoff, T.-Y. Kao, N. Han, C. W. I. Chan, X. Cai, Y. Yang, D. J. Hayton, J.-R. Gao, J. L. Reno, and Q. Hu, “Terahertz laser frequency combs,” *Nature Photonics*, vol. 8, no. 6, pp. 462–467, 2014. [Online]. Available: https://doi.org/10.1038/nphoton.2014.85 [Cited on page 38.]

[115] J. Hillbrand, A. M. Andrews, H. Detz, G. Strasser, and B. Schwarz, “Coherent injection locking of quantum cascade laser frequency combs,” *Nature Photonics*, vol. 13, no. 2, pp. 101–104, 2019. [Online]. Available: https://doi.org/10.1038/s41566-018-0320-3 [Cited on page 38.]

[116] D. Bajek and M. A. Cataluna, “Fast optical sampling by electronic repetition-rate tuning using a single mode-locked laser diode,” *Optics Express*, vol. 29, no. 5, pp. 6890–6902, 2021. [Online]. Available: https://opg.optica.org/oe/abstract.cfm?URI=oe-29-5-6890 [Cited on page 38.]

[117] M. Lai, S. T. Lai, and C. Swinger, “Single-grating laser pulse stretcher and compressor,” *Applied Optics*, vol. 33, no. 30, pp. 6985–6987, 1994. [Online]. Available: https://opg.optica.org/ao/abstract.cfm?URI=ao-33-30-6985 [Cited on page 41.]

[118] 2024. [Online]. Available: https://www.lasercalculator.com/grating-pair-dispersion-calculator/ [Cited on page 42.]

[119] C. Calo, H. Schmeckebier, K. Merghem, R. Rosales, F. Lelarge, A. Martinez, D. Bimberg, and A. Ramdane, “Frequency resolved optical gating characterization of sub-ps pulses from single-section InAs/InP quantum dash based mode-locked lasers,” *Optics Express*, vol. 22, no. 2, pp. 1742–1748, 2014. [Online]. Available: <GotoISI>://WOS:000330585100056 [Cited on page 55.]

[120] Y. Ding, W. Rehbein, M. Moehrle, M. Zander, M. Schell, K. Kolpatzeck, and J. C. Balzer, “Group velocity dispersion in high-performance BH InAs/InP QD and InGaAsP/InP QW two-section passively mode-locked lasers,” *Optics Express*, vol. 30, no. 14, pp. 24 353–24 361, 2022. [Cited on page 55.]

[121] B. Resan, L. Archundia, and P. J. Delfyett, “FROG measured high-power 185-fs pulses generated by down-chirping of the dispersion-managed breathing-mode semiconductor mode-locked laser,” *IEEE Photonics Technology Letters*, vol. 17, no. 7, pp. 1384–1386, 2005. [Online]. Available: <GotoISI>://WOS: 000230052900008 [Cited on page 55.]

[122] J. Kim, M.-T. Choi, and P. J. Delfyett, “Pulse generation and compression via ground and excited states from a grating coupled passively mode-locked quantum dot two-section diode laser,” *Applied Physics Letters*, vol. 89, no. 26, 2006. [Online]. Available: https://doi.org/10.1063/1.2410217 [Cited on page 55.]

[123] M. Radziunas, A. G. Vladimirov, E. A. Viktorov, G. Fiol, H. Schmeckebier, and D. Bimberg, “Pulse broadening in quantum-dot mode-locked semiconductor lasers: Simulation, analysis, and experiments,” *IEEE Journal of Quantum Electronics*, vol. 47, no. 7, pp. 935–943, 2011. [Cited on page 55.]

[124] R. Mindaugas, G. V. Andrei, and A. V. Evgeny, “Traveling wave modeling, simulation, and analysis of quantum-dot mode-locked semiconductor lasers,” in *Proc.SPIE*, vol. 7720, Conference Proceedings, p. 77200X. [Online]. Available: https://doi.org/10.1117/12.853825 [Cited on page 55.]

[125] J. K. Mee, R. Raghunathan, D. Murrell, A. Braga, Y. Li, and L. F. Lester, “Reduced group delay dispersion in quantum dot passively mode-locked lasers operating at elevated temperature,” *Proc. of SPIE*, vol. 9193, no. 919311, 2014. [Cited on page 60.]

[126] Y. Bidaux, K. A. Fedorova, D. A. Livshits, E. U. Rafailov, and J. Faist, “Investigation of the chromatic dispersion in two-section InAs/GaAs quantum-dot lasers,” *IEEE Photonics Technology Letters*, vol. 29, no. 24, p. 2246–2249, 2017. [Cited on pages 60 and 93.]

[127] M. A. Cataluna, “Ultrashort-pulse generation from quantum-dot semiconductor diode lasers,” Thesis, 2007. [Cited on pages xvii, 60, and 61.]

[128] D. J. Derickson, R. J. Helkey, A. Mar, J. R. Karin, J. G. Wasserbauer, and J. E. Bowers, "Short pulse generation using multisegment mode-locked semiconductor lasers," *IEEE Journal of Quantum Electronics*, vol. 28, no. 10, pp. 2186–2202–2186–2202, 1992. [Cited on pages xvii and 61.]

[129] N. G. Usechak, Y. Xin, C.-Y. Lin, L. F. Lester, D. J. Kane, and V. Kovanis, "Modeling and direct electric-field measurements of passively mode-locked quantum-dot lasers," *IEEE Journal of Selected Topics in Quantum Electronics*, vol. 15, no. 3, p. 653–660, 2009. [Cited on page 61.]

[130] M. Rossetti, P. Bardella, and I. Montrosset, "Time-domain travelling-wave model for quantum dot passively mode-locked lasers," *IEEE Journal of Quantum Electronics*, vol. 47, no. 2, pp. 139–150, 2011. [Online]. Available: <GotoISI>://WOS:000286007800001 [Cited on pages 61 and 90.]

[131] R. A. Fisher and J. Fleck, J. A., "On the phase characteristics and compression of picosecond pulses," *Applied Physics Letters*, vol. 15, no. 9, pp. 287–290, 1969. [Online]. Available: https://doi.org/10.1063/1.1653002 [Cited on page 67.]

[132] E. Escoto, R. Jafari, G. Steinmeyer, and R. Trebino, "Linear chirp instability analysis for ultrafast pulse metrology," *Journal of the Optical Society of America B*, vol. 37, no. 1, pp. 74–81, 2020. [Online]. Available: https://opg.optica.org/josab/abstract.cfm?URI=josab-37-1-74 [Cited on pages 68 and 70.]

[133] G. I. Haham, P. Sidorenko, O. Lahav, and O. Cohen, "Multiplexed FROG," *Optics Express*, vol. 25, no. 26, pp. 33 007–33 017, 2017. [Online]. Available: https://opg.optica.org/oe/abstract.cfm?URI=oe-25-26-33007 [Cited on page 68.]

[134] M. Rhodes, G. Steinmeyer, J. Ratner, and R. Trebino, "Pulse-shape instabilities and their measurement," *Laser Photonics Reviews*, vol. 7, no. 4, pp. 557–565, 2013. [Online]. Available: https://onlinelibrary.wiley.com/doi/abs/10.1002/lpor.201200102 [Cited on pages 68 and 70.]

[135] M. Rhodes, G. Steinmeyer, and R. Trebino, "Standards for ultrashort-laser-pulse-measurement techniques and their consideration for self-referenced spectral interferometry," *Applied Optics*, vol. 53, no. 16, pp. D1–D11, 2014. [Online]. Available: https://opg.optica.org/ao/abstract.cfm?URI=ao-53-16-D1 [Cited on page 68.]

[136] T. Pfeifer, Y. Jiang, S. Düsterer, R. Moshammer, and J. Ullrich, "Partial-coherence method to model experimental free-electron laser pulse statistics," *Optics Letters*, vol. 35, no. 20, pp. 3441–3443, 2010. [Online]. Available: https://opg.optica.org/ol/abstract.cfm?URI=ol-35-20-3441 [Cited on page 69.]

[137] J. Ratner, G. Steinmeyer, T. C. Wong, R. Bartels, and R. Trebino, "Coherent artifact in modern pulse measurements," *Optics Letters*, vol. 37, no. 14, pp. 2874–2876, 2012. [Online]. Available: https://opg.optica.org/ol/abstract.cfm?URI=ol-37-14-2874 [Cited on page 70.]

[138] B. Alonso, S. Torres-Peiró, R. Romero, P. T. Guerreiro, A. Almagro-Ruiz, H. Muñoz-Marco, P. Pérez-Millán, and H. Crespo, "Detection and elimination of pulse train instabilities in broadband fibre lasers using dispersion scan," *Scientific Reports*, vol. 10, no. 7242, 2020. [Cited on pages 70, 73, and 74.]

[139] V. V. Lozovoy, G. Rasskazov, D. Pestov, and M. Dantus, "Quantifying noise in ultrafast laser sources and its effect on nonlinear applications," *Optics Express*, vol. 23, no. 9, pp. 12 037–12 044, 2015. [Online]. Available: https://opg.optica.org/oe/abstract.cfm?URI=oe-23-9-12037 [Cited on page 72.]

[140] C. Bourassin-Bouchet and M. E. Couprie, "Partially coherent ultrafast spectrography," *Nature Communications*, vol. 6, no. 6465, 2015. [Online]. Available: https://doi.org/10.1038/ncomms7465 [Cited on page 72.]

[141] B. Alonso, I. J. Sola, and H. Crespo, "Self-calibrating d-scan: measuring ultrashort laser pulses on-target using an arbitrary pulse compressor," *Scientific Reports*, vol. 8, no. 1, 2018. [Cited on page 72.]

[142] E. Escoto, D. Gerth, B. Hofmann, and G. Steinmeyer, "Strategies for the characterization of partially coherent ultrashort pulses with dispersion scan," *Journal of the Optical Society of America B*, vol. 36, no. 8, pp. 2092–2098, 2019. [Cited on page 72.]

[143] K. G. Wilcox and A. Tropper, "Comment on SESAM-free mode-locked semiconductor disk laser," *Laser Photonics Review*, vol. 7, 2013. [Cited on page 84.]

[144] U. Bandelow, M. Radziunas, A. Vladimirov, B. Hüttl, and R. Kaiser, "40 GHz mode-locked semiconductor lasers: Theory, simulations and experiment," *Optical and Quantum Electronics*, vol. 38, no. 4, pp. 495–512, 2006. [Online]. Available: https://doi.org/10.1007/s11082-006-0045-2 [Cited on pages 84 and 86.]

[145] E. J. Saarinen, A. Härkönen, R. Herda, S. Suomalainen, L. Orsila, T. Hakulinen, M. Guina, and O. G. Okhotnikov, "Harmonically mode-locked VECSELs for multi-GHz pulse train generation," *Optics Express*, vol. 15, no. 3, pp. 955–964, 2007. [Online]. Available: https://opg.optica.org/oe/abstract.cfm?URI=oe-15-3-955 [Cited on page 85.]

[146] E. J. Saarinen, J. Lyytikäinen, and O. G. Okhotnikov, "Hysteresis and multiple pulsing in a semiconductor disk laser with a saturable absorber," *Physical Review E*, vol. 78, no. 016207, 2008. [Online]. Available: https://link.aps.org/doi/10.1103/PhysRevE.78.016207 [Cited on page 85.]

[147] R. Raghunathan, J. K. Mee, M. T. Crowley, F. Grillot, V. Kovanis, and L. F. Lester, "Modeling and characterization of pulse shape and pulse train dynamics in two-section passively mode-locked quantum dot lasers," vol. 8619, Conference Proceedings, p. 86190C. [Online]. Available: https://ui.adsabs.harvard.edu/abs/2013SPIE.8619E..0CR [Cited on page 87.]

[148] J. K. Mee, R. Raghunathan, D. Murrell, A. Braga, Y. Li, and L. F. Lester, "Experimental study of the stability of harmonic mode-locking in quantum dot passively mode-locked lasers," in *CLEO: 2014*, ser. OSA Technical Digest (online). Optica Publishing Group, Conference Proceedings, p. SF2G.6. [Online]. Available: https://opg.optica.org/abstract.cfm?URI=CLEO_SI-2014-SF2G.6 [Cited on page 87.]

[149] L. Drzewietzki, S. Breuer, and W. Elsäßer, "Suppression of Q-switching instabilities of passively modelocked semiconductor lasers by a passive electrical circuit," *Electronics Letters*, vol. 47, no. 17, pp. 988–989, 2011. [Cited on pages xviii, 87, and 88.]

[150] R. Nietzkb, J. Sacher, and W. Elsasser, "Mode-locking of a semiconductor laser by self-synchronizing optoelectronic feedback of the longitudinal-mode beats," in *Conference on Lasers and Electro-Optics*, ser. OSA Technical Digest, vol. 7. Optica Publishing Group, Conference Proceedings, p. CFL2. [Online]. Available: https://opg.optica.org/abstract.cfm?URI=CLEO-1990-CFL2 [Cited on pages xviii, 87, and 88.]

[151] T. R. Schibli, U. Morgner, and F. X. Kärtner, “Control of Q-switched mode locking by active feedback,” *Optics Letters*, vol. 26, no. 3, pp. 148–150, 2001. [Online]. Available: https://opg.optica.org/ol/abstract.cfm?URI=ol-26-3-148

[152] G. J. Valentine, E. A. Bente, D. Burns, and A. I. Ferguson, “Active stabilization of quasi-CW passively modelocked Nd:based lasers using closed-loop feedback,” in *Proc. SPIE*, vol. 5137, Conference Proceedings, pp. 88–99. [Online]. Available: https://ui.adsabs.harvard.edu/abs/2003SPIE.5137...88V [Cited on page 87.]

[153] L. Goldberg and D. A. V. Kliner, “Deep-UV generation by frequency quadrupling of a high-power GaAlAs semiconductor laser,” *Optics Letters*, vol. 20, no. 10, pp. 1145–1147, 1995. [Online]. Available: https://opg.optica.org/ol/abstract.cfm?URI=ol-20-10-1145 [Cited on page 89.]

[154] H. Kano and H.-o. Hamaguchi, “In-vivo multi-nonlinear optical imaging of a living cell using a supercontinuum light source generated from a photonic crystal fiber,” *Optics Express*, vol. 14, no. 7, pp. 2798–2804, 2006. [Online]. Available: https://opg.optica.org/oe/abstract.cfm?URI=oe-14-7-2798 [Cited on page 89.]

[155] S. Tang, T. B. Krasieva, Z. Chen, G. Tempea, and B. J. Tromberg, “Effect of pulse duration on two-photon excited fluorescence and second harmonic generation in nonlinear optical microscopy,” *J Biomed Opt*, vol. 11, no. 020501, 2006. [Cited on page 89.]

[156] F. Helmchen and W. Denk, “Deep tissue two-photon microscopy,” *Nature Methods*, vol. 2, no. 12, pp. 932–940, 2005. [Online]. Available: https://doi.org/10.1038/nmeth818 [Cited on page 89.]

[157] D. Kobat, M. E. Durst, N. Nishimura, A. W. Wong, C. B. Schaffer, and C. Xu, “Deep tissue multiphoton microscopy using longer wavelength excitation,” *Optics Express*, vol. 17, no. 16, pp. 13 354–13 364, 2009. [Online]. Available: https://opg.optica.org/oe/abstract.cfm?URI=oe-17-16-13354 [Cited on page 89.]

[158] I. H. Chen, S. W. Chu, C. K. Sun, P. C. Cheng, and B. L. Lin, “Wavelength dependent damage in biological multi-photon confocal microscopy: A micro-spectroscopic comparison between femtosecond Ti:sapphire and Cr:forsterite laser sources,” *Optical and Quantum Electronics*, vol. 34, no. 12, pp. 1251–1266, 2002. [Online]. Available: https://doi.org/10.1023/A:1021303426482 [Cited on page 89.]

[159] D. Auth, S. Liu, J. Norman, J. Edward Bowers, and S. Breuer, "Passively mode-locked semiconductor quantum dot on silicon laser with 400 Hz RF line width," *Optics Express*, vol. 27, no. 19, pp. 27 256–27 266, 2019. [Online]. Available: https://opg.optica.org/oe/abstract.cfm?URI=oe-27-19-27256 [Cited on page 90.]

[160] M. Digonnet, *Rare-Earth-Doped Fiber Lasers and Amplifiers, Revised and Expanded*. Taylor Francis, 2001. [Online]. Available: https://books.google.pt/books?id=cogRJ6Lr-1gC [Cited on page 90.]

[161] D. Zimmerman and L. Spiekman, "Amplifiers for the masses: EDFA, EDWA, and SOA amplets for metro and access applications," *Lightwave Technology, Journal of*, vol. 22, pp. 63–70, 2004. [Cited on page 90.]

[162] M. J. O. Mahony, "Semiconductor laser optical amplifiers for use in future fiber systems," *Journal of Lightwave Technology*, vol. 6, no. 4, pp. 531–544, 1988. [Cited on page 90.]

[163] T. Saitoh and T. Mukai, "Recent progress in semiconductor laser amplifiers," *Journal of Lightwave Technology*, vol. 6, no. 11, pp. 1656–1664, 1988.

[164] S. Yamamoto, K. Mochizuki, H. Wakabayashi, and Y. Iwamoto, "Long-haul high-speed optical communication systems using a semiconductor laser amplifier," *Journal of Lightwave Technology*, vol. 6, no. 10, pp. 1554–1558, 1988.

[165] G. P. Agrawal and N. A. Olsson, "Self-phase modulation and spectral broadening of optical pulses in semiconductor laser amplifiers," *IEEE Journal of Quantum Electronics*, vol. 25, no. 11, pp. 2297–2306, 1989. [Cited on page 97.]

[166] G. P. Agrawal and N. Olsson, "Amplification and compression of weak picosecond optical pulses by using semiconductor-laser amplifiers," *Optics Letters*, vol. 14, no. 10, pp. 500–502, 1989. [Online]. Available: https://opg.optica.org/ol/abstract.cfm?URI=ol-14-10-500 [Cited on pages 96 and 97.]

[167] N. A. Olsson and G. P. Agrawal, "Spectral shift and distortion due to self-phase modulation of picosecond pulses in 1.5 μm optical amplifiers," *Applied Physics Letters*, vol. 55, no. 1, pp. 13–15, 1989. [Online]. Available: https://doi.org/10.1063/1.101742 [Cited on pages 96 and 98.]

[168] N. A. Olsson, "Lightwave systems with optical amplifiers," *Journal of Lightwave Technology*, vol. 7, no. 7, pp. 1071–1082, 1989. [Cited on page 90.]

[169] P. Borri, W. Langbein, J. Hvam, F. Heinrichsdorff, M. H. Mao, and D. Bimberg, "Spectral hole-burning and carrier-heating dynamics in quantum-dot amplifiers: Comparison with bulk amplifiers," *physica status solidi (b)*, vol. 224, pp. 419–423, 2001. [Cited on page 91.]

[170] J. Park, Y. D. Jang, J. S. Baek, N. J. Kim, K. J. Yee, H. Lee, D. Lee, S. H. Pyun, W. G. Jeong, and J. Kim, "Gain recovery in a quantum dot semiconductor optical amplifier and corresponding pattern effects in amplified optical signals at 1.5 μm," *Optics Express*, vol. 20, no. 6, pp. 6215–6224, 2012. [Online]. Available: https://opg.optica.org/oe/abstract.cfm?URI=oe-20-6-6215 [Cited on page 91.]

[171] S. Schneider, P. Borri, W. Langbein, U. Woggon, R. L. Sellin, D. Ouyang, and D. Bimberg, "Linewidth enhancement factor in InGaAs quantum-dot amplifiers," *IEEE Journal of Quantum Electronics*, vol. 40, no. 10, pp. 1423–1429, 2004. [Cited on page 91.]

[172] V. Cesari, P. Borri, M. Rossetti, A. Fiore, and W. Langbein, "Refractive index dynamics and linewidth enhancement factor in p-doped InAs–GaAs quantum-dot amplifiers," *IEEE Journal of Quantum Electronics*, vol. 45, no. 6, pp. 579–585, 2009. [Cited on page 91.]

[173] A. V. Uskov, J. Mørk, B. Tromborg, T. W. Berg, I. Magnusdottir, and E. P. O'Reilly, "On high-speed cross-gain modulation without pattern effects in quantum dot semiconductor optical amplifiers," *Optics Communications*, vol. 227, no. 4, pp. 363–369, 2003. [Online]. Available: https://www.sciencedirect.com/science/article/pii/S0030401803020091 [Cited on page 91.]

[174] T. Akiyama, N. Hatori, Y. Nakata, H. Ebe, and M. Sugawara, "Pattern-effect-free amplification and cross-gain modulation achieved by using ultrafast gain nonlinearity in quantum-dot semiconductor optical amplifiers," *physica status solidi (b)*, vol. 238, pp. 301–304, 2003. [Cited on page 91.]

[175] T. Akiyama, H. Kuwatsuka, N. Hatori, Y. Nakata, H. Ebe, and M. Sugawara, "Symmetric highly efficient ($\approx$ 0 dB) wavelength conversion based on four-wave mixing in quantum dot optical amplifiers," *Photonics Technology Letters, IEEE*, vol. 14, pp. 1139–1141, 2002. [Cited on page 91.]

[176] Y. Ding, R. Aviles-Espinosa, M. A. Cataluna, D. Nikitichev, M. Ruiz, M. Tran, Y. Robert, A. Kapsalis, H. Simos, C. Mesaritakis, T. Xu, P. Bardella, M. Rossetti, I. Krestnikov, D. Livshits, I. Montrosset, D. Syvridis, M. Krakowski, P. Loza-Alvarez, and E. Rafailov, "High peak-power picosecond pulse generation at 1.26 μm using a quantum-dot-based external-cavity mode-locked laser and tapered optical amplifier," *Optics Express*, vol. 20, no. 13, pp. 14 308–14 320, 2012. [Online]. Available: https://opg.optica.org/oe/abstract.cfm?URI=oe-20-13-14308 [Cited on page 91.]

[177] C. Weber, L. Drzewietzki, M. Rossetti, T. Xu, P. Bardella, H. Simos, C. Mesaritakis, M. Ruiz, I. Krestnikov, D. Livshits, M. Krakowski, D. Syvridis, I. Montrosset, E. U. Rafailov, W. Elsäßer, and S. Breuer, "Picosecond pulse amplification up to a peak power of 42 w by a quantum-dot tapered optical amplifier and a mode-locked laser emitting at 1.26 μm," *Optics Letters*, vol. 40, no. 3, pp. 395–398, 2015. [Online]. Available: https://opg.optica.org/ol/abstract.cfm?URI=ol-40-3-395 [Cited on page 91.]

[178] F. Romstad, P. Borri, W. W. Langbein, J. Mørk, and J. M. Hvam, "Measurement of pulse amplitude and phase distortion in a semiconductor optical amplifier: from pulse compression to breakup," *IEEE Photonics Technology Letters*, vol. 12, pp. 1674–1676, 2000. [Cited on page 91.]

[179] H. Schmeckebier, *Quantum-Dot-Based Semiconductor Optical Amplifiers for O-Band Optical Communication*, ser. Springer Theses. Springer, 2017. [Cited on pages 91 and 97.]

[180] D. Strickland and G. Mourou, "Compression of amplified chirped optical pulses," *Optics Communications*, vol. 55, no. 6, pp. 447–449, 1985. [Online]. Available: https://www.sciencedirect.com/science/article/pii/0030401885901518 [Cited on page 92.]

[181] P. P. Baveja, D. N. Maywar, A. M. Kaplan, and G. P. Agrawal, "Spectral broadening in ultrafast semiconductor optical amplifiers induced by gain dynamics and self-phase modulation," *Optics Letters*, vol. 35, no. 3, pp. 294–296, 2010. [Online]. Available: https://opg.optica.org/ol/abstract.cfm?URI=ol-35-3-294 [Cited on page 97.]

[182] L. M. Frantz and J. S. Nodvik, “Theory of pulse propagation in a laser amplifier,” *Journal of Applied Physics*, vol. 34, no. 8, pp. 2346–2349, 1963. [Online]. Available: https://doi.org/10.1063/1.1702744 [Cited on page 97.]

[183] E. O. Schulz-DuBois, “Pulse sharpening and gain saturation in traveling-wave masers,” *The Bell System Technical Journal*, vol. 43, no. 2, pp. 625–658, 1964.

[184] E. Fill and W. Schmid, “Amplification of short pulses in CO_2 laser amplifiers,” *Physics Letters A*, vol. 45, no. 2, pp. 145–146, 1973. [Online]. Available: https://www.sciencedirect.com/science/article/pii/0375960173904635 [Cited on page 97.]

[185] I. W. Marshall and D. M. Spirit, “Observation of large-pulse compression by a saturated traveling wave semiconductor laser amplifier,” in *Conference on Lasers and Electro-Optics*, ser. OSA Technical Digest, vol. 7. Optica Publishing Group, Conference Proceedings, p. TUM64. [Online]. Available: https://opg.optica.org/abstract.cfm?URI=CLEO-1988-TUM64 [Cited on page 97.]

[186] A. F. Forrest, M. Krakowski, P. Bardella, and M. A. Cataluna, “Double-pass amplification of picosecond pulses with a tapered semiconductor amplifier,” *Optics Express*, vol. 27, no. 21, pp. 30 752–30 762, 2019. [Online]. Available: https://opg.optica.org/oe/abstract.cfm?URI=oe-27-21-30752 [Cited on page 106.]